MAX-PLANCK-GESELLSCHAFT

Max-Planck-Institut für Metallforschung

Stuttgart, Germany

Liquid Phase Sintering of SiC Ceramics with Rare Earth Sesquioxides

Koushik Biswas

Dissertation
An der

Universität Stuttgart

Dezember 2002

Liquid Phase Sintering of SiC Ceramics with Rare Earth Sesquioxides

Dissertation

Von der Fakultät Chemie der Universität Stuttgart
zur Erlangung der Würde eines
Doktors der Naturwissenschaften (Dr. rer. nat.)
genehmigte Abhandlung

Vorgelegt von

Koushik Biswas

Aus Calcutta, Indien

Hauptberichter : Prof. Dr. rer. nat. F. Aldinger
Mitberichter : Prof. Dr. rer. nat. Dr. hc. mult. G. Petzow
Tag der mündlichen Prüfung : 16.12.2002

Institut für Nichtmetallische Anorganische Materialien der Universität Stuttgart

Max-Planck Institut für Metallforschung, Stuttgart

Pulvermetallurgisches Laboratorium

2002

Dedicated to my parents

Acknowledgements

I am taking this opportunity to thank my thesis supervisor, Prof. Fritz Aldinger, for his earnest involvement and competent guidance in every phase of this work. Without his inspirational presence, this work would not have seen the light of the day.

I would also like to convey my sincerest thanks and deepest gratitude to my group leader Dr. G. Rixecker for his day to day involvement in this work. He never failed to extend his helping hands with a smiling face for bailing me out from any kind of difficulties that I faced during the course of this work. The most important thing in any research is to find a proper direction and to move along that direction to see the fruition of one's labour. Georg's perspicacious knowledge had helped me immensely in this regard, otherwise it would not have been possible for me to see the timely completion of this endeavour.

It's my great privilege to thank Prof. G. Petzow and Prof. E. J. Mittemeijer for giving consent to examine my thesis taking time out from their extremely busy diurnal schedule.

It goes with out saying that I have actualised my dream by completing this work. So, I don't want to fritter away this chance without thanking Mr. Schweitzer, Mr. Mager, Mr. Labitzke, Mrs. Predel, Mrs. Thomas, Mr. Siegle, Dr. Zorn, Mr. Kaiser, Mr. Wörner, Mr. Kummer, Mrs. Schäfer, Mrs. Carle, Mr. Bruckner and all other technicians who had helped me with their respective capacities during various phases of this work. My sincerest thanks to all of them. I am indebted to Mrs. Rohrbach and Mrs. Paulsen for their assistance at various stages of my stay.

It would be a grave mistake from my part if I failed to acknowledge the help of my friends. I would like to thank Nick, Jayaganthan, Haihui, Rudolf, both Stefanies, Branko, Krenar, Narayanan, Subasri, Pradyot, Ravi, Kartik and many other friends who not only helped me from being engulfed by frustration at times but also made my days at PML memorable. I will fondly remember their consort long after I leave PML. Their memories will remain as a string of pearl in the inner sanctum of my heart.

Last but not the least, I would like to remember the affection of my parents and the love of my brother who always helped me remaining behind the curtain. Without their encouragement, I would not have become what I am today.

Contents

List of figures

List of tables

Nomenclature

a	....	Half the diagonal of the Vickers indentation/distance between the center of two ions
A	....	Pre-exponential constant
AES	....	Auger electron spectroscopy
AN	....	Annealed
AS	....	As-sintered
b	....	Breadth of the specimen/Burgers vector
c	....	Crack length
CN	....	Coordination number
d_H	....	Diagonal of Vickers indentation
D	....	Diffusivity
δ_{gb}	....	Grain boundary width
e	....	Elementary electric charge
E	....	Young's modulus
EDS	....	Energy dispersive spectroscopy
ε	....	Strain
$\dot{\varepsilon}$	....	Strain rate
F	....	Force/intensity
F_c	....	Field strength
Δf	....	Specimen displacement
ϕ	....	Diameter
Φ	....	Geometric constant
G	....	Grain size
$\overline{G}$	....	Average grain size
h	....	Height of the specimen
H	....	Vickers hardness
k	....	Boltzmann's constant
K_{Ic}	....	Fracture toughness
k_p	....	Parabolic oxidation rate constant

l_o	....	Length between the two outer supports of 4-point bending fixture
l_i	....	Length between the two inner supports of 4-point bending fixture
L	....	Vickers indentation crack length
LPS	....	Liquid phase sintering
m	....	Mass of the body
Δm	....	Mass loss
MOR	....	Modulus of rupture
n	....	Stress exponent
N	....	Fatigue cycle, atomic nitrogen
Ω_i	....	Atomic volume
P	....	Volume fraction of the pore/power law exponent
Q	....	Activation energy
R	....	Radius of the ion/gas constant
ρ	....	Density
SEM	....	Scanning electron microscopy
σ	....	Strength
t	....	Tolerance factor/time
T	....	Temperature in K
TEM	....	Transmission electron microscopy
ΔW	....	Specific weight gain
XRD	....	X-ray diffraction
Z	....	Charge of the ion

Abstract

In order to improve the high temperature performance of the intergranular phase of liquid phase sintered SiC, additive systems containing different rare earth sesquioxides were used as sintering aids. This new approach came because of the relatively poor refractoriness of the secondary phases that are formed with the "conventional" Y_2O_3-AlN sintering additives. Refractory rare-earth disilicates, $RE_2Si_2O_7$, can be crystallised at grain boundaries, thereby resulting in good high temperature properties.

In the present investigation, the effects of different pairs of rare earth sesquioxides and AlN-rare earth oxide combinations on the sinterability of SiC were observed with the help of dilatometric studies. Sintering experiments under varying conditions were performed in order to test the effectiveness of these additives for complete densification of SiC. Gd_2O_3-Ho_2O_3 and Dy_2O_3-Ho_2O_3 in equimolar ratio were found to be promising candidates as sintering additives at 10 vol% total additive content. N_2 as sintering atmosphere proved to be better than Ar in terms of densification behaviour. Liquid phase sintering of SiC with these additive systems occurred through a solution-reprecipitation mechanism. This fact was established with the help of SEM, TEM, EDS and AES analysis on the grains and grain boundary/intergranular phases. Sintering kinetics depend not only on the cationic radius of the rare earth, but also on the thermodynamics of the system. Post sintering heat treatments were performed in N_2 at 1950°C for several hours in order to crystallise the secondary amorphous phases, to develop a suitable microstucture for better fracture mechanical properties and to obtain full $\beta \rightarrow \alpha$-SiC phase transformation. Phase evolution, extent of crystallisation, phase transformation and mechanical properties were correlated with SEM and XRD studies.

In a different study, Lu_2O_3 substitution for Y_2O_3 in the "conventional" Y_2O_3-AlN additive system was done by varying the molar ratio of Lu_2O_3 to AlN. Densification to more than 99% was achieved in all the compositional range. Increase of the Lu_2O_3 content in the additive system deteriorates the wetting behaviour and limits the extent of devitrification as well as $\beta \rightarrow \alpha$-SiC transformation. The influence of these parameters on the fracture mechanical properties as well as the microstructural development after sintering and annealing are elaborately discussed. 4-point bending

strength was measured between room temperature and 1500°C. Room temperature bending strength of ~ 600 MPa was obtained due to formation of a bimodal microstructure. High temperature flexural strengths at 1500°C were found to be ~ 500-550 MPa with a strength retention up to 93% of the room temperature value. Creep and compliance tests were performed at various temperatures. High temperature mechanical properties were mainly influenced by the visco-elastic properties and degree of crystallisation of the secondary phase. Creep in these materials was primarily influenced by grain boundary diffusion in the low temperature region (at 1200°C). However, at higher temperature, the main operative mechanisms were found to be grain boundary sliding accomodated by diffusion and cavity formation in the near surface region. Material with high Lu_2O_3 content showed a 10% drop of stiffness at 1450°C during compliance tests which signifies an extraordinarily high retention of the mechanical properties at high temperature. The thermomechanical behaviour was found to be even better in case of the material with an equimolar ratio of $1Lu_2O_3$:$1AlN$ due to an optimum trade-off between viscosity and crystallisation. Oxidation resistance tests were performed in air at various temperatures from 1200°C to 1500°C. The oxidation kinetics were found to be based on a complex mechanism. They are not only influenced by diffuion of oxygen through SiO_2 layer, but also depend on the interfacial reaction between the growing SiO_2 layer and the secondary phases.

1 Introduction

1.1 Foreword

The need for advanced materials has been there since the early days of civilisation and the demand for these materials has currently increased due to the rapid advancement in technology. The main reasons for the attention focused on ceramics as possible structural materials are their heat resistance and wear resistance. As a matter of fact, however, few ceramics are capable of maintaining their strength at temperatures which prohibit the use of metals, the exceptions being covalent materials like Si_3N_4 and SiC, etc. The development of silicon carbide ceramics during the last two decades is one example for the progress that has been made. Application of SiC compacts as structural materials can be broadly divided into two categories: (i) abrasion and corrosion resistant components and (ii) heat resistant components. It was found that SiC sintered bodies possess superior strength at high temperatures, and they were seen as a promising heat-resistant structural material. Their characteristics include high temperature properties like creep resistance, bending strength, high hardness, heat resistance and corrosion resistance. These properties enable SiC to be the prime material for structural components such as high temperature furnace components (heating elements, core tubes, refractory bricks, etc.) [1]. These applications, however, do not require high density sintered bodies. The developments of SiC compacts as structural components with high density were initially begun with the objective of application to gas turbine engines.

Si–C bonds have a high degree of covalency (87 %) [2], and this is the source of the intrinsically high strength of SiC sintered bodies. SiC is fundamentally a brittle material. Its low fracture toughness presents difficulties in application as a structural material. But SiC sintered bodies belong to the few materials, which can be used at extremely high temperatures (e.g. 1300°C and above). However, due to the highly covalent bond characteristics, it is difficult to sinter these materials to full density. The poor sinterability necessitates addition of a sintering aid for densification [1]. Addition of suitable sintering additives leads to dense, fine-grained microstructures and, hence, high strength of the sintered body, but generally it may also result in the formation of secondary phases at the grain boundaries that frequently cause loss of high temperature

strength due to softening of these phases. Three representative technologies have been developed for sintering of SiC namely, hot pressing with a sintering aid, pressureless or gas pressure sintering with a sintering aid, and reaction sintering. Among these techniques, pressureless sintering is considered to be the most important from an industrial standpoint because it allows the manufacture of large or complex-shaped pieces, offers good mass productivity and low cost, and can produce products with superior performance. Besides conventional solid state sintering, one of the pressureless sintering methods is liquid phase sintering (LPS) which has been applied extensively to obtain highly dense (>95 % theoretical density) SiC ceramics [1]. Several additives or combinations of them, such as Al_4C_3, Al_2O_3-Y_2O_3, Al_2O_3-Y_2O_3-CaO and AlN-Y_2O_3 have been investigated for SiC in order to improve the thermomechanical behaviour.

Typically LPS-SiC ceramics consist of highly refractory SiC grains bonded by a less refractory vitreous phase. Therefore the high temperature behaviour depends primarily on the composition, distribution, and crystallinity of the intergranular phase. In order to improve the high temperature performance of the intergranular phase, additive systems containing different rare-earth sesquioxides have been used in the case of Si_3N_4 and SiAlON materials [3-8]. This new approach was motivated by the relatively poor refractoriness of the glass phases formed with conventional sintering additives, particularly the aluminium containing ones. Refractory rare-earth disilicates, $RE_2Si_2O_7$, can be crystallised in the case of the RE_2O_3-based additives, resulting in good high temperature properties.

It has been the intention of the present investigation, to study the effects of different pairs of rare-earth sesquioxides and AlN-rare-earth oxide mixtures on the sinterability of SiC with the help of dilatometric studies. Sintering experiments under varying conditions were performed in order to test the effectiveness of these additives for the complete densification of SiC. Post sintering heat treatments help to obtain an interlocking structure of high-aspect ratio plate-like grains. Creep resistance, room and high temperature flexural strength, and other fracture mechanical properties were investigated on the optimised systems. The evolution of different phases during sintering and annealing, and influences of the phase composition on the materials' properties, particularly the fracture mechanical properties, have been correlated with the help of TEM, SEM, XRD, AES and EDS. Oxidation resistance and high temperature

compliance tests were performed in order to establish the superior thermomechanical properties of some of these new systems over existing additive systems.

1.2 Literature review

1.2.1 Crystal Structure

Silicon carbide occurs with many different crystal structures [l,2]. All of them are characterised by the fact that any given atom is always tetrahedrally bonded with four heteroatoms. The nearest-neighbour bonding distance is approximately 1.89 Å. All structures can be considered as polytypes consisting of differently packed layers of atoms. According to Ramsdell [9], the notation of these polytype consists of one number describing the number of layers (A, B or C-layer) associated with the unit cell, and a letter indicating the crystal system (cubic (C), hexagonal (H) or rhombohedral (R)). The cubic 3C polytype is designated as β-SiC and all other polytypes are referred to as α-SiC. The stacking order of the closely-packed plane (the (111) plane in cubic crystals and the (0001) plane in hexagonal crystals) is shown (*Figure 1.1*) by the stacking sequence (ABC). The stacking of β-SiC in the (111) direction is ...ABCABC..., while that of the hexagonal (2H) variety in the direction of the c-axis is ...ABAB... . The 2H polytype is not stable above 1400°C and transforms to different polytypes depending on the temperature [10]. At 1600°C or above, the stacking sequence changes to ...ABCACB... or ...ABCB... mainly due to stacking transformation, leading to α-SiC polytypes denoted as 6H and 4H respectively [10].
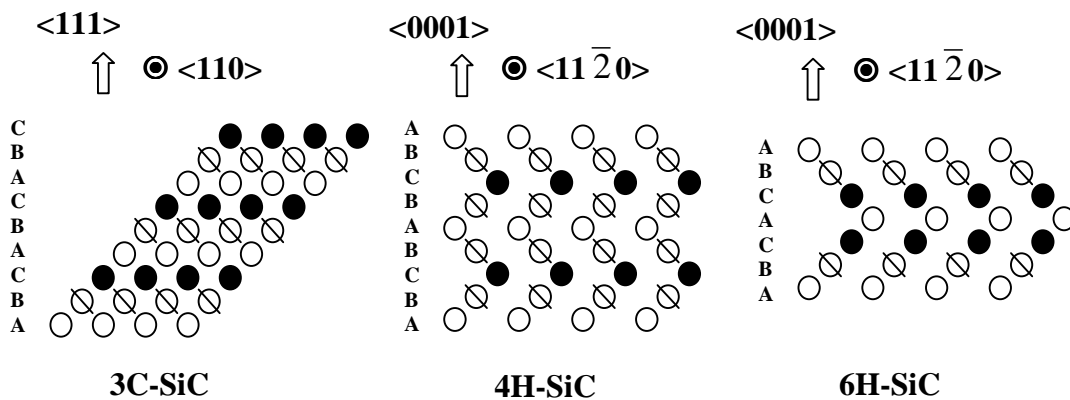
Figure 1.1: Structure of cubic and hexagonal SiC that crystallises in the zinc blende structure and faulted wurtzite structures, respectively.

1.2.2 SiC powder production

Silicon carbide is manufactured most frequently on an industrial scale using the **Acheson method** [11]. In this technique, two solid electrodes are connected with graphite powder, a mixture of silica and coke is packed in the surrounding area, and the whole assembly is electrically heated at 2700°C for producing SiC mainly by the reaction:

$$SiO_2 + 3C \rightarrow SiC + 2CO \qquad (1.1)$$

SiC crystal blocks from the reaction are then ground, refined and classified to produce SiC powders. The SiC grades thus prepared are characterised as α-SiC having a relatively coarse grained structure with a mean particle size of 5 µm. This requires a further refining process to produce submicron grain powders suitable for sintering [12].

β-SiC is also produced by the Acheson method at low temperature (1500-1800°C) [6]. Hence, like α-SiC, it is also possible to manufacture fine grained β-SiC powders through the Acheson process followed by refining treatment.

Beside that, β-SiC powders are produced using vapour-phase reactions [13-15]. **Vapour-phase methods** utilise the reaction of SiH_4 [13] or $SiCl_4$ with hydrocarbons such as CH_4 and C_3H_8 [13] or the thermal decomposition of CH_3SiCl_3, $(CH_3)_4Si$ [14], or polycarbosilane [15] to produce β-SiC. The steps leading to the production of SiC by vapour-phase methods can be summarised as follows:

$$SiH_4 + CH_4 \xrightarrow{\ 1400°C\ } SiC + 4H_2 \qquad (1.2)$$

$$CH_3\,SiCl_3 \xrightarrow{\ Plasma\ } SiC + 3HCl \qquad (1.3)$$

$$Si(CH_3)_4 \xrightarrow{\ 950-1400°C\ } SiC + 3CH_4 \qquad (1.4)$$

$$(CH_3)_2SiCl_2 \xrightarrow{\ 1200°C\ } SiC + CH_4 + 2HCl \qquad (1.5)$$
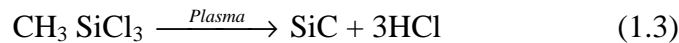
Particle size and stoichiometry are controlled by varying reaction temperature, gas concentration and gas flow rate.

Other methods include the direct reaction of silicon and carbon [16] and the gas evaporation method [17], in which the raw material surface is heated and melted using

an arc discharge in a mixed gas (consisting of an inert gas and H_2 or N_2) to form ultrafine SiC particles.

A new synthesis process was recently developed [18,19] to produce small, high purity, non-agglomerated powders of SiC. In this process, the ceramic powder is synthesised by rapidly heating (plasma heating) a reactant gas (silane (SiH_4) mixed with methane (CH_4) or ethylene (C_2H_4)). The characteristics of the powders are controlled by cell pressure, the reactants, their flow rates and flow ratios and temperature distribution within the reaction zone. Luce *et al.* [20] further studied the same process by using laser heating and by varying the reaction conditions (laser power, flow rates and ratio of reacting gases). The powder characteristics of the SiC synthesised in this way ranges from amorphous to crystalline (powder mixture).

1.2.3 Solid state sintering of silicon carbide

The high degree of covalency makes it difficult to sinter SiC by simple heating of powder compacts. As a result, many different sintering techniques have been developed. Among those techniques, hot-pressing with a sintering aid, pressureless sintering with a sintering aid and reaction sintering are important ones.

1.2.3.1 Pressureless sintering

From the industrial point of view, pressureless sintering with additives is considered to be the most important method as it offers high mass productivity at a low production cost with the flexibility to produce large complex bodies of superior performance. This technique was also applied to the sintering of SiC in order to achieve dense bodies. The absence of densification during sintering of pure silicon carbide is the result of the high amount of energy required for the formation and migration of defects in its structure, which leads to a low self diffusion coefficient and hence sintering by volume and grain boundary diffusion does not occur [21]. However, to obtain a high density of the sintered products, these mechanisms are necessary as surface diffusion does not normally lead to the elimination of pores. Prochazka [22] developed a method leading to good sinterability of silicon carbide powder. He opined that very fine particle size along with B and C additives would promote the sinterability by enhancing volume diffusion and retarding surface diffusion. A similar behaviour was also observed by Hausner [23]. He observed the effect of boron and carbon addition on the sintering of β-SiC and

pointed out that high grain boundary to surface energy ratio (γ_{GB}/γ_{SV}) hinders the densification process. He found out that the addition of boron decreases the grain boundary energy (γ_{GB}) and carbon increases the effective surface energy (γ_{SV}). The proposed combination of mechanisms was removal of the surface oxide layer of silicon carbide by carbon and reduction of the grain boundary energy by segregation of boron [22]. Suzuki and Hase [24] studied the kinetics of densification in the initial stage of sintering of SiC with addition of boron and carbon. They proposed that material transport along grain boundaries was the rate controlling factor. Murata and Smoak [25] observed that solid solution between SiC and boron compounds (BN, BP and B_4C) occurred during densification and the maximum density was obtained at the concentration corresponding to the maximum solubility of the additives in SiC (*Figure 1.2*). Additions of boron and carbon play an important role not only in densification but also in the inhibition of the grain growth of SiC crystals (*Figure 1.3*).
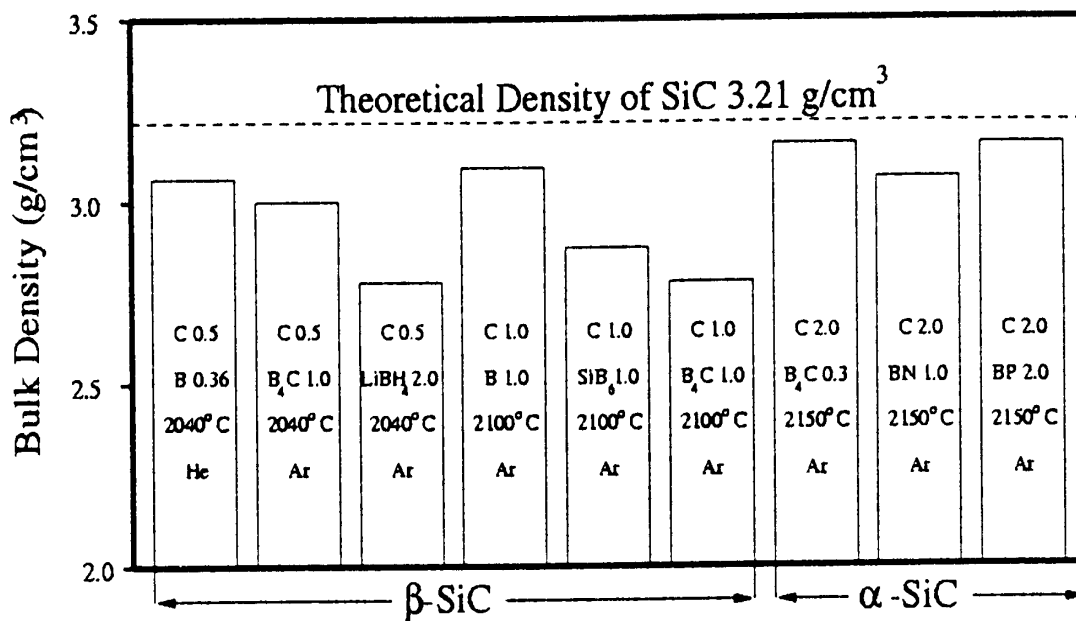
Figure 1.2: The Influence of boron compounds on the sintered density of silicon carbide (additives in wt %) [23].

Another proposed mechanism for the enhanced sintering effect of carbon and boron was that of grain growth inhibition [21]. Carbon and boron inhibit silicon carbide grain growth caused by surface diffusion during heating up to the sintering temperature, thereby maintaining the driving force for sintering up to higher temperatures where

volume diffusion-induced densification becomes active. Addition of carbon or boron alone is not effective for such an activated sintering mechanism. Stutz *et al*. [26] studied the effect of boron with carbon and aluminium with carbon in the sintering of β-SiC and found that a minimum B concentration of 0.3 wt % was required to promote densification. Carbon must be present to the tune of 2 wt %. The effectiveness of aluminium as a SiC sintering additive was discovered by Alliegro *et al.* [27] who observed that aluminium was the most effective additive after boron. But addition of only 1 % Al with 1.5 % C could not densify the cubic SiC powders to high density [26]. Bröcker *et al.* [28] first reported pressureless sintering with addition of aluminium-carbon additives. The mechanism of densification was the same as with the B-C additive system. Al-C sintering additives were proposed to act at the grain boundaries but the quantity of aluminium required was somewhat greater than that of B-C additive because firstly, the solubility limit of aluminium in silicon carbide is larger as compared to boron and secondly, the Al_4SiC_4 and Al_4C_3 produced during sintering are easily volatilised. It was also found that at a particular temperature, more densification occurred with additives from the aluminium-boron system than with pure B additives (*Figure 1.4*). A similar investigation was carried out by Shinozaki *et al.* [29], and they found that addition of Al, B and C to fine grained β-SiC enhanced the β to α transformation and subsequent growth of α-SiC platelets. The excess free carbon present was reduced by reaction with Al, and Al_4C_3, which was formed in the C-rich regions, helped to reduce the formation of large graphite particles.

Apart from the additives, the oxygen content of sinterable silicon carbide powders also affects their densification behaviour [30]. Lower oxygen content improves the densification behaviour of SiC. It was observed that 9 % difference in sintered density existed between a standard powder and a heat treated powder with 0.64 wt % O_2. The morphology of the oxygen containing phases had an influence on the densification. Hausner [23] discussed how the surface area of the powder also had a significant influence on the sintering behaviour. Powders having higher specific surface area had a higher densification rate. Silicon carbide sintered bodies with a relative density of 95 % or more were produced by pressureless sintering at 2050°C if an ultrafine raw powder with particle size of less than 0.05 μm was used [31] .
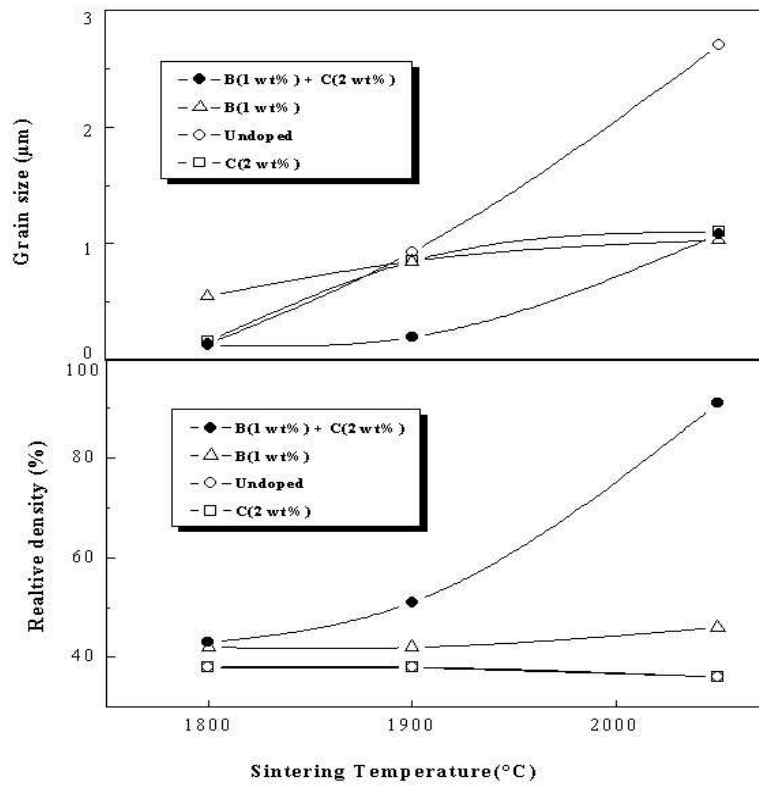
Figure 1.3: Effect of additives on grain growth and densification in sintering of SiC. (heating rate ~20 K/min; duration 1 min at 1800°C and 1900°C, 30 min at 2050°C) [22].
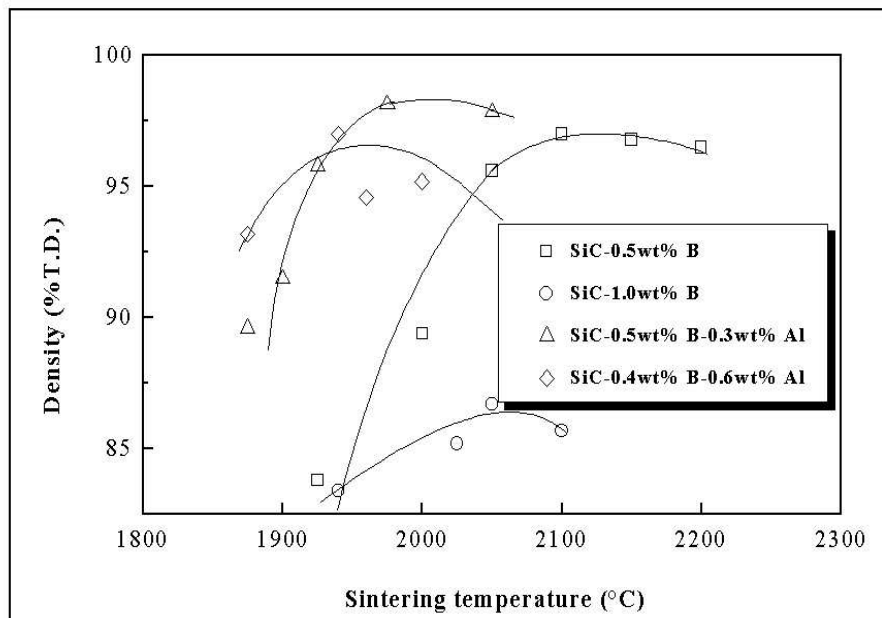
Figure 1.4: Effect of temperature on sintered density for B- and B+Al-doped silicon carbide [26].

Control of sintering atmosphere [23,32,33] and heating rate [32] were also important for the sintering of silicon carbide powders. Noble gas atmosphere gave optimum results with B-doped powders. Higher pressure of the noble gas atmosphere reduced the sintered density. N_2 had a retarding effect on the sintering of boron doped β-SiC [34]. Silicon vapour, oxygen and CO_2 gas in the system were deleterious to sintering as they resulted in a loss of boron and consequently in the inhibition of densification. Sintering was strongly inhibited by silicon vapour as a result of coarsening of the compacts. In terms of heating rate, it was observed [32] that a rapid heating rate was not favourable and in the presence of some of the additives, selection of a slower heating rate was the most effective way to increase the sintered density of silicon carbide.

1.2.3.2 Hot pressing

Hot pressing of silicon carbide ceramics was studied because of its ability to produce dense sintered bodies. By this technique, some success in densifying SiC without any additive was achieved [27]. However, pure silicon carbide powders can be hot pressed, by conventional methods, to only ~84 % of the theoretical density, but the addition of certain impurities can improve the sintered density up to 98% of the theoretical value. Another possible way of densification is hot pressing under very high pressure (~5 GPa). Nadeau [35] investigated ultra-high-pressure hot pressing and reported that high densification (approximately 98 % of the theoretical density) is possible for both α-SiC and β-SiC under a pressure of 3 GPa at 1500°C. He concluded that the mass transport phenomena that might play a role in the hot pressing of silicon carbide powders were crushing and sliding of particles, plastic deformation, evaporation and condensation and bulk or surface (including grain boundary) diffusion. The final stage of densification occurs due to diffusion controlled processes like the ones mentioned above. Kalish and Clougherty [36] reported that high pressure sintering was useful to prepare pure, fine grained and fully dense microstructures of SiC. Takatori *et al.* [37] also studied the high pressure sintering of β-SiC with no sintering additives. It was concluded that densification of SiC under high pressures depends strongly on sintering temperature, grain morphology and magnitude of the self diffusion constants. Prochazka [22] discovered that boron was an effective sintering aid. He was able to obtain a SiC compact of 99 % theoretical density when he added only 1 % boron to a submicron silicon carbide powder and sintered at 1950°C under 70 MPa pressure. It was concluded

that solid phase diffusion was the main mechanism for effective densification. Sakai and Aikawa [38] studied the phase transformation and thermal conductivity of hot-pressed β-SiC with Al_2O_3 and carbon additives. Up to 2 % Al_2O_3 the simultaneous addition of carbon was required, but specimens containing 3 wt % Al_2O_3 were densified to near the theoretical value regardless of the carbon content (*Figure 1.5*). In another investigation, Sakai and Hirosaki [39] pointed out that addition of BaO-C to SiC powders allows the compact to be densified by hot pressing. Hot pressing of SiC powders was also accomplished by addition of AlN, although the sintering mechanism was not well understood by the authors [40].
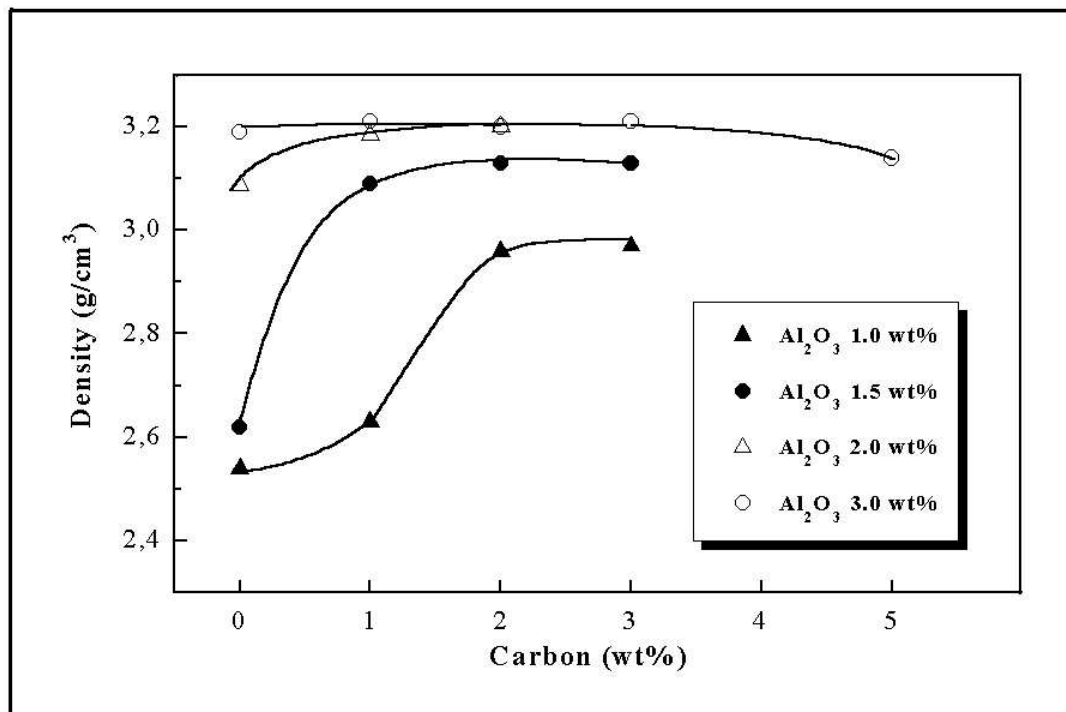
Figure 1.5: Effect of Al_2O_3 and carbon on the sintered density of SiC (all specimens hot pressed at 2050° C for 30 min) [38].

Schoennahl *et al.* [41] in their extensive study observed that hot pressing of selected compositions in the systems Si-Al-C and Si-Ti-C produced dense SiC ceramic materials. They also observed that elemental Si, C or Al addition led to a considerable diminution of the hardness of the sintered samples. Addition of complex carbides like Al_4SiC_4 or Ti_3SiC_2 to SiC aided in densification.

1.2.4 Liquid phase sintering

Liquid phase sintering has been extensively applied in order to obtain dense SiC ceramics. This innovative approach to the sintering of SiC was initiated in early 1980s [42]. The major inspiration for this densification strategy came from the sintering procedures of Si_3N_4 with Al_2O_3-Y_2O_3 additives [43-45]. By adopting them, superior self-reinforced SiC was fabricated successfully [46,47]. Various sintering parameters and types of additives were utilised for the optimisation of properties. The advantage of using a liquid phase was that SiC could be sintered to high densities (>95 % Th. D.) at temperatures well below 2000°C [48]. Another advantage of using liquid phase sintering was that SiC powder with a higher oxygen content could be densified. The use of low sintering temperature and short sintering time also allowed to obtain fine grained materials with improved mechanical properties [48].

1.2.4.1 Effect of oxide additives

In the pioneering work [42], sintering experiments were carried out at 2100°C with oxide additives that were produced by the reaction of $Al(OH)_3$ with HCl and of $Y(OH)_3$ with HCOOH. It was found that addition of Y_2O_3 did not promote densification, whereas Al_2O_3 additions enhanced the same, though equimolar additions of both the additives also gave rise to a denser material. Further, it was concluded that 3:5 was the optimum Al_2O_3 :Y_2O_3 ratio for sintering the β-SiC powder [49]. It was suggested that the densification of SiC occurred by a liquid phase containing Al and Si that was produced by the decomposition of $Al_2Y_4O_9$ above 2000°C and subsequent reaction with SiC. From Misra's [50] thermochemical analysis, it was concluded that a liquid phase was formed in the SiC-Al_2O_3 system in the temperature range of 1950-2150°C (*Figure 1.6*). With free carbon, a eutectic melt would be likely to form even at a lower temperature. These liquids helped to densify the SiC. Thus addition of alumina along with some carbon as sintering aid would be beneficial.

Pressureless sintering of submicron SiC powder with the addition of aluminium oxide was also investigated by Suzuki [51]. He achieved a sintered body with high density exceeding 97 % of the theoretical value by the addition of at least 2 wt % Al_2O_3. The densification proceeded via a liquid-phase sintering mechanism accompanied by a β → α-SiC phase transformation and a reduction in the amount of liquid phase. SiC with higher alumina content (15 %) did not densify even after a holding time of 10 h. Lower

alumina content (2 %) caused a less pronounced time dependence of the relative density. *Figure 1.7* shows the effects of alumina content and time on the densification of silicon carbide. Sigl and Kleebe [52] investigated the densification mechanism of silicon carbide using yttrium-aluminium garnet powder ($3Y_2O_3 \cdot 5Al_2O_3$). The core and rim structure in this system suggested that Ostwald ripening by solution and reprecipitation controls the sintering process. Grande *et al.* [53] also investigated the Y_2O_3-Al_2O_3 additive system. They found that SiC containing 7.5 wt % Y_2O_3-Al_2O_3 formed a eutectic and densification occurred by liquid phase sintering. It was reported that apart from alumina-yttria, relatively high density was achieved by using several other rare-earth metal oxides, usually in combination with Al_2O_3 or boron compounds. Much lower sintering temperatures (1700-1800°C) for SiC were observed by Mulla and Kristic [48], if a small amount of SiO_2 (only a few percent) was present with the Y_2O_3-Al_2O_3 system. The densification behaviour was presented as a function of the Y_2O_3-content at different temperatures (*Figure 1.8*). Thus a fraction of percent of oxygen was sufficient to reduce the temperature of liquid-phase formation.
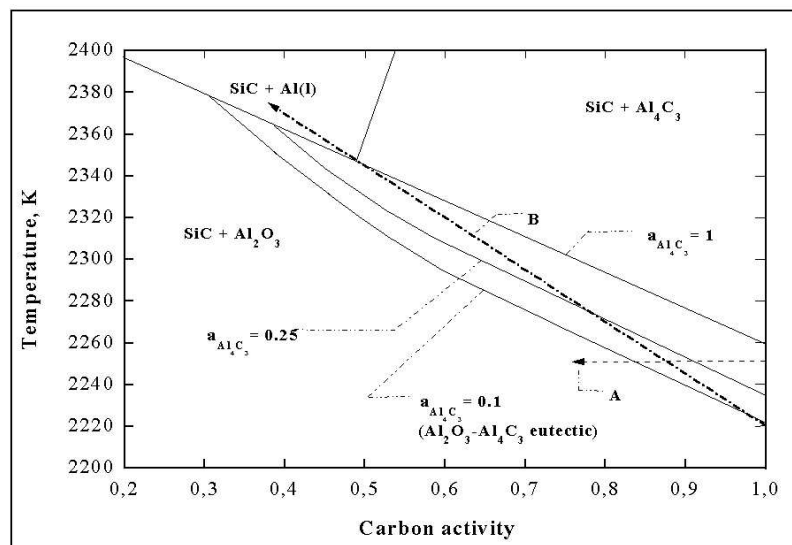
Figure 1.6: SiC-Al₂O₃ stability diagram for an ambient total pressure of 0.1 MPa showing the stability regions for the Al₂O₃ + Al₄C₃ melt and the effect of the high vapour pressure of gaseous species on the stability of the melt: (A) Change in the melt composition due to the loss of the carbon from Al₄C₃ at a constant sintering temperature of 2250 K; (B) Change in the melt composition as all of the carbon from Al₄C₃ is lost during the heating-up period for sintering at 2350 K [50].

Lange [54] in his study observed that a liquid phase was responsible for the densification of SiC powder when Al_2O_3 was used as hot-pressing aid. However, the composition of the liquid phase during densification was uncertain. The presence of SiO_2 and other impurities suggested the presence of an alumino-impurity-silicate phase. The author supported this fact by reporting that completely dense bodies were obtained at a temperature of 1800°C which is less than the melting point of pure alumina. The mechanism was a rapid rearrangement during the initial period of pressure application and densification by a solution-reprecipitation process. Kim *et al.* [47] found that addition of Y_2O_3-Al_2O_3-CaO to β-SiC densified the compact to full density by hot pressing at 1750°C.
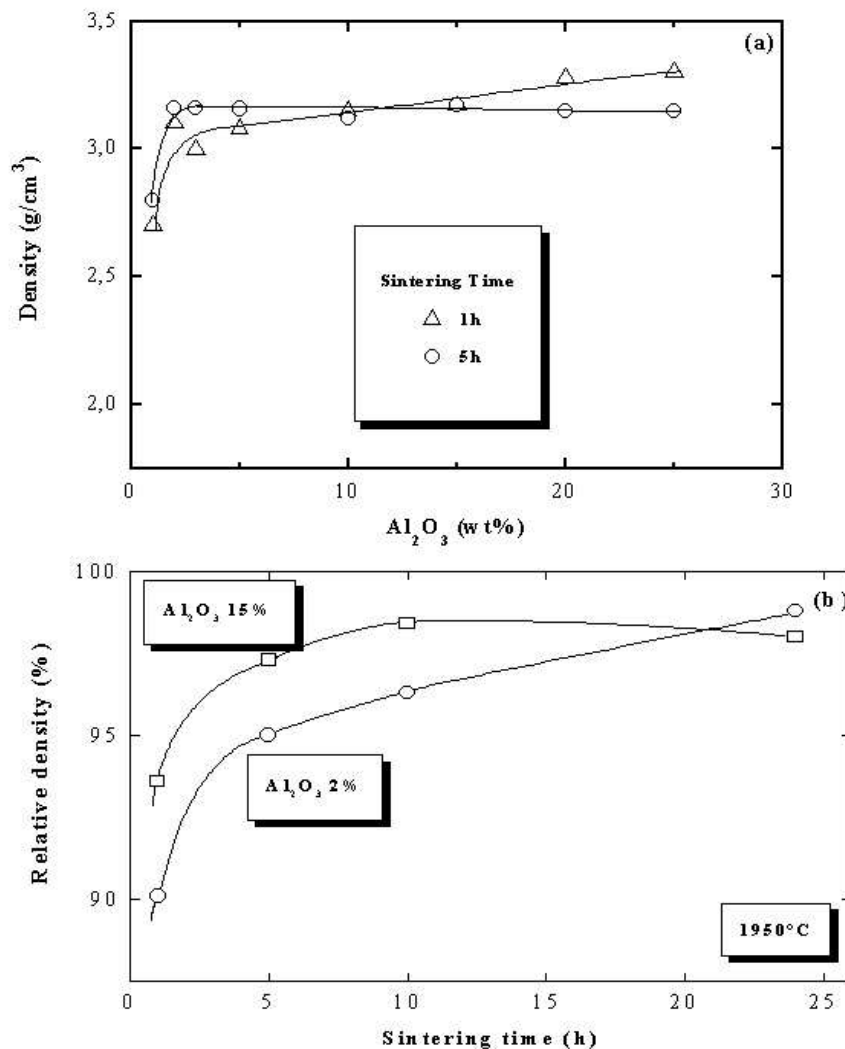
Figure 1.7: (a) Sintered density variation of SiC sintered at 2000°C for 1 and 5 h as a function of the amount of Al_2O_3 added and (b) sintered density variation of SiC (sintered at 1950°C with 2 % and 15 % Al_2O_3 addition) as a function of sintering time [45].
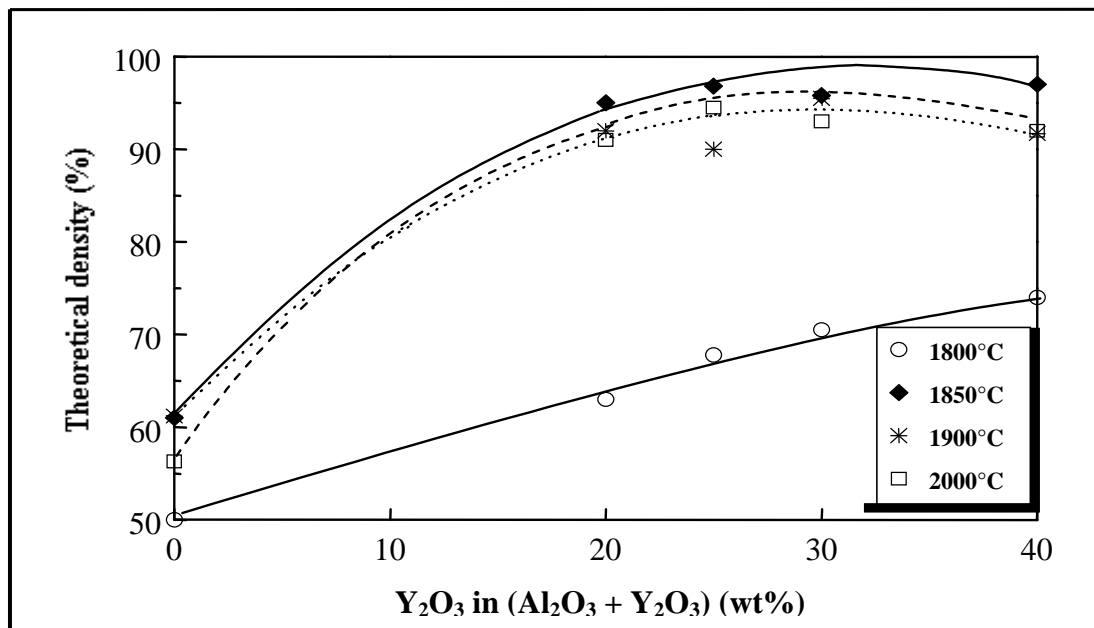
Figure 1.8: Change of sintered density of SiC with Y$_2$O$_3$ content for samples containing 10 vol % (Al$_2$O$_3$ + Y$_2$O$_3$) [48].

Nader [55] also studied oxide additives (SiO$_2$, Al$_2$O$_3$ and Y$_2$O$_3$) and found that the reaction of SiC with SiO$_2$ reduces densification. Al$_2$O$_3$ has somewhat an similar effect, whereas Y$_2$O$_3$ did not cause any effect.

1.2.4.2 Effect of nitrides and other additives

The densification of SiC using AlN-Y$_2$O$_3$ was first attempted by Chia *et al.* [56]. Nader [55], in his doctoral thesis, studied extensively the sintering behaviour of SiC with addition of AlN-Y$_2$O$_3$ and also found the beneficial effect of N$_2$ atmospheres on sintering. In another work on the same additive system, Jun *et al.* [57] reported that the amount of nitride or a N$_2$ atmosphere had a strong influence in terms of densification and grain growth behaviour of the SiC sintered bodies. *Figure 1.9* shows the effects of atmosphere and amount of sintering aids on the densification of β-SiC. Apart from improved densification behaviour, addition of AlN to LPS-SiC even could improve the beneficial effects of yttria and/or alumina dopants. An optimised composition of 10 vol % of additive with 60 mol % AlN and 40 mol % Y$_2$O$_3$ was found by Nader [55] based on the AlN-Y$_2$O$_3$ phase diagram investigated by Jeutter [58] which shows an eutectic composition at about 40 mol % AlN (*Figure 1.10*). Recently, the AlN-Y$_2$O$_3$ phase diagram was reinvestigated by Huang *et al.* [59] showing the eutectic point at 20 mol% AlN.
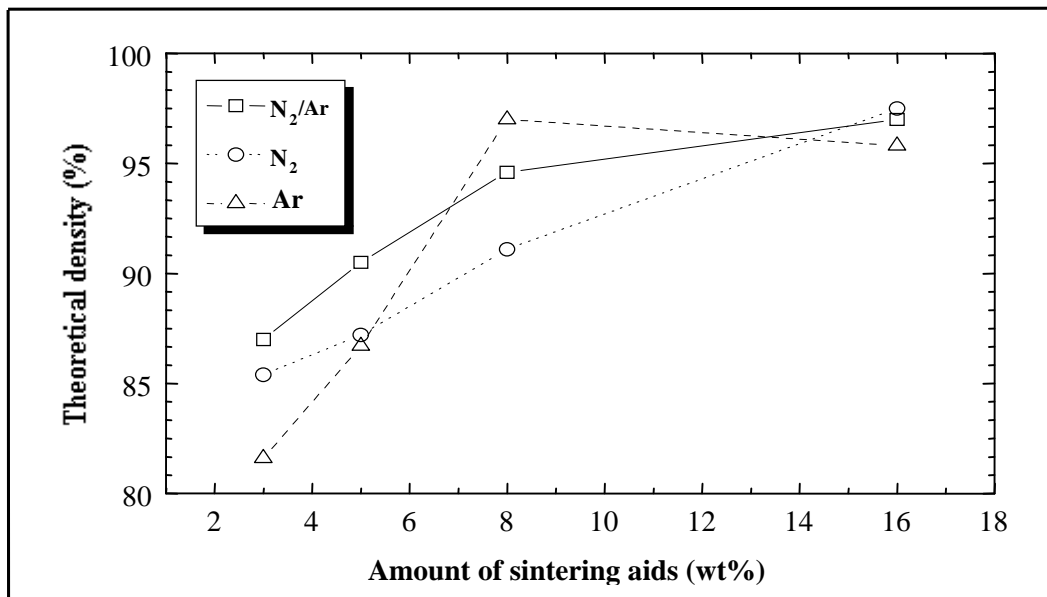
Figure 1.9: Plot of density versus amount of sintering aids (AlN-Y₂O₃) for 95% SiC / 5% AlN sintered at 2050°C for 1 h in N₂, Ar and N₂/ Ar [57].
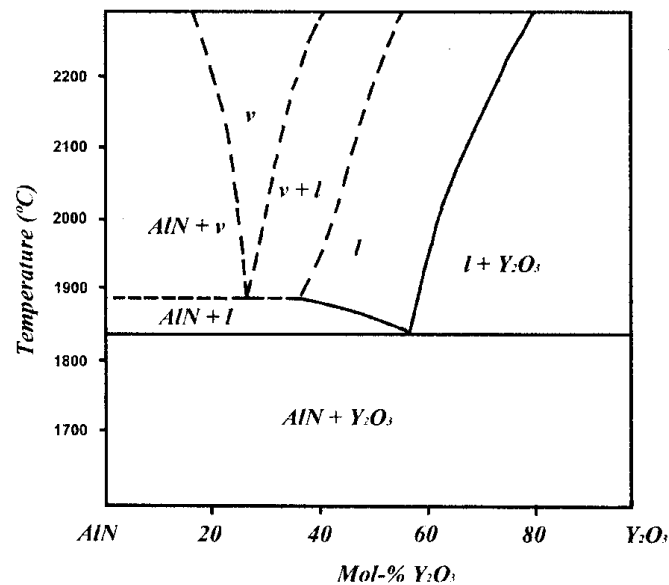
Figure 1.10: Quasibinary phase diagram of AlN-Y₂O₃ [58].

Other than nitride additives, B_4C, Al_4C_3, etc., are also reported as sintering aids for SiC. Lin *et al.* [60] studied the sintering behaviour of β-SiC powders with additions of Al, B and C and observed that a secondary phase ($Al_8B_4C_7$) was formed during hot pressing within the range of 1600°C to 1800°C with an applied pressure of 20 to 60 MPa. It was suggested that a liquid phase, which coexisted with this compound, enhanced densification. Suzuki [61] also reported on the densification of SiC by liquid phase

sintering using aluminium and carbon. Stutz *et al.* [26] studied SiC sintering in the presence of Al and B and reported that liquid formation that occurring the system SiC-Al$_4$C$_3$- B$_4$C at 1780 or 1860°C enhanced densification.

1.2.5 Microstructural aspects

1.2.5.1 Effect of B, Al and C

Pioneering work of Prochazka [22] revealed that during sintering and hot pressing with boron addition, β-SiC frequently transformed into α-SiC polytypes, mainly the 6H form. Grain growth occurred at a rate several orders of magnitude higher than the rate of grain growth of β-SiC. This phenomenon was unwanted as fine-grained microstructures were the desirable product. Hamminger *et al.* [62] investigated the microstructures of (B,C)- and (Al,C)-doped pressureless sintered SiC by wavelength dispersive X-ray analysis, Auger electron spectroscopy and Micro-radiography. Clean grain boundaries were detected in (B,C)-doped materials, while in (Al,C)-doped materials, the existence of thin Al-containing grain boundary films was revealed. In a similar type of study, Shinozaki *et al.* [63] and Greil and Stutz [64] found that addition of Al enhanced the β to α-phase transformation and subsequent basal plane growth of α-SiC which prevented exaggerated grain growth. Homogeneous distribution of the Al additive lead to homogeneously distributed fine α-SiC platelets. Without Al additions, β-phase sheaths were observed inside SiC grains that were very difficult to remove by heat treatment at higher temperature. Greil and Stutz [64] improved the microstructure of sintered β-SiC with 0.5 wt % B, 0.3 wt % Al and 1.5 wt % C by annealing between 1650-1850°C for 30 min before sintering at 2000°C. This prevented the formation of liquid phase, which in turn hindered the SiC polytype transformation and exaggerated grain growth.

1.2.5.2 Role of oxide additives

During pressureless sintering of SiC with alumina, Suzuki and Sasaki [65] observed fine plate-like interlocking grains. The grain growth proceeded predominantly in the basal plane with increasing sintering time. *Figure 1.11* summarises the three stages of microstructural development. The sintered body had no secondary phase along the grain boundaries, while aluminium oxide remained mainly at the triple points. Sasaki *et al.* [66], in a similar system, noted the presence of Si, C, Al, Ca and O on the surface of SiC

Green compact   **Initial stage**   **Intermediate stage**   **Final stage**

$\bigcirc$ β-SiC
● Al₂O₃

	Formation of liquid phase (Al₂O₃ rich)	**Solution-repreciptation**	**Transformation Decrease in amount of liquid phase**
	→ **Rearrangement**	→ **Grain growth (Plate-like-grains)**	
	→ **Densification**	**3C** → **4H**	
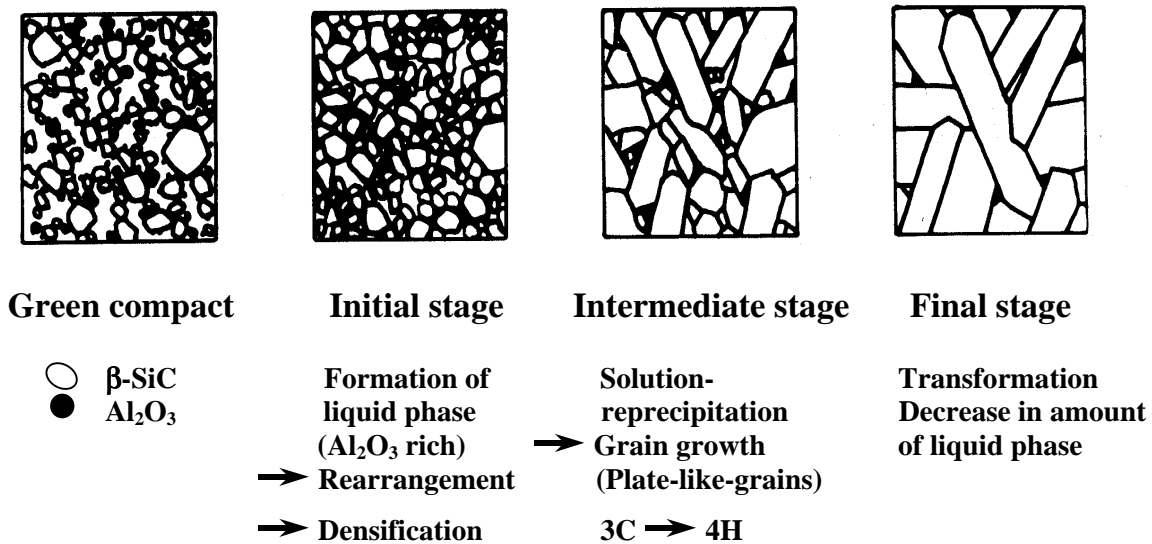
Figure 1.11: Schematic microstructure development of β-SiC with Al₂O₃ addition during pressureless sintering [65].

grains showing an intergranular fracture mode (2 wt % Al₂O₃, 5 h sintering). Micro-structural examination of β-SiC with addition of alumina-yttria revealed that most of the grains were uniform and equiaxed [48]. XRD patterns showed the presence of yttria-alumina-garnet eutectic liquid. β-to-α-SiC transformation was greatly reduced due to low temperature sintering. A polytype analysis of the relevant SiC peaks in XRD revealed that both the starting powder and the sintered body were dominated by the 6H structure [52]. It was also observed that an amorphous grain-boundary film was present between the SiC grains contrary to the findings of Suzuki and Masaki [65]. Grande *et al.* [53] found that a homogeneously distributed secondary phase formed during sintering of SiC with Al₂O₃-Y₂O₃. Coarsening of this phase occurred with increasing sintering time. An inhomogeneous microstructure developed during sintering at 1820°C (LPS-SiC) and the secondary phase was identified as YAG crystals. Lee and Kim [67] studied the pressureless sintering of β-SiC and α-SiC powders with addition of Al₂O₃-Y₂O₃ additives. The microstructure was highly dependant on the polytypes of the starting SiC powders. The microstructure of SiC obtained from α-SiC powder was composed of equiaxed grains, whereas SiC obtained from β-SiC powder was composed of a plate-like grain structure resulting from the grain growth associated with the β → α phase transformation. Kim *et al.* [68] annealed the hot pressed β-SiC powders sintered with large seed grains of α-SiC or β-SiC at 1850°C and investigated the microstructural development. The introduction of large seeds (0.44 μm as compared to 0.1 μm β-SiC

powders) accelerated the grain growth of elongated large grains during annealing, in which no appreciable $\beta \rightarrow \alpha$ phase transformation occurred. It was also observed that the growth of matrix grains was slower in case of β-SiC seeds. A bimodal microstructure of small and large elongated grains was obtained. In contrast, with α-SiC seeds, a uniform microstructure of elongated grains was found. They concluded that further optimisation of the microstructure could be possible with β-SiC seeds because of the remnant driving force for grain growth caused by the bimodal microstructure.

1.2.5.3 Effect of nitride and other additives

Rafaniello *et al.* [69] observed a phase separation leading to two phases having 2H (wurtzite) structure after annealing hot pressed SiC-AlN samples below ~2000°C. In a later work, Zangvil and Ruh [70] showed that at 2100-2300°C, the 4H solid solution was stable up to 14 mol % AlN whereas above 23 mol % AlN, the 2H (δ) solid solution was stable.

The system SiC-AlN-Al$_2$OC was investigated by Kuo and Virkar [71], and they also observed a homogeneous solid solution to undergo phase separation when annealed at temperatures lower than ~1900°C. The two phases formed here were also of the 2H type structure but with different compositions.

Both the SiC-AlN and SiC-AlN-Al$_2$OC systems exhibited the formation of either a modulated structure or very uniformly sized precipitates. The morphology of phase separation in these two systems was originally investigated by Kuo *et al.* [72,73]. In the SiC-AlN system, a basket-weave type of morphology was observed whereas in the AlN-Al$_2$OC system, the microstructure contained disk-shaped precipitates. The difference in morphology between the two systems was attributed to the orientation-dependent elastic energy function following the approach of Mayo and Tsakalakos [74]. Chen *et al*. [75] also observed the effect of coherency strain energy in the SiC-AlN pseudobinary system. Modulated, coherent, tweed-type structures were found at equimolar composition in the SiC-AlN system when annealed between 1600-1900°C. It was concluded that phase separation in this system under the conditions of composition and annealing temperature occurred by spinodal decomposition. In recent studies on the SiC-AlN-Y$_2$O$_3$ system, Nader [55] and Wiedmann [76] found that after sintering in N$_2$ atmosphere, the phases present in the system were mostly α-SiC (6H polytype) with Y$_{10}$Al$_2$Si$_3$O$_{18}$N$_4$ being the principle

secondary crystalline phase. They also noticed that after prolonged annealing for several hours at 1950°C, all the β-SiC transformed into α-SiC, mostly of the 6H and 4H polytypes, whereas the $Y_{10}Al_2Si_3O_{18}N_4$ decomposed into some oxide phases.

The effect of sintering atmosphere on microstructure evolution in sintered β-SiC (sintered at 2050°C for 1 h) was investigated by Jun *et al.* [57]. The microstructure consisted mainly of equiaxed grains irrespective of sintering atmosphere and AlN addition. However in samples which were annealed for 12 h at 1850°C after densification, the growth of large elongated grains was observed although the total rate of grain growth was low due to grain growth inhibition by N_2 atmosphere. N_2 significantly retarded both the β → α transformation and the anisotropic grain growth.

1.2.6 Mechanical properties

1.2.6.1 Strength

The strength of SiC sintered bodies depends on a number of factors including the mechanical testing method, strain rate, temperature, impurity level, size distribution of microstructural defects, and in some cases, on the orientation of the test specimen relative to the original material [77]. It was reported that surface flaws drastically lower the strength, which increases with increasing density of the sintered body. A study on the influence of the mechanical testing method revealed that the values of strength measured in tension were lower than those obtained in bending because a larger volume of material was tested. Although bending strength was independent of the orientation of the test specimen, higher values were obtained in the pressing direction of hot pressed SiC [77]. Inclusions played a significant role in determining the strength of fully dense material, as these inclusions were the crack initiating regions. The temperature dependence of the strength of hot pressed SiC containing B additions had been measured by Prochazka and Charies [78]. Edington *et al.* [77] also reported on the variation of bend strength with temperature in hot pressed SiC (*Figure 1.12*).

Dutta [79,80] in an extensive study noted that room temperature strengths were somewhat higher than those at 1370°C. Surface oxidation at 1370°C was found to be responsible for this phenomenon. Additions of boron and carbon were found to have negligible effect on the room temperature flexural strength of α-SiC while the bending strength at 1370°C was lower than the bending strength of commercially sintered α-SiC. Similarly, the bending strength was lower at 1400°C than at room temperature in the

case of both 2 wt % and 15 wt % Al$_2$O$_3$-added SiC [65]. However, bending strength showed a tendency to increase with sintering time for both 2 wt % and 15 wt % Al$_2$O$_3$. Jun *et al.* [57] reported the effects of additions of AlN, TiN additives to SiC and of the sintering atmosphere on the flexural strength. When sintering was carried out in N$_2$/Ar atmosphere, SiC with improved flexural strength was obtained due to a higher sintered density and fine grain size. AlN addition also showed a similar influence on the flexural strength. The bending strength increased with the amount of sintering aids. A maximum average 3-point bending strength of 953 MPa was obtained in a sample sintered in N$_2$/Ar with 16 wt % sintering aids. This value was much higher as compared to conventional Ar-sintered SiC [57]. Keppeler *et al.* [81] also investigated the high temperature bending strength and concluded that a globular LPS-SiC material showed an increase of strength in the temperature range between 1000°C to 1200°C due to healing of flaws and surface cracks by a glassy phase formed by oxidation. Higher strength will be achieved by proper microstructural design and minimising the size of defects through improved manufacturing processes [1].
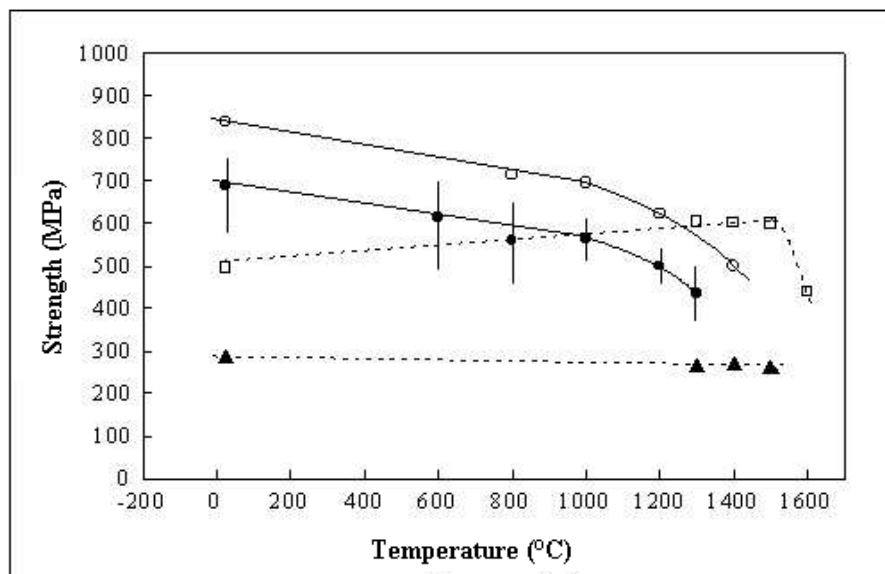
Figure 1.12: The variation of bend strength with temperature in hot pressed SiC. The open circles are three point bending data for a material hot pressed with B additives, while the closed circles are four point bending measurements for the same material. The open squares are three point bending data of the best boron containing material while the closed triangles are also three point bending data of the same material but containing coarse α-SiC grains [77].

1.2.6.2 Fracture toughness

The K_{Ic} value of SiC was shown [82] to increase with decreasing grain size and optimum fracture toughness was obtained for grain sizes less than 10 µm. Schwetz and Lipp [83] determined the value of K_{Ic} at room temperature and at 1200°C using the SENB (Single Edge Notched Beam) method for SiC sintered with the additive systems B+C and Al+C. The results showed that the room temperature K_{Ic} values of both materials were identical. However, with increasing temperature, the fracture toughness also increased, and this was much more pronounced in the B+C system. Grathwohl *et al.* [84] also investigated a similar system and found that all materials exhibited a moderate resistance against fatigue at 1300°C. The fracture mode was found to be clearly different for B+C and Al+C additive systems.

Suzuki and Sasaki [65] reported the K_{Ic} values of sintered SiC with 2 wt % and 15 wt % Al_2O_3 and found that K_{Ic} increased with sintering time. After 24 h of sintering, the sintered SiC with 15 wt % Al_2O_3 revealed a K_{Ic} of 5.7 MPa·m$^{1/2}$ which was twice the fracture toughness of B-doped sintered α-SiC (2-3 MPa·m$^{1/2}$) [85]. This value was also higher than K_{Ic} of 3-4 MPa·m$^{1/2}$ for an Al_2O_3-fluxed hot pressed SiC [85]. The K_{Ic} values strongly depended on the aspect ratio of the grains. Higher aspect ratio increased the K_{Ic} value owing to the resulting microstructure with interlocking plate-like grains. Improved fracture behaviour of novel SiC ceramics having rod-like whisker grains was observed by Kodama and Miyoshi [86]. They concluded that the fracture toughness of these ceramics was higher than that of ordinary SiC and its maximum value was 7.3 MPa·m$^{1/2}$. Grain pullout, grain bridging and crack deflection were considered to be the main operative mechanisms that led to improved fracture toughness. Based on these toughening mechanisms, Lee and Kim [67] and Cao *et al.* [87] improved the fracture toughness of β-SiC sintered with Al-B-C additives. Lee and Kim [66] also showed that with α-SiC starting powder, the fracture toughness increased slightly upon annealing whereas in the case of β-SiC powder, it increased significantly which was attributed to crack bridging and crack deflection by the plate-like grains. Keppeler *et al.* [81] also observed a similar mechanism in a material liquid phase sintered from 99 wt % β-SiC and 1 wt % α-SiC, although they considered that pullout of platelets was not a toughening mechanism as platelet grains with an orientation normal to the crack propagation were broken without any debonding.

1.2.6.3 Creep and high temperature strength

Creep of hot pressed SiC has been investigated between 1900°C and 2200°C and it was concluded that the creep of these forms of SiC was controlled by grain boundary diffusion which is influenced by free carbon [88,89]. The creep properties of SiC sintered bodies containing Al were somewhat different from those which were produced with B+C sintering additive. It was observed that the high temperature creep rate was much higher than for those not containing Al because the aluminium accelerated the diffusion within the materials [32]. Suzuki and Sasaki [65] confirmed that SiC with the addition of Al_2O_3 had a higher creep rupture resistance up to 1200°C in air than B-doped sintered α-SiC.

Yarnada and Mohri [1] reviewed that SiC possessed better high-temperature strength at temperatures above 1000°C than any other materials, including metals. There was a tendency for the strength of SiC to increase at high temperatures, and stress relaxation at the crack tip was reported as a possible mechanism responsible for this.

1.2.6.4 Fatigue resistance

Suzuki [51] reported the results of static and low-cycle fatigue tests for Al_2O_3 doped SiC. It was observed that in the static fatigue test, the time-to-rupture vs. stress curve was virtually horizontal up to 1200°C, the number of fatigue cycles (N) being 100 or more, and there was no evidence of slow crack growth. Another work [90] on a comparable material exhibited an N value of 27 at 1200°C accompanied by fatigue. A drop in the N value (for N = 27) and slow crack growth were also observed for Al_2O_3-added pressureless sintered SiC at 1400°C. The results of low cycle fatigue tests were similar to those of the static fatigue test, indicating the superior fatigue resistance of SiC sintered bodies.

1.2.7 Oxidation resistance

Suzuki [51], in his review, reported the oxidation-induced weight gain and change in strength before or after oxidation of hot isostatically pressed (HIPed) SiC. It was found that at 1200°C and 1300°C weight gain increases linearly with the square root of oxidation time and the kinetics are parabolic up to 1000 h. It was also noticed that although room-temperature strength dropped by 11 %, there was no change in the strength at 1300°C after oxidation for 1000 h.

It was further concluded that the lower the alumina content, the better the resistance to oxidation. A sintered body with a density of at least 99 % and containing less than 3 wt % Al_2O_3 exhibited superior oxidation resistance with a weight gain of less than 1 mg/cm^2 after oxidation for 1000 h at 1300°C [51].

1.3 Scope of the present investigation

Many studies have been carried out in recent years using rare-earth sesquioxides as densification additives for Si_3N_4 and SiAlON ceramics [3-8]. These new rare-earth sesquioxides additive systems were introduced for the modification of the grain boundaries by highly refractory crystalline rare-earth disilicates ($RE_2Si_2O_7$) leading to improved high temperature properties. Moreover, it has been observed that the solubility of N in oxynitride glasses containing rare-earth oxides can reach higher levels as compared to the conventional additive systems [89]. The glass transition temperatures and softening points of oxynitride glasses are significantly higher than those of silicate glasses [91], contributing to superior high-temperature properties of the sintered ceramics. Combinations of either Al_2O_3 or AlN with Y_2O_3 (or a rare-earth sesquioxide) have been reported to facilitate sintering to high densities tremendously [47-51]. However, Al-containing compounds tend to compromise the refractoriness because Al^{3+} can act both as a network former and a network modifier in silicate glasses [92,93], thereby lowering their softening points. Therefore, additional efforts were directed to replace the Al-containing compounds by using two different rare-earth sesquioxides in combination. In this case, the melting point depression in the $RE_2^I O_3$ - $RE_2^{II} O_3$ systems at intermediate composition is exploited for the formation of a liquid phase. Based on this philosophy, rare-earth oxide-containing systems were introduced into SiC as sintering additives in order to study the effect of these oxides on sinterability, phase evolution and α-to-β-SiC transformation, oxidation behaviour, mechanical and high temperature thermo-mechanical behaviour.

2 Fundamentals

This chapter explains the theory and basic mechanisms of liquid phase sintering as far as it is applicable to the present investigation. Apart from that, criteria for selecting individual rare earth sesquioxides as candidates for sintering additives of SiC are elaborated. Basic principles and explanations are given on important mechanical properties like fracture toughness, strength and thermo-mechanical behaviour. Oxidation mechanisms are discussed in the light of different rare earth cations and phase composition.

2.1 Sintering theory

The technique of liquid phase sintering is quite old and has been used in the manufacture of ceramics for many centuries [94]. Liquid phase sintering is of great value in fabricating several unique materials to near net shapes and will continue to expand in application as the fundamental attributes are better appreciated. Liquid phase sintering is classically defined as sintering involving a particulate solid and coexisting liquid during the sintering process. The liquid can result from melting of one component or formation of a eutectic due to the interaction of two or more components. The liquid may be transient or persistent during sintering depending on the solubility relationships. The kinetics of liquid phase sintering largely depend on the solubility of the solid in the liquid, the interfacial energies between the liquid and solid phases (wetting), and the penetration of the liquid along solid-solid grain boundaries. These variables, coupled with processing parameters like particle size and size distribution, sintering temperature, time, atmosphere and green density, have large effects on the characteristics of materials formed by liquid phase sintering. The interdependence of all of these factors contributes to the difficulty in understanding the mechanisms of liquid phase sintering.

The mechanisms of liquid phase sintering have been extensively discussed by Kingery [94,95], Petzow *et al.* [96] and German [97]. Classically, the following sequence of sintering stages is thought to be prevailing.

1. Particle rearrangement

Densification results from particle rearrangement under the influence of capillary forces and the filling of pores by the liquid phase. Due to this mechanism, much faster densification occurs during the early stage of sintering than in solid state sintering. Parameters like the liquid volume fraction, solubility, green density, temperature, wetting, etc., strongly affect this process.

2. Solution-reprecipitation

A general attribute of solution-reprecipitation processes is microstructural development, shape accommodation and grain growth. Due to the chemical potential gradient generated by capillary forces, smaller grains dissolve in the liquid and through diffusion, matter is transported to the larger grains where it re-precipitates. This process is analogous to Ostwald ripening. The process alters the grain shape, commonly termed as grain shape accommodation, thus leading to pore elimination, and hence shrinkage and densification occurs.

3. Solid-state or skeleton sintering

The last stage is referred to as solid state controlled sintering. The overall shrinkage and densification is very sluggish due to the rigidity of the solid skeleton that inhibits further rearrangement, although microstructural coarsening continues by grain boundary diffusion. A schematic diagram of a typical shrinkage curve showing the three stages of liquid phase sintering is presented in *Figure 2.1*.
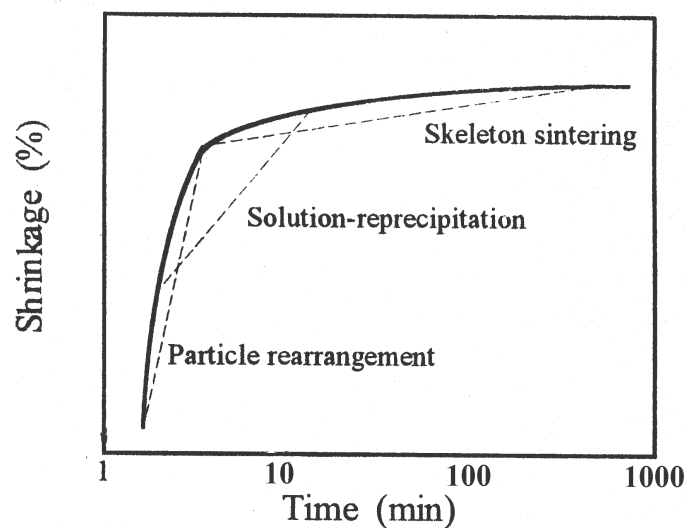
Figure 2.1: Schematic shrinkage curve for the three stages of liquid phase sintering.

2.2 Rare earth sesquioxides as components of additive systems

2.2.1 Role of rare earth oxides

One problem associated with the use of additives in liquid phase sintering processes is the resultant degradation of high temperature properties due to residual glassy grain boundary phases [98,99]. The basic phenomenon can be explained by the Zachariasen-Warren model for oxide glasses [100]. Cations of the additives enter into the voids formed by SiO_4^{4-} tetrahedra as network modifiers, leading to more open structures which in turn lowers the glass transition temperature [92,93] (*Figure 2.2*). Addition of rare earth (RE) oxides also exhibits similar behaviour within the silica network [101,102]. However, replacing Y^{3+} with smaller rare earth cations (e.g. Lu^{3+}) increases the glass transition temperature. In this regard, their advantage over the conventional additive systems (Al_2O_3-Y_2O_3 or AlN-Y_2O_3) is the more refractory nature of grain boundary phase formed in rare earth oxide systems. On the other hand, Al^{3+}, having an amphoteric nature in the silicate structure, leads to formation of non-bridging oxygens by substituting Si^{4+} (glass former with reduced number of bonds) and at the same time creates a more open structure by breaking the Si–O bonds in the silica network (glass modifier) [103,104] (*Figure 2.2(b)*). Both effects lead to a drop in glass transition temperature [103]. So, in Al^{3+}-free

(a) a-SiO$_2$ (Si: "Network former")   (b) a-SiO$_2$ / Al^{3+}, RE^{3+} ("Network modifier")
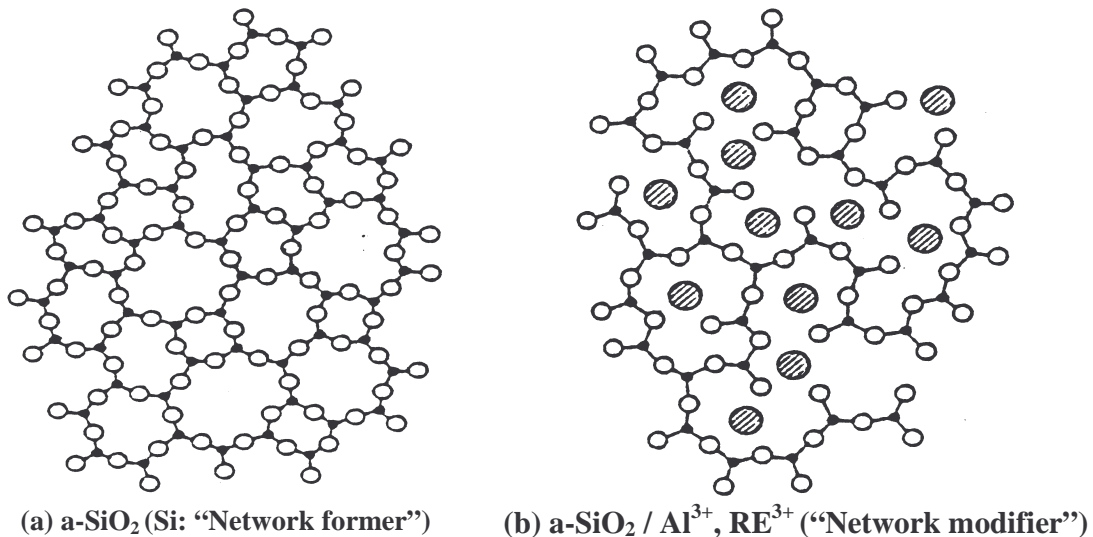
Figure 2.2: Schematic view of (a) a pure silica network and (b) silica network after addition of another cation.

RE$_2$O$_3$-based additive systems, increase in glass transition temperature may be possible in two ways.

In general, the physical properties of a glass are predominantly controlled by the bond strength between cations (Si^{4+} or the cation of oxide additives) and the anions (O^{2-}). The high temperature properties of a SiO$_2$–based glass are believed to be determined by the weakest bond [105]. The bond strength is characterised as a "field strength" which is proportional to the ionic charge and the reciprocal of the ion size [106] and is expressed as :

$$F_c = \frac{Z_a e\, Z_c e}{a^2} \cdot \frac{1}{4\pi\,\varepsilon_0} \tag{2.1}$$

where F_c is the field strength, Z_a is the charge of the anion, Z_c is the charge of the cation, e is the elementary electric charge, a is the distance between the center of the two ions and ε_0 is the vacuum dielectric constant.

Considering the crystal field theory, the bond strength between the cation of the oxide additive and the oxygen ion is expected to increase with decreasing cationic radius. It is also known that in some complex oxides, trivalent rare earth ions take higher coordination states compared to other trivalent cations (i.e., CN > 6) [93]. This is also attributed to the strong ionicity of the RE–O bond and will lead to different ordering in the glass structure that may influence the glass transition temperature.

2.2.2 Criteria for the selection of rare earth oxides

1. Melting point depression

The rare earth sesquioxides are oxides with very high melting point (ranging from 2200-2500°C). This limits their use as single component sintering additives. But a combination of two or more oxides along with SiO$_2$ (present on the surface of SiC) can lead to a melting point depression of 300-400°C (see the Sc$_2$O$_3$-Y$_2$O$_3$ phase diagram in *Figure 2.3* [107]), allowing liquid phase sintering within viable temperature regions. So far, very little literature has been published on the phase diagrams of these oxide systems, hence

the well-established Sc_2O_3-rare earth oxide systems were used as a guideline in these investigations.

2. Cationic radius difference

It has been observed that when the ratio of the ionic radii, $r_{RE^{3+}} / r_{Sc^{3+}}$ is greater than 1.2, an orthorhombic perovskite type of structure is formed leading to more complicated phase diagrams (e.g., the Sc_2O_3-La_2O_3 phase diagram in *Figure 2.3* [107]). The resultant eutectics between $ScREO_3$ and the end members usually do not cause melting at temperatures significantly lower than 2000°C. The melting point depression that arises for those combinations with $r_{RE^{3+}} / r_{Sc^{3+}} < 1.2$ leads to melting in combination with the SiO_2 present as impurities in SiC powders.
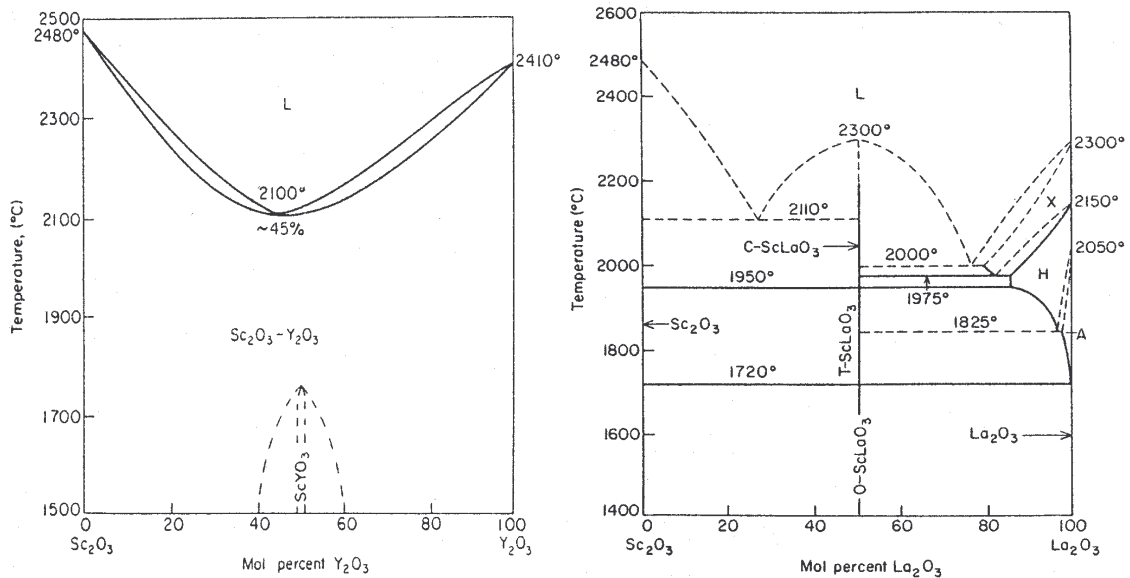
Figure 2.3: The Sc_2O_3-rare earth sesquioxide phase diagrams [107].

In order to classify these two types of phase diagrams, a tolerance factor, *t*, was introduced :

$$t = (R_A + R_o) / \sqrt{2} \, (R_B + R_o) \qquad\qquad (2.2)$$

where R_A, R_B and R_o are the radius of the larger cation, smaller cation and anion, respectively. It has been shown that perovskite-type compounds may form if the tolerance factor lies between 0.825 and 1 [107].

2.3 Theory on mechanical properties

2.3.1 Strength of ceramics

Tensile testing of ceramics is not only time consuming, but it is also expensive to fabricate the specimens. Therefore, the easier-to-handle transverse bending or flexure test is commonly used for determining the strength of ceramics. Here, the specimen is loaded up to failure in either three- or four-point bending geometry. The maximum stress or stress at fracture is commonly referred to as fracture strength. For rectangular cross sections, the fracture strength in four-point bending is given by :

$$\sigma_{4P} = \frac{3}{2} \cdot \frac{F(l_o - l_i)}{b h^2} \qquad (2.3)$$

where F is the force (N), l_o is the length between two outer supports (40 mm), l_i is the length between two inner supports (20 mm), b and h are the breadth and height of the specimen, respectively.

The flexural strength of a sintered body is strongly dependent on such factors as size, shape, density, and distribution of residual pores, agglomerates, surface flaws, inclusions and their distribution, grain size and grain boundary properties (bonding strength).

Pores are usually quite deleterious to the strength of ceramics not only because they reduce the cross-sectional area over which the load is applied, but also because they act as stress concentrators. Typically, the strength and the porosity have been related by the following empirical relationship [108] :

$$\sigma_P = \sigma_0 \, e^{-BP} \qquad (2.4)$$

where P, σ_P and σ_0 are, respectively, the volume fraction of the pores and the strength of the specimen with and without porosity. B is a constant and depends on the distribution and morphology of the pores.

Agglomerates and large grains cause degradation in strength. During sintering, the rapid densification regions containing agglomerates can induce stresses within the surrounding compact facilitating the formation of voids and cracks. Anisotropic large grains often produce mismatch in thermal expansion and elastic modulus and act as flaws in a homogeneous matrix.

Surface flaws can also degrade the mechanical performance to a greater extent. They can be a result of post-fabrication machining operations, or accidental damage to the surface during use. During high temperature testing, grain boundary grooving can result in lower flexural strength. According to the Griffith criterion [109], the fracture stress is expected to decrease with increasing flaw size.

Empirically, the strength of ceramics (σ) shows an inverse correlation with the average grain size ($\overline{G}$). In general, the σ vs. $\overline{G}^{-1/2}$ relationship for ceramic materials shows two branches : one branch at larger grain sizes showing a strong grain size dependence of the strength (Orowan branch), and another branch at smaller grain sizes where extrinsic factors, such as, surface finish, preferred orientation, pores and inclusions dictate the strength of the ceramics (Petch or Hall-Petch branch) [110]. Carniglia [111] suggested that microplasticity was the failure mechanism for the fine-grain branch whereas for large grains, Griffith flaw failure operates with the critical flaw dimensions being close to the grain size. So, invoking the Orowan-Petch relationship, one expects the strength to be proportional to $\overline{G}^{-1/2}$ for larger grain size [110]. In the present investigation, Orowan branch behaviour is ruled out as the grain sizes lie between 1-5 µm.

Apart from the above-mentioned factors, residual stresses, crack velocity, elastic anisotropy and temperature influence the flexural strength of ceramics [110]. Strengthening can occur by introduction of a compressive surface layer that inhibits surface cracks to propagate. Similar strengthening can occur when a protective, usually oxide, layer forms on the surface, which tends to blunt and partially heal pre-existing flaws or surface cracks leading to higher strength values. On the contrary, during high temperature testing, surface pits or etching of the surfaces occur that can result in a drop in strength. At high temperature, ceramics containing amorphous intergranular phases

exhibit a drop in strength value which is usually related to the softening of the above mentioned phases.

2.3.2 Fracture toughness

Vickers hardness indentations as a means to measure the K_{Ic} have become quite popular due to the simplicity of the method. In this method, a diamond indenter is penetrated into the surface of the specimen to be tested. Upon removal of the indenter, the lengths of the cracks that emanate from the edges of the indent are measured, and the Vickers hardness H in GPa of the material is calculated [108]. A number of empirical and semi-empirical relationships have been proposed relating K_{Ic} to the crack length, and in general the expression take the form as given below [112] :

$$K_{IC} = \Phi \sqrt{a}\, H \left(\frac{E}{H}\right)^{0.4} f\left(\frac{c}{a}\right) \qquad\qquad (2.5)$$

where Φ is a geometric constant, E is Young's modulus, f is a geometric function depending on the crack length (c) and the diagonal of the Vickers indentation ($2a$). It should be emphasised that the K_{Ic} values measured by this technique are usually not as precise as those from other macroscopic tests, especially the single edge V-notched beam (SEVNB) test [108].

The average stress intensity at the crack tip is reduced in polycrystalline materials containing glassy grain-boundary phases, as the crack is deflected along the weak grain boundaries. This is because the stress is no longer always normal to the crack plane leading to an increase in the fracture toughness which can be calculated by the equation :

$$K_{tip} = \left(\cos^3 \frac{\theta}{2}\right) K_{app} \qquad\qquad (2.6)$$

where K_{tip} = stress intensity at tip, K_{app} = applied stress intensity and θ = deflection angle [108].

In crack-bridging situations, the toughening results from bridging of the crack surfaces behind the crack tip by a strong reinforcing phase. These bridging ligaments generate closure forces due to elastic stretching and hence reduce the crack-tip stress [113].

2.3.3 Creep

Progressive deformation of a material at constant stress is called creep. The creep response of a solid can be obtained by measuring the strain rate as a function of the applied load. Typically, strain versus time curves (*Figure 2.4*) are obtained by measuring the deformation as a function of time at constant load or stress at a specific temperature. In general, three regions can be observed in an ideal creep curve: (1) primary creep where the creep rate decreases with time, (2) secondary or steady state creep in which the creep rate changes little with time and (3) finally, tertiary creep where the strain rate increases rapidly with time prior to fracture. In liquid phase sintered ceramics, the secondary creep region is usually not reached within experimentally accessible time intervals.
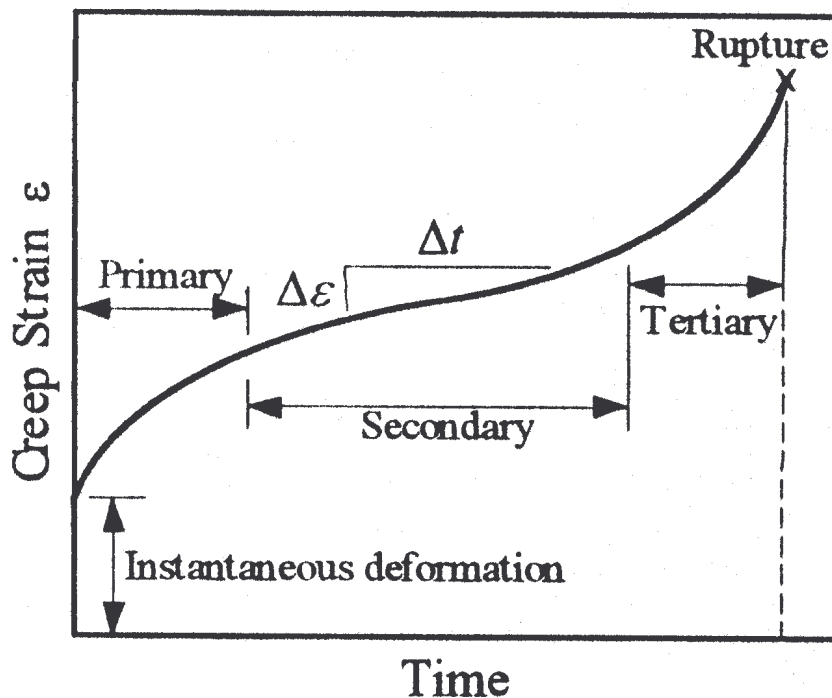
Figure 2.4: Typical strain versus time creep curves showing three regions of creep [107].

Another way of representing creep data is by plotting the logarithm of the steady-state creep rate ($\dot{\varepsilon}$) versus the logarithm of the applied stress (σ) at a constant temperature. Such curves usually yield straight lines, which can be expressed mathematically like the following [108] :

$$\dot{\varepsilon} = \frac{\partial \varepsilon}{\partial t} = \Gamma \sigma^P \qquad (2.7)$$

where Γ is a temperature-dependent constant, and P is called the power law exponent. The value of P generally lies between 1 and 8.

A great deal of research has been carried out to elucidate the mechanisms leading to the observed functional dependence of the creep rate. The main creep deformation mechanisms can be grouped into three categories: diffusion, viscous flow, or dislocation creep.

Depending on the material transport path (either bulk or grain boundary), diffusional creep mechanisms can be classified into two groups namely Nabarro-Herring and Coble creep. At higher temperatures, Nabarro-Herring creep is predominant, i.e., diffusion occurs through the bulk. The strain rate is given by [108] :

$$\dot{\varepsilon} = \frac{8\sigma\,\Omega_i\,D_i}{k\,T\,G^2} \qquad (2.8)$$

where Ω_i = atomic volume, D_i = diffusivity of the atom and G = grain size.

However, at lower temperature, or for very fine-grained solids, grain boundary diffusion is predominant leading to Coble creep, and the creep rate becomes [108] :

$$\dot{\varepsilon} = \Psi \frac{\sigma\,\Omega_i\,\delta_{gb}\,D_{gb}}{k\,T\,G^3} \qquad (2.9)$$

where δ_{gb} = grain boundary width with Ψ is a numerical constant $\approx 14\pi$, D_{gb} = grain boundary diffusivity.

Viscous creep is significant for many structural ceramics containing glassy grain boundary phases and it is now well known that for many of them, the main creep mechanisms are not diffusional but rather result from the softening and viscous flow of these glassy phases. Several mechanisms have been reported to explain the observed phenomena, among which the following three are most important: (1) solution-reprecipitation, which is similar to the process observed in liquid phase sintering, (2) viscous flow, where the glass phase softens at higher temperature resulting in a flow of the intergranular glassy phase under an applied stress and (3) viscous creep cavitation where the time-dependent accumulation of creep damage (either bulk or localised damage) eventually causes failure of the material. The damage accumulation depends on several factors such as microstructure, volume of the amorphous phase, temperature and applied stress. The mechanisms (1) to (3) are usually associated with power law exponents in the range 1 to 3.

Dislocation creep mechanisms are operative at higher temperature and applied stress where the power law exponents are in the range of 3 to 8. Creep occurs by movement of atoms from the region of compression to the region of tension via dislocation glide or climb.
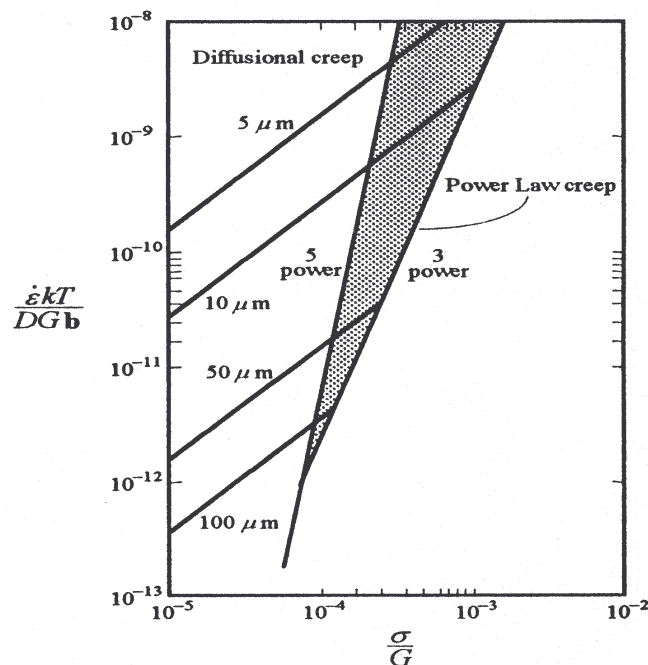
Figure 2.5: Effect of grain size on normalised creep rate versus normalised stress [108].

Grain size also influences the creep behaviour at lower stress levels. *Figure 2.5* schematically summarises the creep behaviour over a wide range of applied stress as a function of the grain size, neglecting viscous creep mechanisms (power law exponent ≥ 3). From the figure, it is obvious that small grains are detrimental to the creep rate at lower stress.

2.3.3.1 Formulation of creep parameters

The steady state creep deformation of ceramics under sustained loading conditions normally exhibits a power-law stress-dependent behaviour [114]. The stationary creep is expressed by Norton's power-law for elementary analysis :

$$\dot{\varepsilon} = A \cdot \sigma^n \cdot e^{-Q/RT} \qquad\qquad (2.10)$$

where $\dot{\varepsilon}$ is the secondary creep rate, A is a pre-exponential constant, n is the stress exponent, Q is the activation energy associated with the operating creep mechanism, R is the universal gas constant and T is the test temperature in K.

Although four-point bending creep tests have essential advantages in the testing procedure as compared to tensile or compression creep tests, they do not provide an accurate analysis of the creep test results in terms of creep mechanisms due to certain assumptions.

In the present analysis, the assumption is made, after Hollenberg *et al.* [115], that the part of the sample which experiences tensile stress behaves similar to its compressive counterpart. This simplifies the analysis substantially and allows the solutions to be presented in closed form, as the neutral axis is assumed to be located at the geometric center of the rectangular bending specimen irrespective of the magnitude of the applied load.

The stationary stress distribution over a bending bar of height h was given by Timoshenko [116]. He formulated the stress in the outer fiber (σ_{max}), i.e., at $h/2$, which is given by :

$$\sigma_{max} = \frac{3(l_o - l_i)F}{bh^2}\frac{(2n+1)}{3n} \qquad (2.11)$$

where l_o and l_i are the length between the two outer and inner supports, respectively, F = force, b = breadth of the specimen, n = stress exponent.

In polycrystalline SiC-ceramics containing a secondary phase, grain boundary diffusion along with grain boundary sliding play predominant roles in creep deformation [117-120]. These creep mechanisms exhibit a stress exponent of n ~ 1 at T ≤ 1500°C in air. So, by inserting n = 1, the stress can be calculated based on elastic theory and is given as :

$$\sigma_{max} = \frac{3(l_o - l_i)F}{bh^2} \qquad (2.12)$$

Specimen displacement under constant load is calculated from geometric considerations and for small deflections, the maximum strain is formulated as [115] :

$$\varepsilon = \frac{4h}{s^2}\cdot\delta \qquad (2.13)$$

where ε is the maximum strain in the outer fiber, δ is the deflection at the loading points and s is the distance between the loading points (s = l_i).

2.4 Oxidation

In recent years much work has been done to elucidate the oxidation processes in Si_3N_4- and SiC-based ceramics. In spite of rigorous efforts, however, there is still no general agreement on the factors governing the oxidation kinetics. Silicon-based ceramics exhibit two types of oxidation behaviour, passive and active oxidation, depending on partial pressure and temperature [121,122]. Passive oxidation is observed under high oxygen

partial pressure, in which a protective SiO_2 film prevents further oxidation. In the case of silicon carbide oxidation, this can be expressed as :

$$SiC\ (s) + 3/2\ O_2\ (g) \rightarrow SiO_2\ (s) + CO\ (g) \qquad (2.14)$$
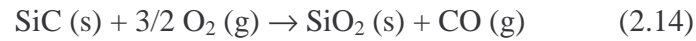
Active oxidation occurs at low oxygen partial pressure, and no protective films are expected in this case because of significant SiO vapour formation following the equation :

$$SiC\ (s) + O_2\ (g) \rightarrow SiO\ (g) + CO\ (g) \qquad (2.15)$$
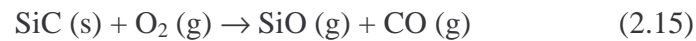
Passive and active oxidation leads to mass gain and loss, respectively. Under normal atmospheric conditions, the passive oxidation predominates. In dry atmosphere, the oxidation mechanism of SiC can be explained in terms of a parabolic rate law below the melting point of cristobalite (1728°C) [123]. The oxidation behaviour of sintered specimens containing additives, in particular, obeys a parabolic rate law of the type :

$$\Delta W^2 = k_p\ t + Q \qquad (2.16)$$

where ΔW is the weight gain per unit surface area, k_p is the rate constant of parabolic oxidation, t is the exposure time and Q is an additive constant (ideally = 0). The parabolic equation, which can be derived from Fick's first law of diffusion, implies that the oxidation rate is diffusion controlled, either by oxygen diffusing through a growing silica/silicate layer or by cations diffusing through the oxide layer in the opposite direction. It is also quite clear that the oxidation behaviour is not only dependent on the partial pressure of O_2 and on the temperature, but also on the grain boundary phase composition, structure and amount in case of LPS-SiC ceramics [124].

3 Experimental procedures

3.1 Preparation of LPS-SiC ceramics

3.1.1 Raw materials and greenbody fabrication

The starting materials used to fabricate green bodies are commercially available α-SiC, β-SiC, RE_2O_3 (RE = Gd, Dy, Ho, Er, Lu, Y, Sc) and AlN powders. The characteristics of these powders are given in *Table 3.1*. Compositional variation is done by combining either two rare earth sesquioxides or AlN and Lu_2O_3 in equimolar amounts or different molar ratio in the additive systems. The powder specifications and denominations are detailed in *Table 3.2*. Sintering experiments are performed in order to test the effectiveness of these additives for complete densification of SiC.

Table 3.1: *Characteristics of starting ceramic powders*

Powder	Manufacturer	Chemical Analysis (wt%)	Particle Size Distribution			Specific Area (m^2/g)	Density (g/cm^3)
			$d_{10}(\mu m)$	$d_{50}(\mu m)$	$d_{90}(\mu m)$		
α-SiC	A-10, H.C.Starck Germany	C-30.0, O-0.9, Al-0.03, Ca-0.01, Fe-0.05	0.18	0.51	1.43	11.1	3.22
β-SiC	BF-12, H.C.Starck Germany	C-30.0, O-1.2, Al-0.05, Ca-0.005, Fe-0.03	0.25	0.89	3.5	17.8	3.22
AlN	Grade C, H.C.Starck	N-30.0, C-0.1, O-2.5, Fe-0.005	0.34	0.92	3.07	5.0	3.26
Y_2O_3	Grade C, H.C.Starck	Al-0.005, Ca-0.003, Fe-0.005	1.21	4.48	8.08	12.9	5.02
Gd_2O_3	STREM CHEMICALS USA	99.99% Gd	~1-2 μm			—	7.41
Dy_2O_3		99.90% Dy	< 65 μm				7.81
Er_2O_3		99.99% Er	< 65 μm				8.66
Lu_2O_3		99.90% Lu	—				9.45
Sc_2O_3		99.90% Sc	< 65 μm				3.85
Ho_2O_3	Alfa Aesar, Germany	99.99% Ho	4 – 5 μm			—	8.36

The powder mixtures are prepared by attrition milling for 4 h in isopropanol with Si_3N_4 milling media using a polyamide container and stirrer. The slurry is separated from the milling media via a sieve chain and is subsequently dried in a vacuum evaporator. Completely dried powders are obtained after 15 h of drying at 60°C in a drying oven. The processed powders are then sieved to obtain granules with a maximum size of 160 µm. Then the premixes are encapsulated within rubber dies and cold isostatically pressed (Paul Schaefer, KIP 100) at a pressure of 240 MPa for bar-shaped specimens of the dimension ~55 mm × 15 mm × 12 mm or at a pressure of 600 MPa into cylinders of 15 mm ⌀ × 12 mm. A flow chart of the preparation method is sketched in *Figure 3.1*.

Table 3.2: Specifications of the starting powders

Powder Denomination	SiC (vol%)	Additive (vol%)	α-SiC : β-SiC (mol%)	Additive composition (mol%)
1Gd-1Er	90	10	10:90	$50Gd_2O_3 : 50Er_2O_3$
1Gd-1Ho	90	10	10:90	$50Gd_2O_3 : 50Ho_2O_3$
1Gd-1Lu	90	10	10:90	$50Gd_2O_3 : 50Lu_2O_3$
Sc	90	10	10:90	$100Sc_2O_3$
Lu	90	10	10:90	$100Lu_2O_3$
1Dy-1Lu	90	10	10:90	$50Dy_2O_3 : 50Lu_2O_3$
1Dy-1Ho	90	10	10:90	$50Dy_2O_3 : 50Ho_2O_3$
2Dy-1Ho	90	10	10:90	$66.7Dy_2O_3 : 33.3 Ho_2O_3$
1Dy-2Ho	90	10	10:90	$33.3Dy_2O_3 : 66.7 Ho_2O_3$
1Dy-1Y	90	10	10:90	$50Dy_2O_3 : 50Y_2O_3$
1Ho-1Lu	90	10	10:90	$50Ho_2O_3 : 50Lu_2O_3$
1Lu-1AlN	90	10	10:90	$50 Lu_2O_3 : 50AlN$
2Lu-1AlN	90	10	10:90	$66.7Lu_2O_3 : 33.3AlN$
1Lu-2AlN	90	10	10:90	$33.3Lu_2O_3 : 66.7AlN$
1Y-1Lu	90	10	10:90	$50Y_2O_3 : 50Lu_2O_3$
1Y-1AlN	90	10	10:90	$50Y_2O_3 : 50AlN$
3Y-2AlN	90	10	10:90	$60Y_2O_3 : 40AlN$
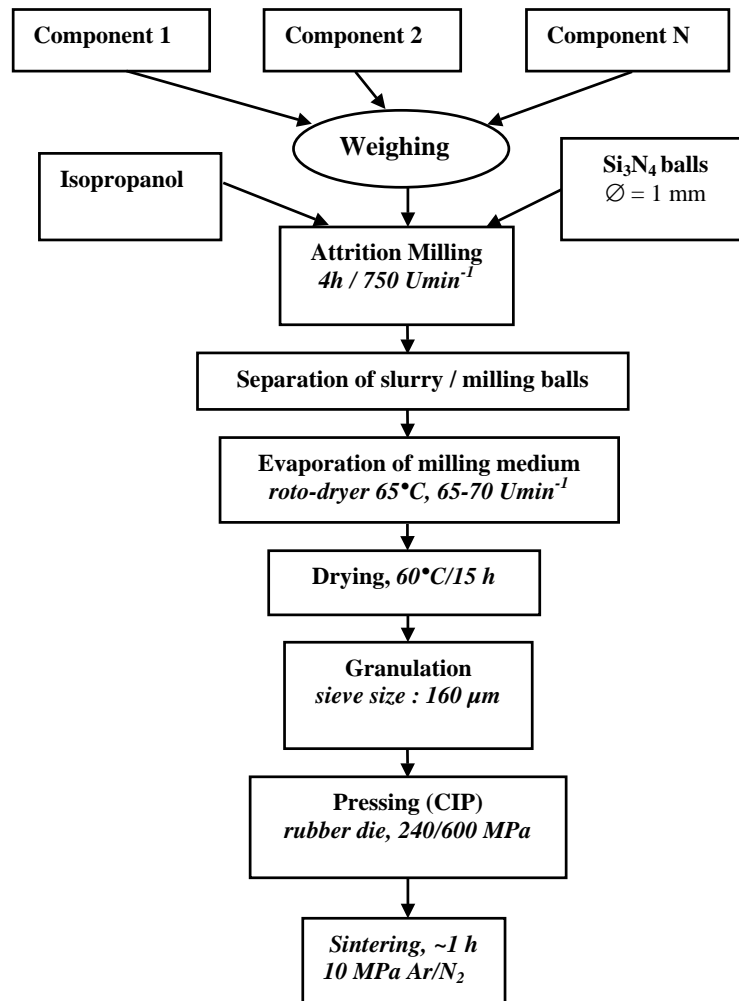
Figure 3.1: Schematic diagram of sample preparation method.

3.1.2 Dilatometric studies

In order to understand the densification behaviour of different powder compositions, a series of dilatometric experiments are performed with a high temperature differential dilatometer. Cylindrical samples (8 mm $\varnothing \times$ 12 mm) are weighed and placed inside a graphite heated furnace (FCT F8205) containing the dilatometric set-up. The linear shrinkage is monitored as a function of temperature with the help of an integrated PC-software. The samples are first heated in vacuum upto 1100°C, then under an overpressure of 0.2 MPa N_2 until 2150°C. The heating rate is 20 K/min upto 1500°C, followed by 10 K/min to 2150°C with a holding time of 15 min at the peak temperature. The schematic dilatometric heating and cooling cycle is depicted in *Figure 3.2*.
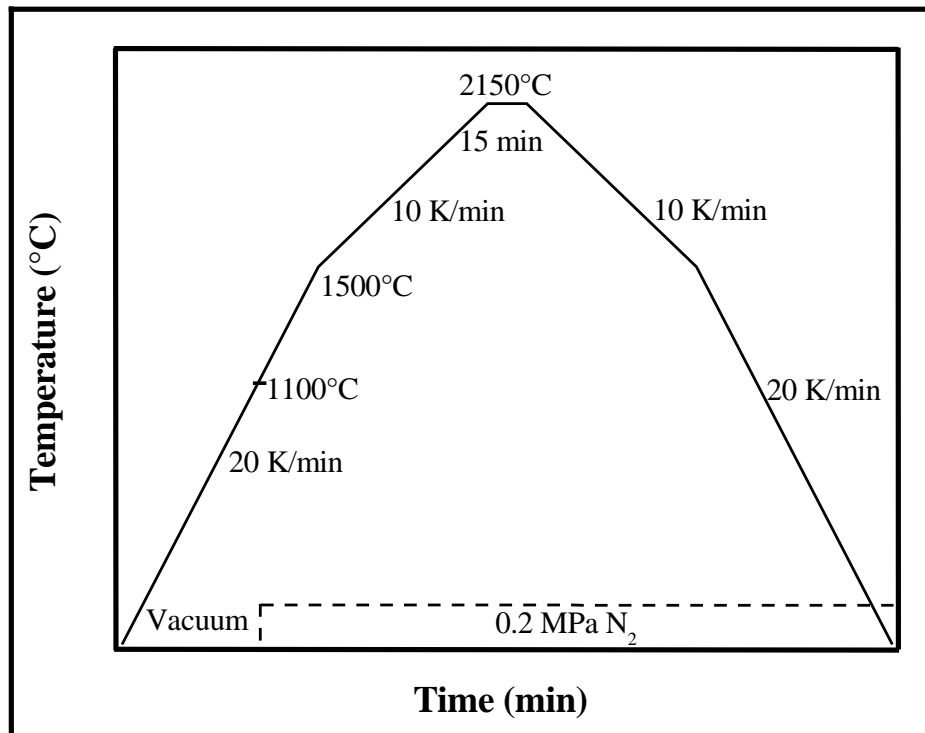
Figure 3.2: Schematic diagram of dilatometric cycle.

3.1.3 Densification process

The densification behaviour is investigated by using two different graphite heated gas pressure furnaces manufactured by Astro Industries (USA) and FCT (Germany), respectively. Temperature is controlled by a boron carbide/graphite thermocouple in the case of the Astro furnace and by pyrometer in the case of the FCT F8205 furnace. The maximum gas pressure that can be achieved is 1.5 MPa with the Astro furnace and 10 MPa with the FCT furnace. In a later stage, sintering experiments are performed in the FCT furnace utilizing nitrogen or argon atmospheres. The densification behaviour is monitored as a function of different temperature cycles and gas atmospheres in order to optimise the sintering conditions. The peak temperature is varied from 1875°C to 2150°C. The heating rate is selected as 20 K/min from room temperature to 1500°C and then 10 K/min to the sintering temperature. Selection of the sintering temperature depends on the additive system, with the main objective to get fully dense samples after sintering. The first stage of sintering is carried out under a slight N_2 or Ar overpressure of 0.2 MPa for 30 min, followed by a pressure sintering cycle of 30 min at the same

temperature under 10 MPa N_2 or Ar to achieve complete densification. A schematic diagram of the sintering cycle is shown in *Figure 3.3.*
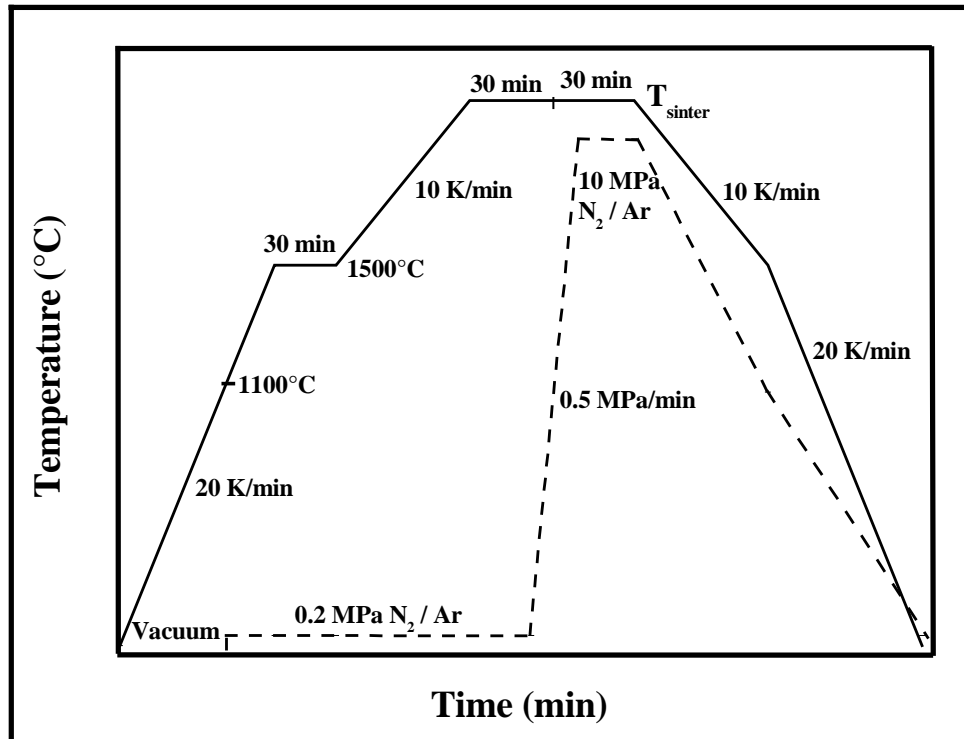
Figure 3.3: Schematic diagram of sintering schedule.

3.1.4 Annealing treatment

Annealing schedules are performed in the same graphite furnaces as the sintering cycles, at a slight overpressure of 0.2 MPa N_2. The specimens are kept in a graphite crucible and annealed at 1950°C for different times to observe the $\beta \rightarrow \alpha$-SiC phase transformation. The heating and cooling rates are kept at 10 K/min.

3.2 Characterisation of the ceramics

3.2.1 Sintered density and mass loss

The sintered densities are measured using Archimedes' water displacement method :

$$\rho_s = \frac{m_s \cdot \rho_w}{m_s - m_w} \qquad\qquad (3.1)$$

where ρ_s = sintered density (g/cm^3), ρ_w = density of water at room temperature (~1 g/cm^3), m_s = mass of the sintered body (g) and m_w = mass of the sintered body in water (g).

The relative densities (ρ_{rel}) are calculated by dividing the sintered density (ρ_s) by the theoretical density (ρ_{th}). The theoretical densities are calculated from the rule of mixtures, and in order to incorporate the effect of phase transformations, another set of theoretical densities is determined by Helium pycnometry.

Mass losses (Δm) of the specimens are measured by using the following formula:

$$\Delta m = \frac{m_G - m_S}{m_G} \cdot 100 \qquad\qquad (3.2)$$

where m_G = mass of the green body (g).

3.2.2 X-ray diffractometry

X-ray powder diffractometry (XRD) is performed in a Siemens D5000 X-ray diffractometer using filtered CuK$_\alpha$ radiation with a wavelength of λ = 1.5406Å on sintered and annealed samples. Qualitative phase analysis [125] is accomplished by comparison with JCPDS standards [126]. The sintered and annealed bodies are ground to fine powders to eliminate texture effects. Bulk oxidised and crept specimens are analysed to evaluate possible texturing and to identify the crystalline phases that evolve during oxidation and creep tests. The X-ray diffraction patterns are analysed by using Siemens DIFFRAC-AT software for identifying the phases present and for measuring the extent of $\beta \rightarrow \alpha$-SiC conversion. The percentage of α-SiC formed upon annealing is calculated from the ratio of the relative intensities of the (101) reflection of the α-SiC polytype 6H (F) and the SiC reflection with maximum intensity (F_{max}), followed by comparison of that ratio with a calibration curve (*Figure 3.4*) established by Nader [50].
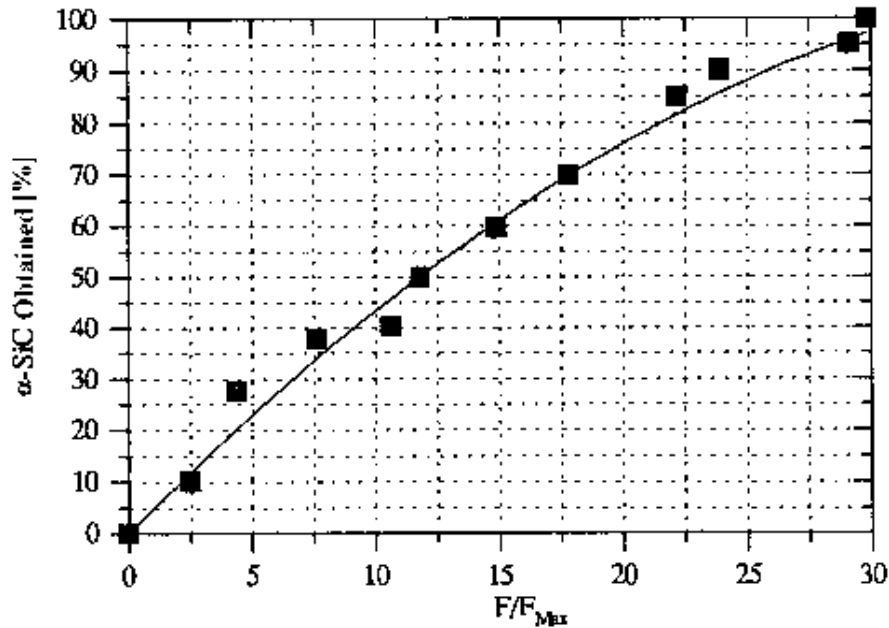
Figure 3.4: Percentage α-SiC vs. intensity ratio [50].

3.2.3 Metallography

For scanning electron microscopy observations, the specimens are Cu-resin mounted (Wirtz Resin II) and polished with a semi-automatic polishing machine (Struers Pedemax II). At first, the mounted samples are ground with a diamond wheel (60 µm) to flatten the surface. Polishing is done using the diamond suspensions DP-PLAN of size 15 µm and DP-DAC of sizes 6, 3 and 1 µm. After polishing, the specimens are dismounted and plasma etched using a RF Plasma Barrel Etcher (Biorad PT7150) for 3-3.5 min in a mixture of CF_4 and O_2 at 1:1 ratio.

3.2.4 Scanning electron microscopy and X-ray microanalysis

Microstructures of the sintered, annealed, crept and oxidised specimens are examined with scanning electron microscopes (SEM) of types S200, Cambridge Instruments, and DSM 982 GEMINI, Zeiss, the latter equipped with a thermal Schottky field emission cathode. The characteristic X-rays emitted due to electron bombardment are analysed by energy dispersive spectrometry (EDS) in order to obtain qualitative and quantitative compositional information from a region of about 1 µm diameter (however, EDS is not an effective tool for light element analysis ($Z < 10$), limiting exact compositional determination). The specimens for SEM observation and EDS analysis are mirror polished to 1 µm. Instead of plasma etching, carbon coating is performed on the

specimens in order to obtain precise compositional measurements and to avoid charging effects.

3.2.5 Transmission electron microscopy

Energy filtered transmision electron microscopy (EFTEM) is carried out using an instrument with maximum accelerating voltage of 120 keV (Zeiss EM 912 Omega). The point resolution of this instrument is 3.8 Å. For the TEM observation, specimens are cut from the bulk materials to obtain thin slices (<1 mm). With the help of a hollow ultrasonic drill (Gatan Model 601), a 3 mm $\varnothing \times 1$ mm disk is obtained. The disk is then glued to the centre of a Gatan disk grinder and ground and polished to a 100 µm thin foil with a surface finish of ¼ µm. Dimpling of this thin foil is done in a dimpling apparatus (Gatan Model 656) to get a thinner core of about 20-30 µm thickness. The thin disk is then dismounted and further glued to a copper ring of 3 mm diameter for mechanical support. Ion-beam milling is performed in a precision ion polishing system (PIPS, Gatan Model 691) at an accelerating voltage of 4-6 keV with the Ar ion beam aligned at an angle of 7-10° to the surface of the specimen for several hours. When a hole is observed at the centre of the specimen, a 2 keV beam is used to remove the amorphous layer. Finally, a TEM specimen is obtained with an electron transparent edge of 10 to 100 nm thickness.

3.3 Mechanical properties evaluation

Room temperature indentation hardness, fracture toughness of sintered and annealed samples, and 4-point bending strength of sintered and annealed specimens at room temperature and at high temperature (1200°C, 1400°C and 1500°C) are measured as representative mechanical properties. Creep tests are extensively performed in order to evaluate the mechanical stability at high temperatures. High temperature compliance tests are also an useful tool to establish high temperature performance.

3.3.1 Room temperature fracture toughness

The fracture toughness of sintered and annealed samples is determined by using the Vickers indentation method. The samples are polished to a surface finish of l µm and

mounted in a specimen holder. For each specimen, 12 indentations are made by a Vickers hardness tester (Buehler Micromet 1) with a load of 5 kg at a constant loading speed of 70 µm/s and a loading time of 15 s. After measuring the crack length and diagonals of the indentation, a software calculates the fracture toughness value using the following formula [112] :

$$K_{Ic} = 0.016 \cdot \sqrt{\frac{E}{H}} \cdot F \cdot L^{-\frac{3}{2}} \qquad (3.3)$$

where E = Young's modulus, taken as 400 GPa for SiC ceramics, H = Vickers hardness (GPa), F = Load (N), L = Crack length (µm).

The hardness (H) is calculated by the formula [108] :

$$H = 1.8544 \cdot \frac{F}{d_H^2} \qquad (3.4)$$

where d_H = diagonals of Vickers indentation (µm).

3.3.2 Bending strength

Four-point bending strength measurements of as sintered and annealed specimens are performed at room temperature and at high temperatures between 1200°C to 1500°C in air. For strength measurements, bar-shaped samples ($3 \times 4 \times 50$ mm^3) are used. The tensile surface of the test specimens is polished to 3 µm diamond finish and the tensile edges are beveled to avoid stress concentrations and large edge flaws caused by sectioning. The distances between the inner and outer load application points are $l_i = 20$ mm and $l_o = 40$ mm, respectively.

Room temperature testing is carried out with a testing machine (Schenck Hydropuls PSA 2017) with a cross head speed of 5 mm/s. For each composition, at least 6 specimens of the dimension 3 mm $\times$ 4 mm $\times$ 50 mm (see *Figure 3.5*) are tested. Special care is taken during specimen preparation in order to avoid any occurrence of surface flaws.
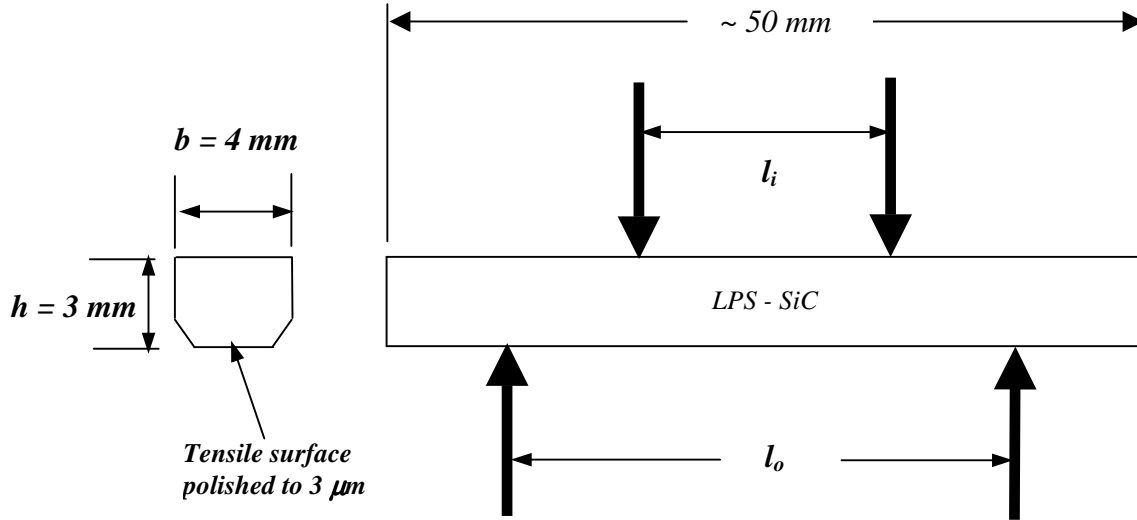
Figure 3.5: *Schematic drawing of 4-point bending strength specimen.*

High temperature tests are performed at 1200°C, 1400°C and 1500°C with a Zwick 1476 universal test machine coupled with an ATS furnace. The specimens are heated up at a rate of 10 K/min to 50°C below the testing temperature and then at a rate of 5 K/min up to the test temperature. This heating profile is followed in order to avoid thermal shock. A dwell time of 10 min is allowed to ensure a homogeneous temperature during testing. The specimens are loaded with a constant cross head displacement rate of 0.1 mm/s.

The bending strength is calculated according to the following formula [108] :

$$\sigma_{4p} = \frac{3}{2} \cdot \frac{F \ (l_o - l_i)}{b \ h^2} \qquad\qquad (3.5)$$

where σ_{4p} = 4-point bending strength (MPa), F = force (N), l_o = length between the two outer supports (40mm), l_i = length between the two inner supports (20mm), b = breadth of the specimen (mm) and h = height of the specimen (mm).

3.3.3 Creep

Various materials are chosen for measuring their creep resistance by using four-point bend testing. The test is conducted with as-sintered and annealed specimens in air, at temperatures ranging from 1200 to 1500°C. The bar specimens used for creep testing are identical to those used for bending strength measurements. The stress (σ_{4p}) is calculated assuming elastic response to the imposed bending moment (given by equation (3.5)). The strain (ε_{4p}) is calculated using the actual specimen displacement Δf relative to the inner load application points and can be expressed as :

$$\varepsilon_{4p} = 4 \cdot \frac{h \cdot \Delta f}{l_i^2} \qquad (3.6)$$

Specimen displacement is measured by using a three-rod system connected to a position encoder outside the hot zone to provide the differential measure Δf [127]. Four-point bending creep rate measurements are performed at temperatures of 1200, 1300, 1400, and 1500°C with different applied stress levels varying from 50 MPa to 300 MPa for a maximum duration of 60 h. The specimens are heated at a rate of 10 K/min to 50°C below the test temperature, then at 5 K/min to the final test temperature, and held for 45 min for temperature homogenization. The samples are loaded with a constant cross head speed of 0.002 mm/s and the constant stress level is maintained within the range of ± 1 MPa.

3.3.4 High temperature compliance testing

The samples as well as the experimental setup used for this experiment are similar to those used for the measurement of high temperature 4-point bend strength. The specimens are heated to temperatures between 850°C and 1450°C at intervals of 150°C. The heating rate up to 1300°C is 10 K/min, followed by 5 K/min to the peak temperature of 1450°C. Transient loading to 100 MPa with a cross head speed of 0.1 mm/s is used at each of the temperature stops of 850, 1000, 1150, 1300 and 1450°C. Prior to loading, a holding time of 10 min is allowed for temperature homogenization.

3.4 Oxidation

Oxidation experiments are carried out at different temperatures varying from 1200°C to 1500°C over a period of 100 h in air. Rectangular pellets (2 mm × 10 mm × 17 mm) are cut from the bulk specimen with a diamond saw, ground and carefully mirror polished to 3 µm with diamond paste. Prior to oxidation, the specimens are cleaned in an ultrasonic bath and degreased with acetone and alcohol. Dried pellets are then weighed accurately and the exact dimensions are measured for calculating the surface area. The experiments are carried out in a horizontal tube furnace preheated to the oxidation temperatures. Inside the furnace, the samples are placed on a HIPed SiC block to avoid reaction with the sample holder. The weight gain as a function of time is recorded by intermittently removing the specimens from the furnace after 1 to 36 h intervals for weighing and then putting them back. The samples are slowly inserted and taken out in order to maintain heating and cooling rates of ≤ 50 K/min for avoiding thermal cracking.

4 Sintering kinetics and microstructural design

This chapter describes the selection process of rare-earth sesquioxides as sintering additives for SiC. Basic sintering and dilatometric studies are performed in order to understand the densification behaviour and the sintering kinetics with varying temperatures, sintering atmospheres and compositions. Phase evolution is monitored as a function of compositional variation and annealing treatments. XRD/EDS/AES analysis and SEM/TEM investigations help to explain the structure-property relationships.

4.1 Dilatometry

In order to optimise the rare-earth sesquioxide systems, a series of dilatometric tests are performed. Based on the cationic radus difference, various pairs of rare-earth sesquioxides are added to SiC as sintering additives. *Table 4.1* shows the series of samples along with the ionic radii of the rare-earths and the calculated tolerance factor (see chapter 2) for different coordination numbers (CN).

Table 4.1: Calculated tolerance factor on the basis of cationic radius difference for coordination numbers 6 and 8 [92].

| Rare-earth cation	Cationic radius, $r_{RE^{3+}}$ (pm)		Series (50:50 mol%)	Tolerance factor, t	
	CN-6	CN-8		CN-6	CN-8
Gd^{3+}	93.8	106.0	1Gd-1Ho	0.7207	0.7583
			1Gd-1Er	0.7248	0.7626
			1Gd-1Lu	0.7354	0.7738
Dy^{3+}	90.8	103.0	1Dy-Ho	0.7114	0.7490
			1Dy-1Lu	0.7260	0.7644
Ho^{3+}	89.4	102.0	1Ho-1Dy	0.7114	0.7414
			1Ho-1Gd	0.7207	0.7319
			1Ho-1Lu	0.7216	0.7612
Y^{3+}	89.2	101.5	1Y-1Lu	0.7209	0.7596
Er^{3+}	88.1	100.0	1Er-1Gd	0.7248	0.7259
Lu^{3+}	84.8	97.0	1Lu-1Y	0.7209	0.7312
			1Lu-1Ho	0.7216	0.7305
			1Lu-1Dy	0.7260	0.7261
			1Lu-1Gd	0.7354	0.7168
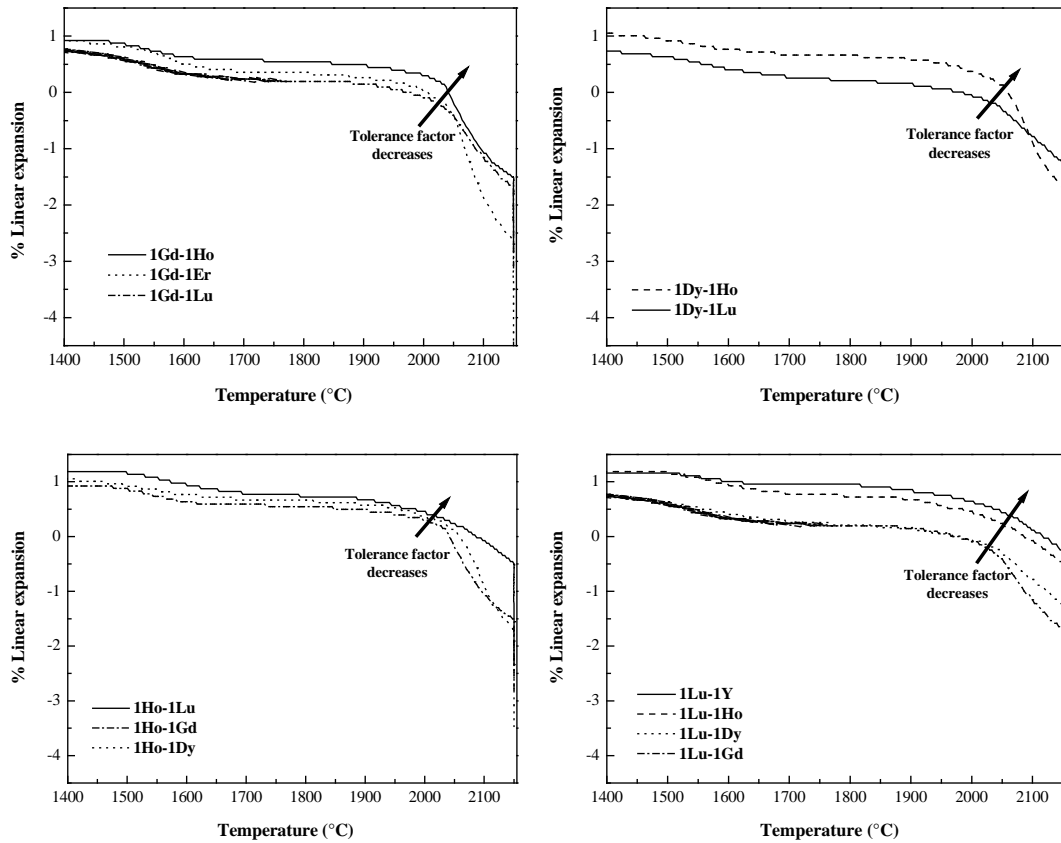
Figure 4.1: Dilatometric curves for different additive systems showing the shrinkage and densification rate at different temperatures.

From *Figure 4.1*, it is observed that as the cationic radii difference or the tolerance factor increases, the sintering temperature decreases for all the series except for holmium where till 2090°C, the dilatometric behaviour is in accordance with the expected results but after that the trend gets reversed. If a higher coordination number, i.e., 8 is assumed for Ho at higher temperature, then the behaviour is similar to the expected one. A similar observation was also made in the studies of Menke *et al.* [8] and Murakami *et al.* [128]. They observed a linearly increasing trend of T_g with CN upto Gd and then a decreasing trend for higher atomic number rare-earth oxides. It is found that in some complex oxides, trivalent rare-earth ions take higher coordination states as compared to other trivalent cations [93]. This has been attributed to the strong ionicity of the RE–O bond and an ionic size large enough to accommodate 8 or more nearest neighbours. So, depending on the ionicity and size, rare-earth elements can assume different CN. In other words, the variation of properties with either ionic size or tolerance factor is not a linear one.

4.1.1 Characterisation of dilatometric specimens

The densities of the dilatometric samples are measured by the well known Archimedes'
principle and are reported in *Table 4.2* along with the mass loss data.

*Table 4.2: Dilatometric results for different combinations of rare-earth sequioxides as
sintering additives for SiC with varying atmosphere and temperature.*

Composition (50:50 mol%)	% Mass loss	Density (g/cm^3)	% Theoretical density	Temperature (°C)	Atmosphere (0.2 MPa)
1Gd-1Er	10	2.98	81	2070	Ar
1Gd-1Er	6.4	3.52	96	2150	N_2
1Sc	18	1.69	52	2120	Ar
1Sc	8.9	1.72	53	2150	N_2
1Lu	5.1	2.49	65	2150	N_2
1Gd-1Ho	6.3	3.72	102	2150	N_2
1Gd-1Lu	7.6	3.68	99	2150	N_2
1Dy-1Lu	8.4	3.06	82	2150	N_2
1Dy-1Ho	5.0	3.08	83	2150	N_2
1Ho-1Lu	4.8	3.40	91	2150	N_2
1Lu-1Y	6.3	3.58	99	2150	N_2
1Lu-1AlN	7.0	3.59	98	2150	N_2

From the tabulated values, it is observed that the degree of densification with only
Sc_2O_3 or Lu_2O_3 oxide is poor. Insufficient liquid phase as well as high mass losses (in
case of Sc_2O_3) may be the cause for less densified materials even after sintering at
2150°C. Specimens with binary rare-earth systems containing Lu_2O_3 as one of the
sintering additives sintered well and more than 90% of the theoretical density has been
achieved in all the cases. However, the material with Lu_2O_3-Dy_2O_3 shows a relatively
low density due to high mass loss in this system. Similar results are also found in the
system with Gd_2O_3-Er_2O_3 when sintered under Ar atmosphere. So, following the
experimental results of *Table 4.2*, some combinations of two rare-earth oxides are
selected for further sintering studies.

4.2 $RE_2^I O_3$ - $RE_2^{II} O_3$ additive systems

4.2.1 Sintering behaviour

The average sintered densities and mass losses of all the materials are reported in *Table 4.3*. The mass loss for the 1Gd-1Er system is rather high due to relatively high vapour pressure of the gadolinium oxide at the sintering temperature. Sintered densities of LPS-SiC samples with the additive systems 1Dy-1Lu, 1Gd-1Ho and 1Dy-1Ho are not consistent with the sintering temperature and sometimes only ≤80% of the theoretical density are reached when sintered in Ar atmosphere. Irregular behaviour during sintering can be due to the fact that the furnace atmosphere can sometimes be very different depending on previous sintering runs. Furthermore, the temperature calibration of different furnaces can deviate according to the method of measurement. Relative densities ≥99% are consistently achieved with the 1Gd-1Ho and 1Dy-1Ho systems after sintering at 2000°C in N_2 atmosphere. *Figure 4.2(a)* shows the effect of sintering temperature on the final densities of 1Gd-1Ho and 1Dy-1Ho under different sintering atmospheres.
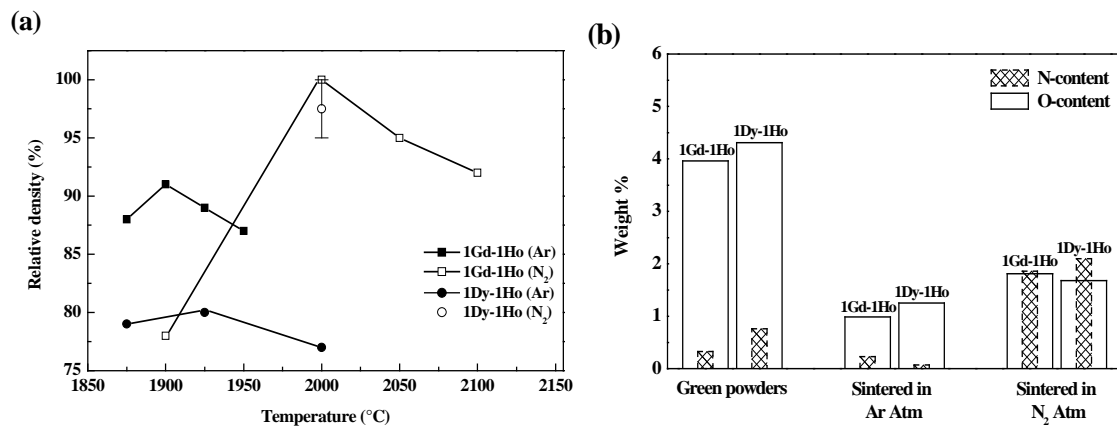
Figure 4.2: (a) Relative density vs. sintering temperature, (b) nitrogen and oxygen content in the samples.

In contrast to N_2, Ar atmosphere obstructs densification. Most probably, N_2 entrapped in pores is able to dissolve into the liquid phase, thereby enhancing the pore closure in the final densification stage. Chemical analysis (*Figure 4.2(b)*) reveals that the 1Gd-1Ho and 1Dy-1Ho samples have a higher N content when sintered in N_2 over-pressure. Nitridation of rare-earth oxides can lead to increase in N content and some mass gain is observed in the system 1Gd-1Ho when sintered in 10 MPa N_2 overpressure (*Table 4.3*).

Apart from facilitating densification, N_2 atmosphere also retains a higher O level as compared to Ar atmosphere, owing to the fact that N_2 increases the viscosity of the melt which hinders the loss of oxygen by evaporation due to lower diffusivity of the chemical species.

Table 4.3: The average sintered densities and mass losses of all the materials sintered in different atmosphere and at different temperatures.

Composition (50:50 mol%)	% Mass loss	Density (g/cm^3)	% Theoretical density	Temperature (°C)	Atmosphere (0.2 MPa)
1Gd-1Er	4.5	2.76	75	1900	Ar
,,	4.6	2.78	76	1925	,,
1Dy-1Lu	3.2	3.45	91	1900	,,
,,	3.2	3.51	94	1925	,,
,,	1.6	3.10	80	1925	,,
1Gd-1Ho	2.6	3.24	88	1875	,,
,,	3.8	3.48	95	1900	,,
,,	2.6	3.33	91	1900	,,
,,	2.5	3.25	89	1925	,,
,,	3.9	2.71	74	1925	,,
,,	2.8	3.20	87	1950	,,
,,	3.5	3.47	95	2000	10 MPa Ar
,,	2.4	2.86	78	1900	N_2
,,	3.3	3.70	101	2000	,,
,,	3.3	3.70	101	2000	,,
,,	-0.5	3.21	87	2000	10 MPa N_2
,,	-0.4	3.19	87	2000	,,
,,	-0.5	3.20	87	2000	,,
,,	-0.3	3.20	87	2000	,,
,,	-0.2	3.20	87	2000	,,
,,	-0.3	3.21	87	2000	,,
,,	-0.3	3.20	87	2000	,,
1Dy-1Ho	1.8	2.91	79	1875	Ar
,,	3.0	2.86	77	1925	,,
,,	3.2	3.55	96	1925	,,
,,	2.0	2.96	80	1925	,,
,,	4.0	2.86	77	2000	,,
,,	3.3	3.35	91	2000	10 MPa Ar
,,	3.1	3.10	84	2000	N_2
,,	3.4	3.55	95	2000	,,
,,	3.3	3.68	99	2000	,,

The sintering mechanism in 1Gd-1Ho as well as in the 1Dy-1Ho system is not clear from the microstructural observation (*Figure 4.3*). Even after severe plasma etching, there is no visible core-rim structure of the SiC grains which would indicate a solution-repreciptation mechanism [94]. However, EDS analysis shows (*Figure 4.4*) traces of dysprosium, holmium and oxygen inside the SiC grains which suggest that sintering occurred through a solution-repreciptation mechanism [94]. During sintering, the mass transport mainly occurs through the liquid phase formed by the dissolution of the two rare-earth oxides along with some amount of SiO_2 present on the surface of the SiC grains. As sintering progresses, SiC-grains with highly convex curvature (small grains) will begin to dissolve in the oxide melt to the solubility limit. Initial α-SiC seeds or larger grains act as nucleation sites for α-SiC precipitation. Thus, solution-repreciptation occurs on the pre-existing α-SiC and is connected with some chemical inhomogenity of the SiC-grains.
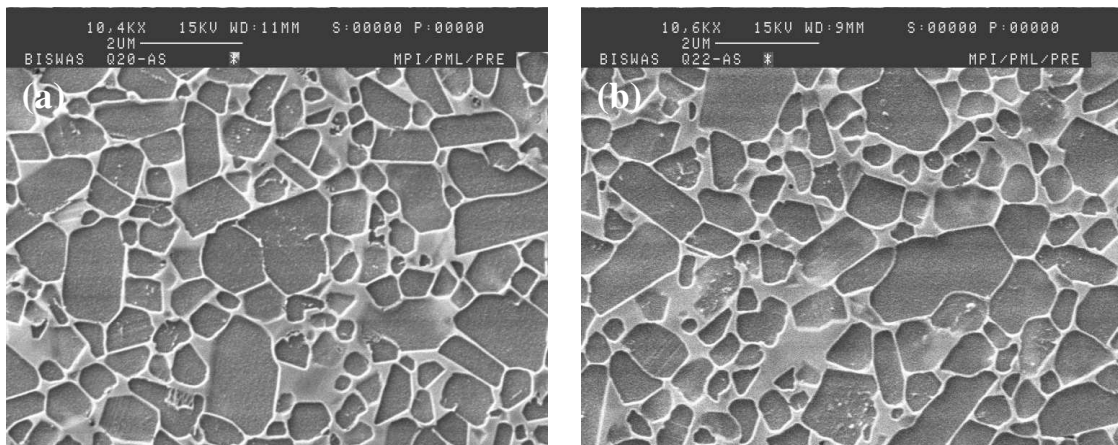

Figure 4.3: Microstructure of as-sintered SiC materials sintered in N_2: (a) 1Gd-1Ho and (b) 1Dy-1Ho.

During sintering, complete wettability of the SiC-grains and a homogeneous microstructure are obtained in both systems (*Figure 4.3*). However, EDS analysis of TEM specimens shows some segregation of rare-earth elements depending on their cationic radius. In the 1Dy-1Ho system, the element with higher cationic radius (Dy^{3+}) more likely to get deposited at grain boundary layers whereas the content of the element with lower atomic radius (Ho^{3+}) is higher at multi grain junctions (*Figure 4.4*). A similar wettability behaviour of SiAlON grains sintered with rare-earth oxides and a

segregation effect depending on atomic radius was observed by Rosenflanz and Chen [6].
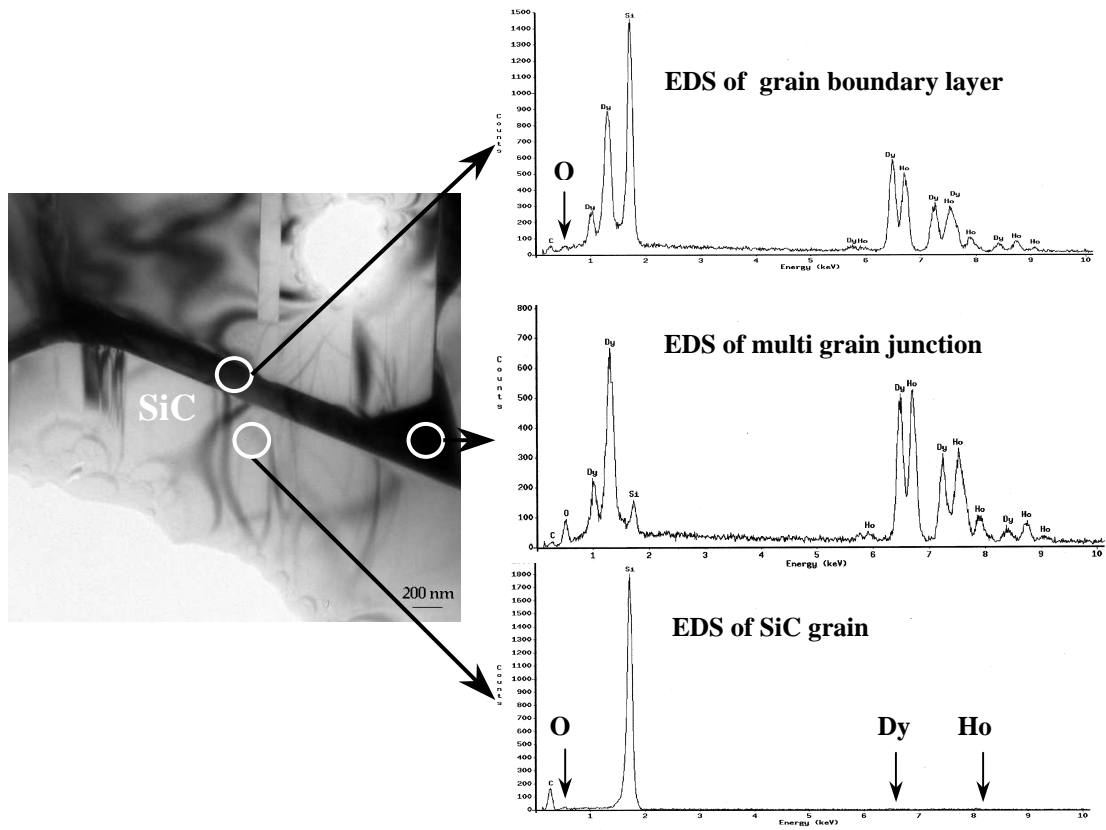

Figure 4.4: TEM-EDS analysis of SiC sintered with 1Dy-1Ho showing different spectra obtained from the SiC grain and the grain boundary layer and multi grain junction.

4.2.2 Microstructure and phase evolution

Typical microstructures of LPS-SiC sintered with 1Gd-1Ho and 1Dy-1Ho are shown in *Figure 4.3*. The remnant of the liquid phase is primarily located at the triple or multi-grain junctions. Plasma etching reveals a grain-boundary film present between the SiC grains in both the systems. In order to confirm this, TEM investigation is done on these systems. *Figure 4.5* represents a low magnification transmission electron micrograph showing the general morphology of the 1Dy-1Ho system with the SiC grains being in bright contrast and showing some bending contours and stacking faults. The secondary phases appear in dark contrast because of the presence of the heavy rare-earth elements resulting in high electron scattering. The TEM image, along with electron diffraction patterns (*Figure 4.5*), confirms the presence of an amorphous layer along the SiC grain-boundaries as well as at heterophase boundaries (between SiC grains and crystalline

secondary phase). The electron diffraction pattern from the grain boundary layer (*Figure 4.5 (1)*) shows spots in addition to an annular ring, suggesting that some crystalline phases are present as well.
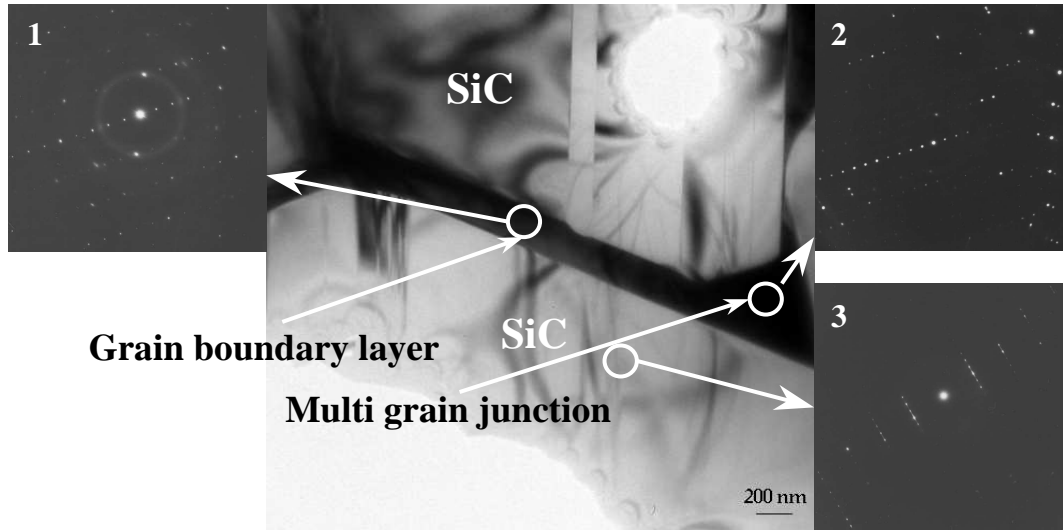

Figure 4.5: Transmission electron micrograph along with electron diffraction patterns showing amorphous and crystalline regions in LPS-SiC sintered with the 1Dy-1Ho additive system.
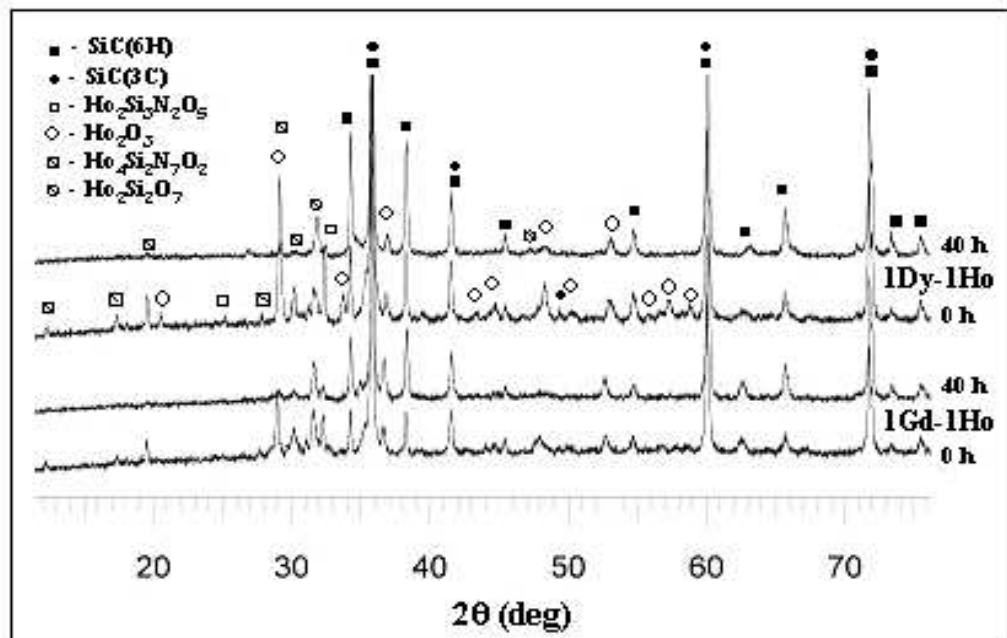

Figure 4.6: X-ray diffraction pattern of LPS-SiC sintered with 1Gd-1Ho and 1Dy-1Ho after sintering and annealing for 40 h.

This is different from the observations by Ye [129] on LPS-SiC sintered with AlN-Y_2O_3 additives, where the intergranular films (thickness ~ 1 nm) were always amorphous. Multi grain junction phases are entirely crystalline after sintering as can be seen from diffraction patterns of triple points (*Figure 4.5 (2)*). According to the XRD pattern of the as sintered samples (indicated by "0 h") in *Figure 4.6*, the major grain boundary layer phases are crystalline in both the 1Gd-1Ho and 1Dy-1Ho systems showing sharp reflections in the XRD pattern, with little diffuse scattering indicating that the amount of residual amorphous phases is small.

Annealing of SiC materials sintered with these systems also gives rise to a platelike morphology of the SiC grains (*Figure 4.7*) very similar to LPS-SiC sintered with conventional additive systems [55,76,81]. The microstructure changes from equiaxed to platelike grains during annealing, and grain growth proceeds predominantly perpendicular to the prismatic planes of the hexagonal crystal lattice (plate-like growth). This anisotropic grain growth of α-SiC grains is related to the β → α-phase transformation and continues until full transformation is achieved or until there is steric hindrance by neighbouring grains [55,67]. This microstructural development is analogous to the formation of rodlike grains in Si_3N_4-ceramics [47,67,68]. Image analysis of the two dimensional sections provides a estimation of the average grain size (measuring the sectional length of the grains), aspect ratio and the secondary phase content in the two systems, and results are tabulated below (*Table 4.4*).

Table 4.4: The average grain size, aspect ratio and the liquid-phase content in sintered and annealed materials after sintering with 1Gd-1Ho and 1Dy-1Ho additive systems.

Powder denomination	Average grain size (µm) after		Average aspect ratio after		Secondary phase content (%) after	
	sintering	40 h of annealing	sintering	40 h of annealing	sintering	40 h of annealing
1Gd-1Ho	1.0 ± 0.6	1.3 ± 0.7	1.2 ± 0.2	1.6 ± 0.6	11 ± 0.5	2.7 ± 0.3
1Dy-1Ho	1.1 ± 0.5	1.7 ± 0.5	1.3 ± 0.3	2.2 ± 0.5	11 ± 0.4	2.2 ± 0.3

It is observed that the average grain size increases with annealing along with the aspect ratio, the platelet type of morphology evolving in both systems. However, due to faster

kinetics in the system 1Dy-1Ho, the growth of platelet grains is more pronounced. In both cases, secondary phases are expelled from the grain boundary region upon annealing, and very small amounts of residual secondary phases remain at the triple or multi-grain junctions. The reduction of residual secondary phases occurs due to the volatilisation of these phases via carbothermal reductions (graphite-heated furnace) [130]. Remarkably, this does not seem to generate any porosity in the present systems. From the micrographs (*Figure 4.3 and 4.7*) and the phase-transformation plot (*Figure 4.8*), it is clear that the kinetic is faster in case of the smaller cation contrary to what
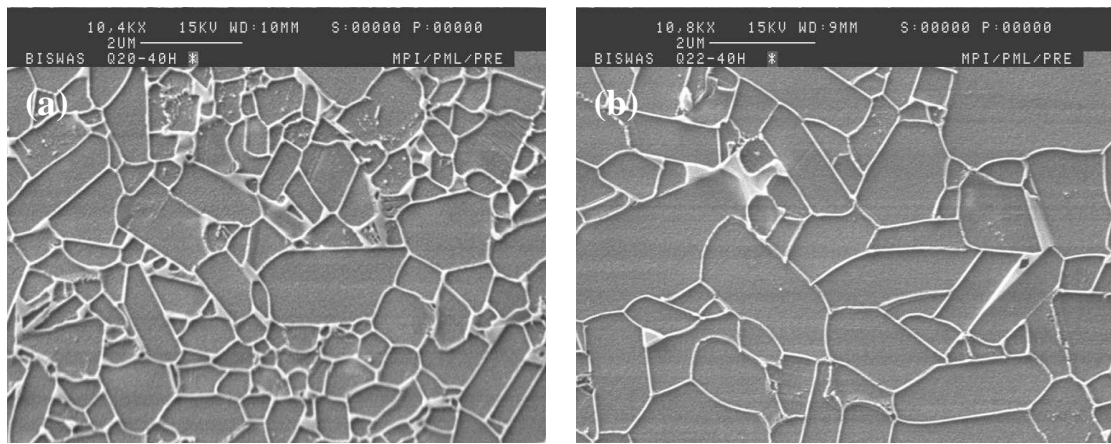

Figure 4.7: Microstructure of annealed SiC materials sintered with (a) 1Gd-1Ho and (b) 1Dy-1Ho (compare to Figure 4.3).
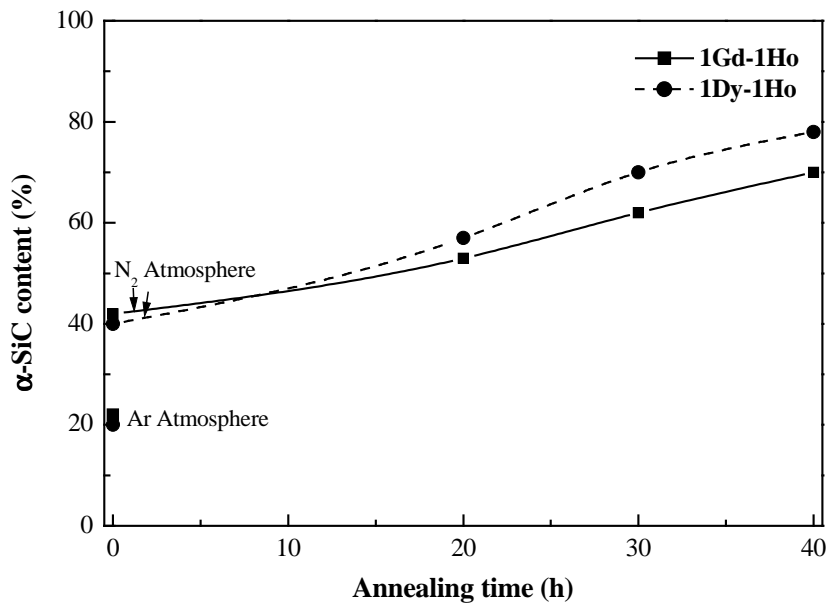

Figure 4.8: $\beta \rightarrow \alpha$-SiC phase transformation as a function of annealing time.

would be expected from chemical considerations [131]. Although silicate liquids containing larger cations (lower field strength) show a lower viscosity, the transformation kinetics do not follow this rule. Rather, the opposite phenomenon is observed here. Since material transport through the melt is obviously not the rate limiting step (otherwise grain growth and transformation would scale with the melt viscosity), the dissolution rate of SiC in the melt is probably rate-determining [132] (or the re-precipitation rate, but this has not yet been reported in the literature on this kind of materials). Possibly, the higher field strength of the Dy^{3+} ions makes the 1Dy-1Ho melt more efficient in dissolving SiC.

4.2.3 Fracture toughness and hardness

Vickers indentation fracture toughness and hardness are measured on as-sintered and annealed samples and plotted in *Figure 4.9*. In as-sintered samples, cracks propagate mainly along the grain boundaries as the grain boundary phases are weakest due to thermal expansion mismatch between grain boundary phases and SiC grains [133]. However, the crack path remains essentially straight as there is no appreciable crack deflection by the fine globular microstructure (*Figure 4.10 (a) and (c)*). The fracture
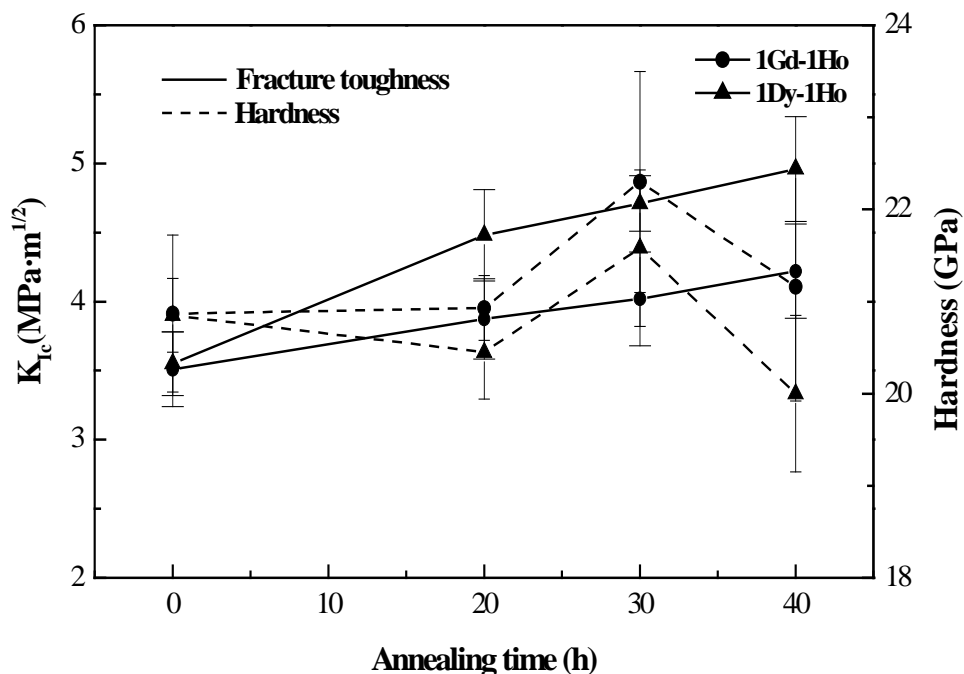

Figure 4.9: Variation of fracture toughness and hardness as a function of annealing time in SiC ceramics sintered with 1Gd-1Ho and 1Dy-1Ho additive systems.

toughness increases with annealing time for both the systems. In the annealed samples, cracks also propagate along the grain boundaries but are continuously deflected by elongated grains (*Figure 4.10 (b) and (d)*). Crack deflection along the grain boundaries seems to be the main toughening mechanism [134]. Apart from crack deflection, crack bridging, mechanical interlocking and thermally induced microcracking may also play a significant role in the toughening of SiC ceramics [75,129]. In the present case, the fracture toughness improves with post sintering annealing treatments, this behaviour being more pronounced in the case of SiC sintered with the 1Dy-1Ho additive system as compared to the 1Gd-1Ho system (*Figure 4.9*). This larger improvement upon annealing can be directly correlated with the larger grain size and higher aspect ratio.

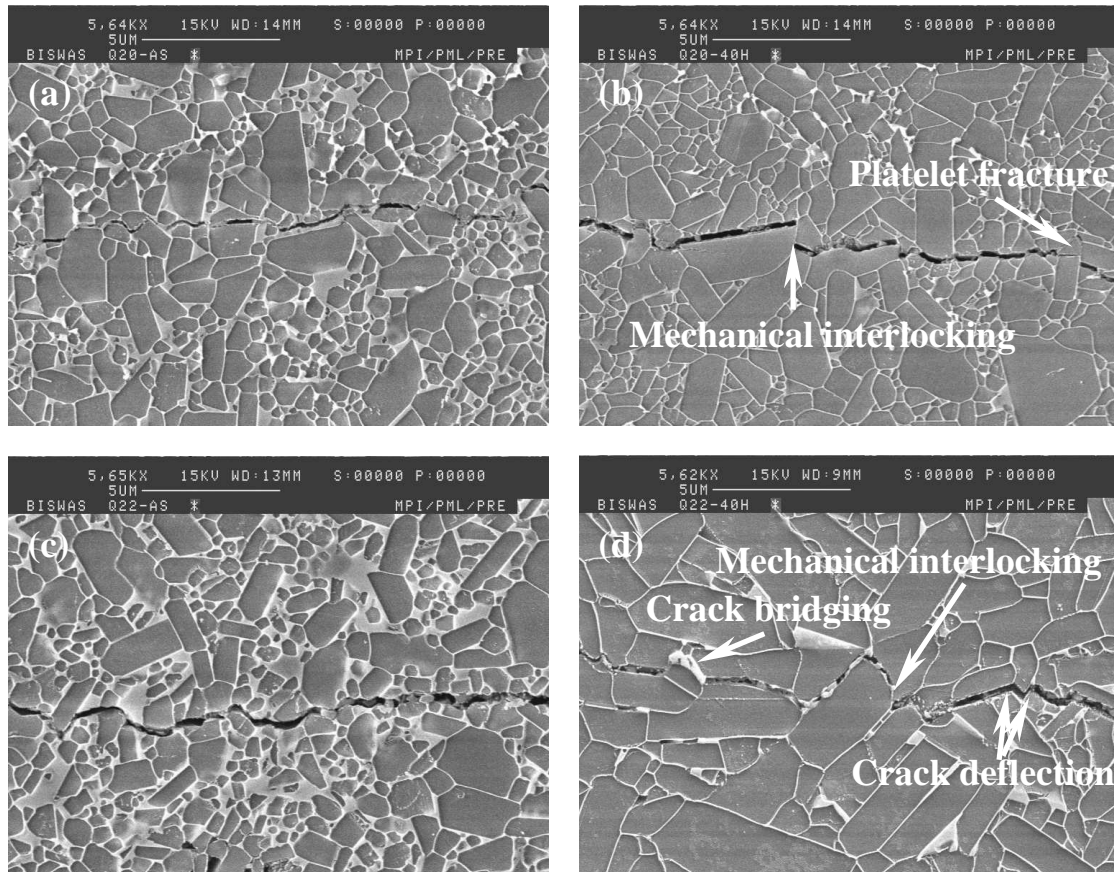*Figure 4.10: Vickers indentation crack propagation in as sintered (a) 1Gd-1Ho and (c) 1Dy-1Ho and in annealed (for 40 h) (b) 1Gd-1Ho and (d) 1Dy-1Ho .*

The Vickers hardness value initially remains unchanged for both systems. Thereafter it increases to a maximum value after 30 h of annealing, followed by a drop at the maximum annealing time of 40 h. During annealing, the average grain size ($\overline{G}$)

increases in both systems and hence invoking Hall-Petch like H vs. $\overline{G}^{-\frac{1}{2}}$ behaviour, one can expect a decrease in hardness (H) values with increasing average grain size [135]. However, in poly-crystalline materials containing glassy grain boundary and intergranular phases, after thermal treatment, reduction and crystallisation of the secondary phases generally improve the hardness of the material [130]. Hence, there seems to be a trade-off between glassy phase removal and grain coarsening effect. However, hardness values drop again. This is thought to be due to the formation of micro-cracking caused by residual stresses generated after considerable grain boundary phase removal [130]. For 1Dy-1Ho, a higher hardness could be expected due to the lower cationic radius and stronger RE–O bond strength, counteracting the microstructural mechanism described above. This is obviously not the case (*Figure 4.9*).

4.3 The Lu$_2$O$_3$-AlN additive system

The objective of the addition of Lu$_2$O$_3$ was to substitute Y$_2$O$_3$ in one of the conventional additive systems for SiC (AlN-Y$_2$O$_3$) and observe the effects on sinterability, microstructure and mechanical properties.

4.3.1 Sintering behaviour

Dilatometric studies on this system (*Table 4.2*) showed 98% densification with a moderate mass loss of 7% which is mainly due to the decomposition of AlN [55,134]. In order to suppress this decomposition of AlN, sintering experiments were carried out by applying a N$_2$ overpressure. To establish which chemical composition provides the best sintering aids, three formulations with different Lu$_2$O$_3$:AlN ratios are investigated. *Table 4.5* shows the sintered densities for these formulations. It is observed that all three intermediate compositions of 1Lu-2AlN, 1Lu-1AlN and 2Lu-1AlN have superior sinterability. More than 99% densification occurs in all the samples with a low mass loss ($< 3\%$) after sintering at 2100°C in a N$_2$ overpressure (10 MPa).

Table 4.5: The average sintered densities and mass losses of SiC sintered with different Lu$_2$O$_3$:AlN ratios.

Powder denomination	% Mass loss	Density (g/cm^3)	% Theoretical density	Temperature (°C)	Atmosphere (10 MPa)
1Lu-2AlN-AS	2.3	3.60	98.9	2100	N$_2$
1Lu-1AlN-AS	2.8	3.69	99.5	2100	N$_2$
2Lu-1AlN-AS	2.6	3.74	99.1	2100	N$_2$

Figure 4.11 shows microstructures of the SiC ceramics sintered with different Lu$_2$O$_3$-AlN compositions. Plasma etched samples reveal a typical core and rim structure inside the SiC grains which indicates that the sintering mechanism in these systems is also solution-reprecipitation [94]. Both the core and rim zones consist predominantly of one single polytype of SiC, namely 6H α-SiC [52]. The difference in contrast comes from the differential etching behaviour of the core with respect to the rim region which contains impurities due to the reprecipitation process. By analysing the rim zone, EDS

analysis reveals traces of Lu and O in the SiC grains (*Figure 4.12*). Low concentrations and the presence of the heavy rare-earth element make it difficult to identify Al by EDS analysis. However, auger electron spectroscopic (AES) analysis on the SiC grains qualitatively proves the existance of Al (*Figure 4.13*). This observation corroborates that the sintering proceeds through solution-reprecipitation processes similar to the $RE_2^I O_3$-$RE_2^{II} O_3$ systems discussed in the previous section.
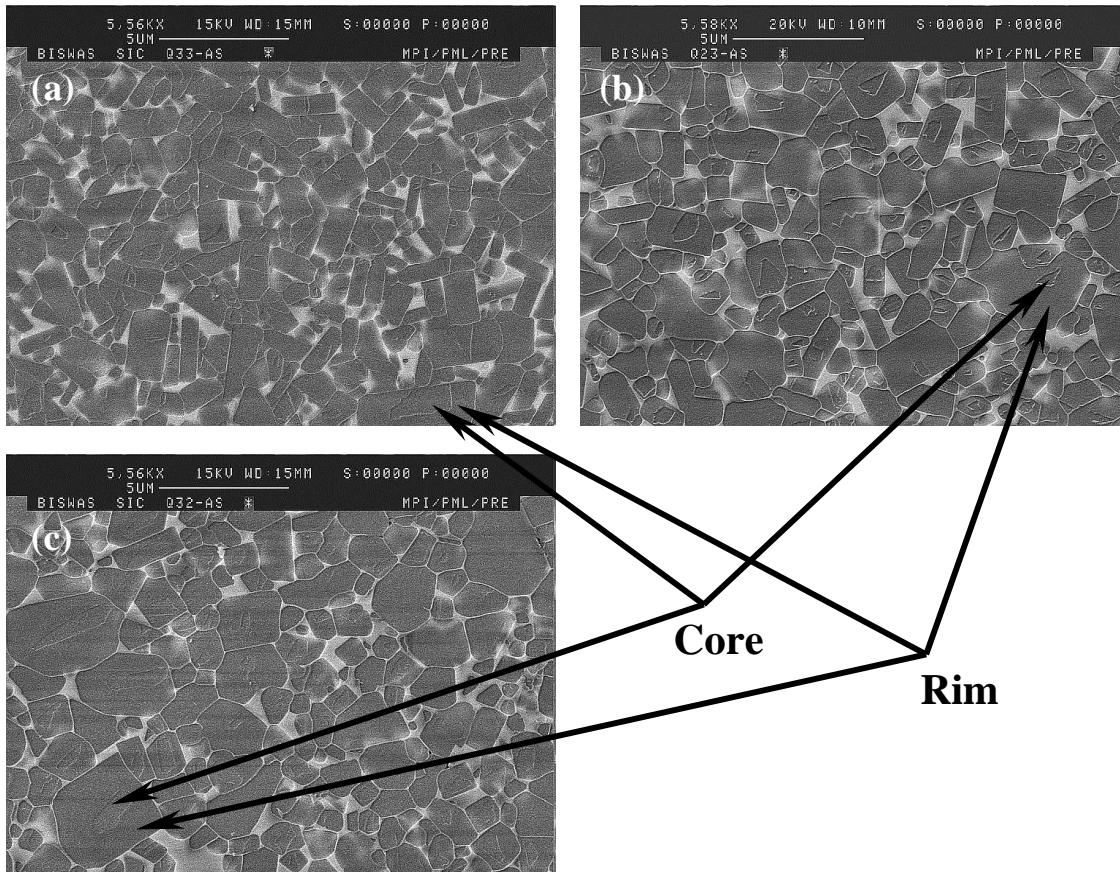

Figure 4.11: Microstructure images showing the core-rim structure in LPS-SiC materials sintered with (a) 1Lu-2AlN, (b) 1Lu-1AlN and (c) 2Lu-1AlN additives.
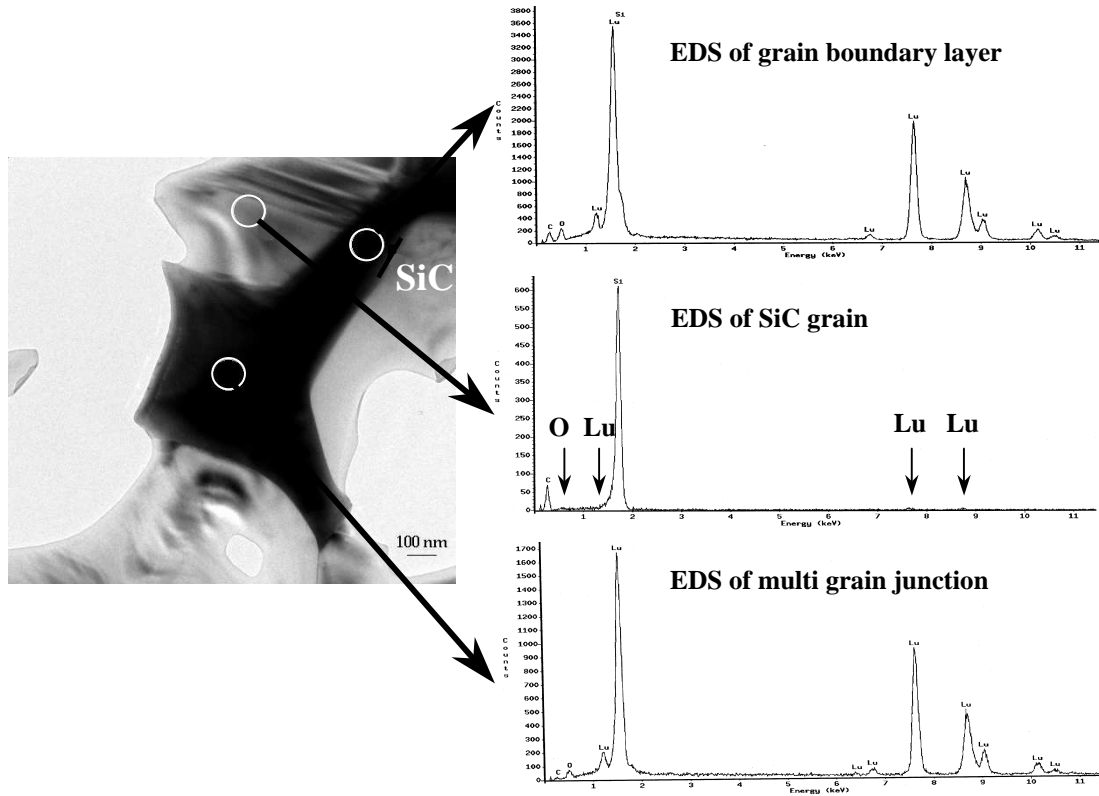
Figure 4.12: TEM-EDS analysis of SiC sintered with 1Lu-1AlN, showing spectra obtained from the SiC grain, the grain boundary layer and multi grain junction.
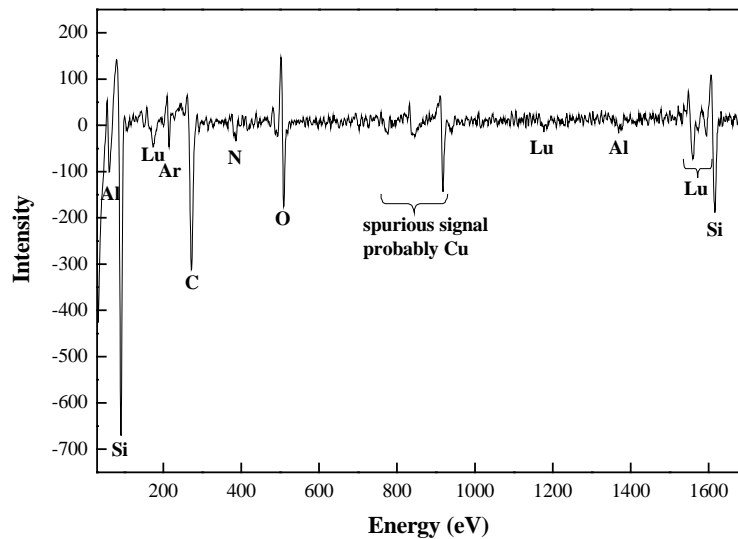

Figure 4.13: Auger electron spectroscopic analysis of a SiC grain after sintering SiC with 1Lu-1AlN additive.

4.3.2 Microstructure and phase evolution

SEM images of LPS-SiC samples sintered with different molar ratio of Lu_2O_3:AlN have been shown in *Figure 4.11*. The microstructures consist of SiC-grains separated by an intergranular secondary phase. The morphology of the grains changes from platelet with some globular grains to mostly globular grains as the Lu_2O_3 content increases in the secondary phase. In SEM micrographs, residual porosities are not observed in these systems. The characterisation of the intergranular phases has been carried out by TEM. In all samples, the grain boundaries are characterised by an amorphous structure with little crystalline phases as observed in the electron diffraction patterns (*Figure 4.14*). However, the triple junction phases are completely crystalline after sintering. Similar types of patterns were also found in the earlier systems. XRD patterns show that sintered samples contain mainly β- and α-SiC along with Lu_2O_3 as major secondary phase (*Figure 4.15*). Traces of $Lu_4Si_2N_7O_2$ and $Lu_2Si_3N_4O_3$ are present as secondary crystalline phases after sintering. Due to the N_2 overpressure, these oxynitride phases may evolve during cooling. However, after annealing treatments, they are decomposed to the disilicate $Lu_2Si_2O_7$. XRD or EDS of the secondary phases give no hint to the presence of Al in these systems after sintering or annealing. However, AES (*Figure 4.16*) and chemical analysis do confirm the presence of Al (~1.25-1.5 wt%) within these samples.
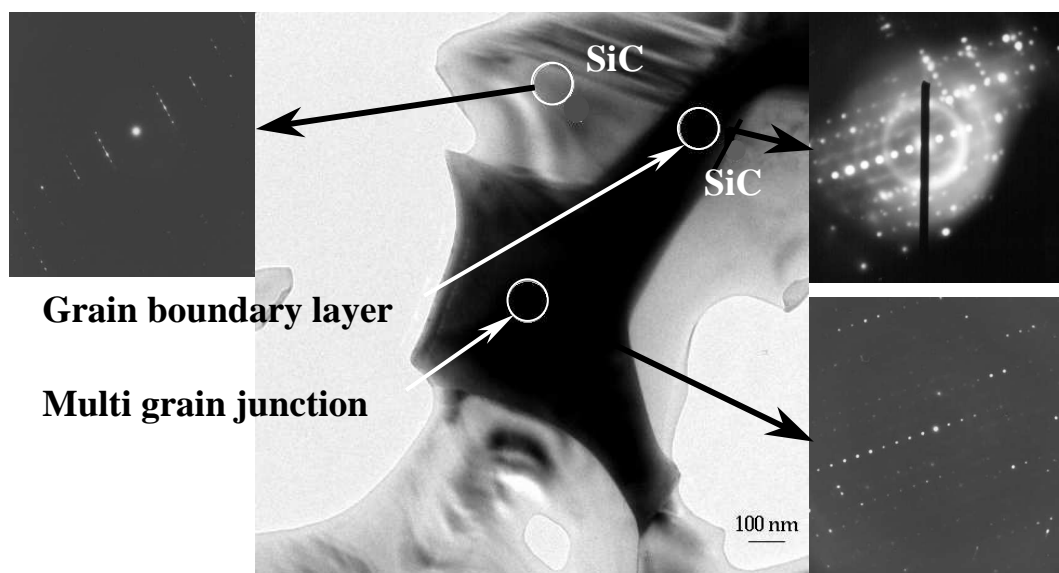

Figure 4.14: Transmission electron micrographs along with electron diffraction showing the amorphous and crystalline regions in SiC sintered with 1Lu-1AlN additive system.
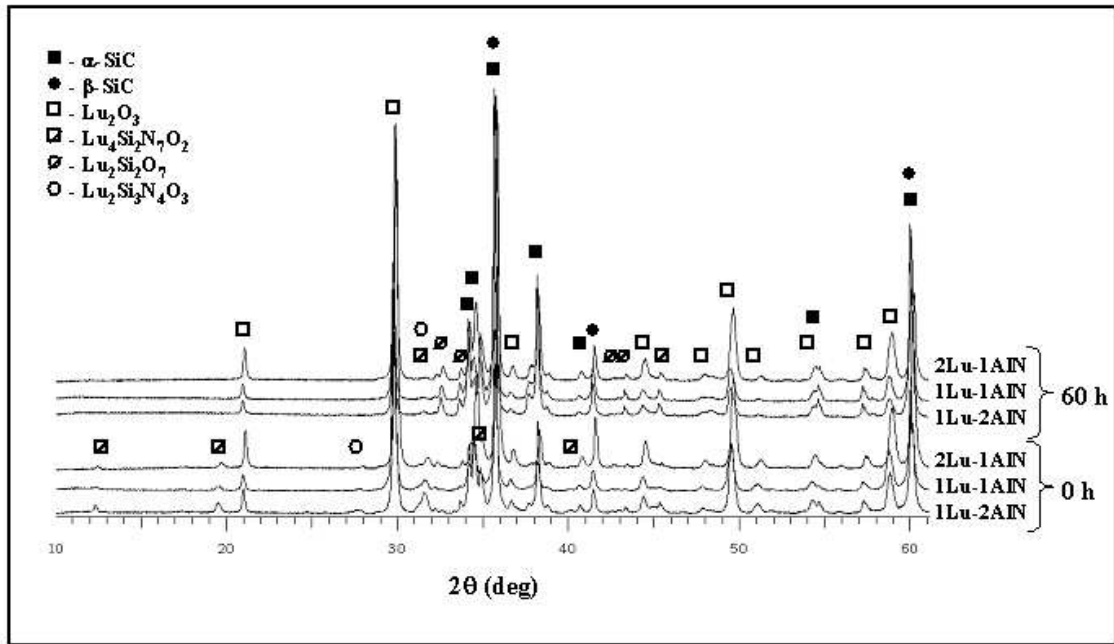
Figure 4.15: X-ray diffraction patterns of LPS-SiC sintered with 1Lu-2AlN, 1Lu-1AlN and 2Lu-1AlN after sintering and annealing for 60 h.
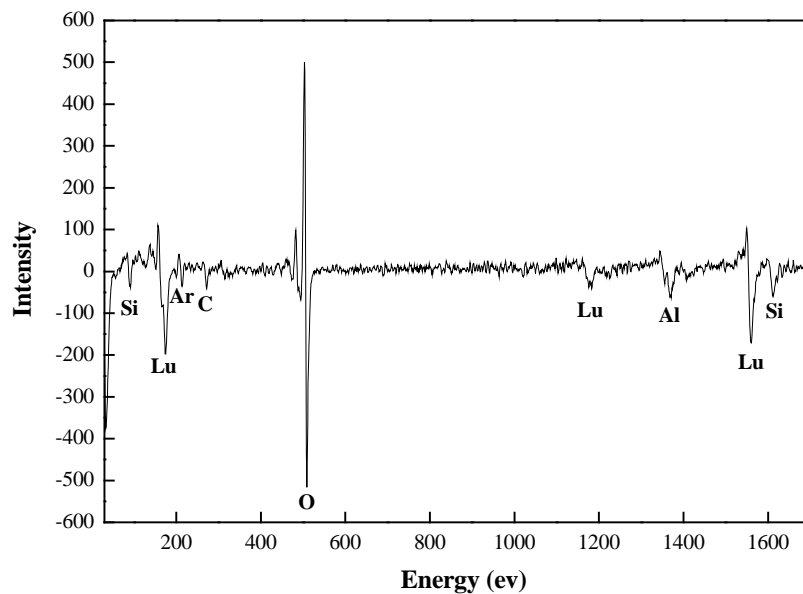
Figure 4.16: Auger electron spectroscopic analysis of intergranular phase obtained after sintering of SiC with 1Lu-1AlN additive.

By comparing the different XRD intensities of the crystalline phases with the main Bragg reflection (α-SiC (006) + β-SiC (111)), it is observed that the extent of crystallisation as well as $\beta \rightarrow \alpha$-SiC transformation decreases with increasing Lu_2O_3

content in the secondary phases (*Figure 4.17*). This phenomenon is attributed to the liquid viscosity since silicate liquids containing more refractory rare-earth oxide (Lu_2O_3) typically show a higher viscosity, which is likely to render the transformation more sluggish due to slow diffusion of the chemical species [131]. In order to enhance the $\beta \rightarrow \alpha$-SiC transformation, annealing treatments were done on all materials and microstructural changes were monitored through SEM investigations (*Figure 4.18*). During annealing, a platelet type of morphology is obtained in the case of 1Lu-2AlN, and the morphology tends to become globular with increasing Lu_2O_3 content within the samples. After prolonged annealing (for 60 h), grain coarsening occurs by coalescence of grains leading to large grains having low aspect ratio (*Figure 4.18 (b), (d) and (f)*). Apart from this microstructural modification, retraction and overall reduction of secondary phases are also observed. As a consequence, all samples underwent a loss of weight and some pores might have been created due to evaporation processes, although they are not visible in the SEM pictures. After prolonged annealing, a double rim structure (*Figure 4.18 (d) and (f)*) is observed due to precipitation of α-SiC on existing α-SiC grains which are formed during sintering. From the density and mass loss data reported in *Table 4.6* it is observed that, after annealing, the extent of recrystallisation is higher in case of material containing a higher amount of Lu_2O_3 and decreases with
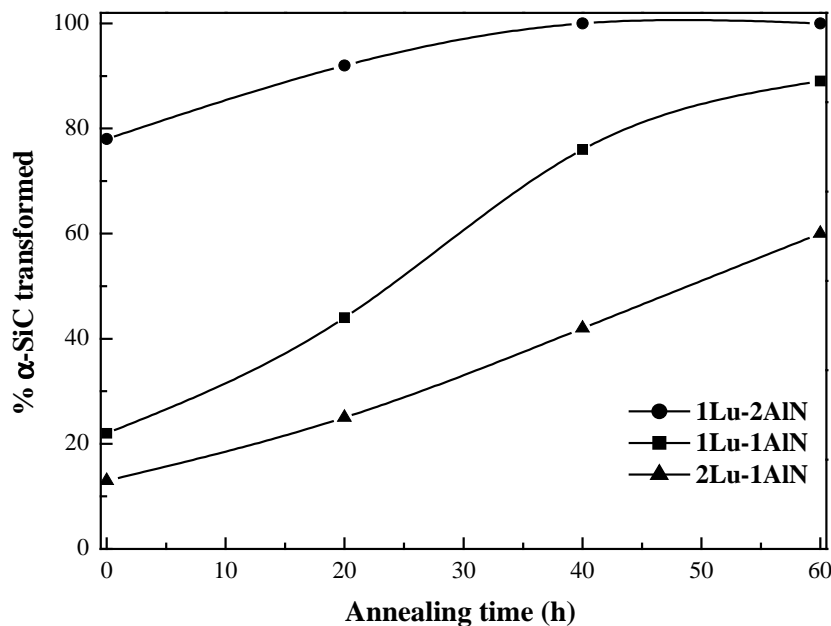
Figure 4.17: $\beta \rightarrow \alpha$-SiC phase transformation as a function of annealing time.

decrease in the Lu_2O_3 content. This suggests that, during sintering, most of the recrystallisation and $\beta \rightarrow \alpha$-SiC transformation occurs within the samples containing less Lu_2O_3. This comes from the refreactory behaviour of the liquid phase which affects the diffusion of the chemical species, solution-reprecipitation mechanism and subsequent crystallisation [136].

Figure 4.18: Microstructures of 20 h annealed LPS-SiC sintered with (a) 1Lu-2AlN, (c) 1Lu-1AlN, (e) 2Lu-1AlN and after 60 h annealing (b) 1Lu-2AlN, (d) 1Lu-1AlN and (f) 2Lu-1AlN.

Table 4.6: Average densities and mass losses of annealed (20 h) SiC samples sintered with different Lu_2O_3:AlN ratios.

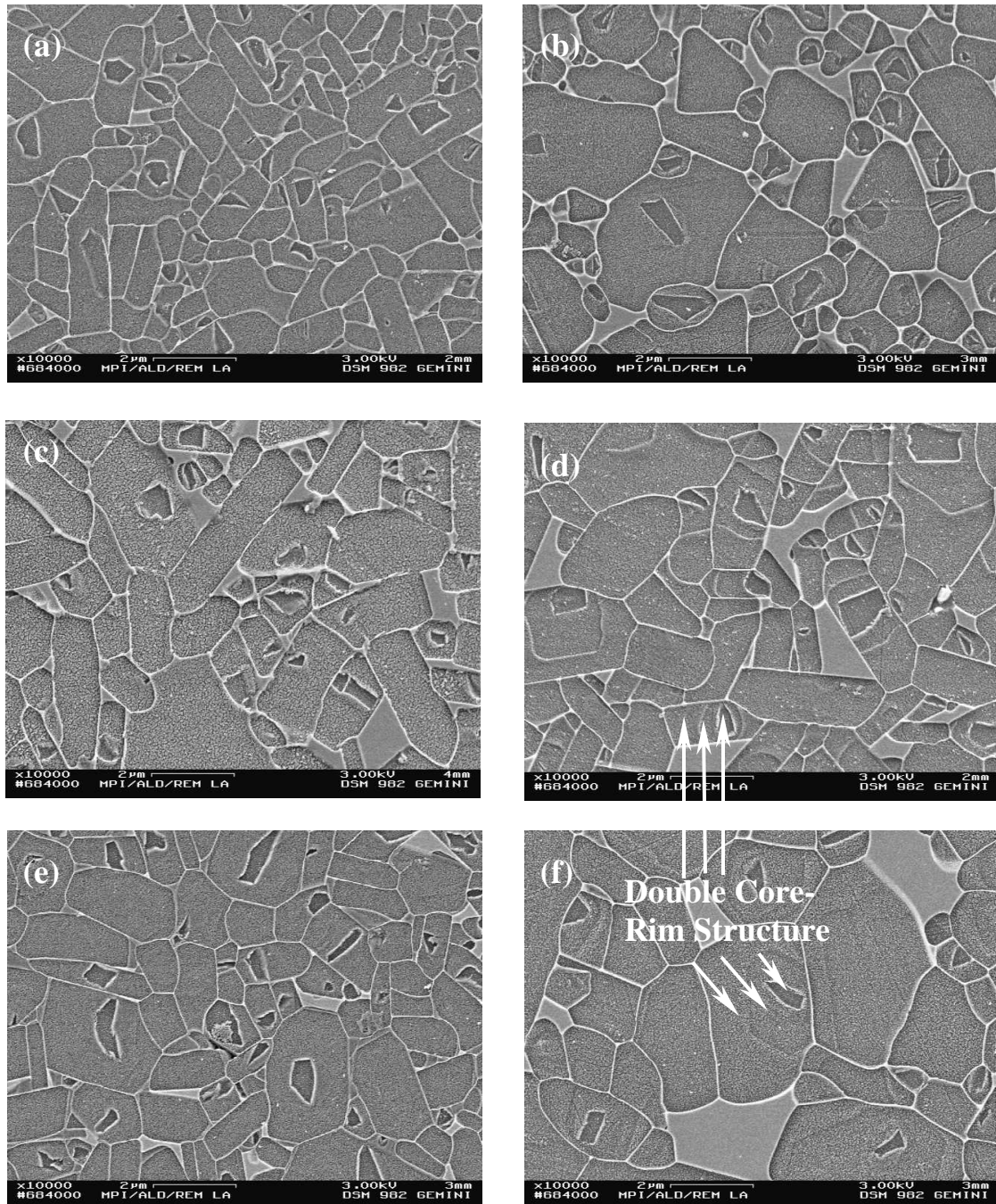| Powder denomination	% Mass loss	Density (g/cm^3)	% Theoretical density	Temperature (°C)	Atmosphere (0.2 MPa)
1Lu-2AlN-AN	0.8	3.60	98.9	1950	N_2
1Lu-1AlN-AN	0.6	3.68	99.3	1950	N_2
2Lu-1AlN-AN	2.8	3.70	98.1	1950	N_2

4.3.3 Fracture toughness and hardness

The hardness and indentation fracture toughness of the three materials were measured and plotted against the annealing time (*Figure 4.19*). In all three compositions, fracture toughness and hardness initially increase with increasing annealing time, whereas constant or decreasing hardness and toughness is observed in case of prolonged annealing. *Figure 4.20* shows the crack paths in as-sintered and annealed samples with different Lu_2O_3:AlN ratios. In as-sintered samples, the crack paths are mostly localised in the secondary phase, showing a predominace of the intergranular fracture mode as a result of the weak interfaces. After annealing for 20 h, grain coarsening occurs resulting in an elongated grain morphology (i.e., higher aspect ratio). In this case, the cracks also propagate mostly along the grain boundaries, but crack deflection occurs by the elongated grains. Hence, the fracture toughness increase in these materials is mainly due to crack deflection mechanisms [134]. Crack bridging and mechanical interlocking (*Figure 4.20*) are also observed as toughening mechanisms in these systems [76,130,136]. However, the fracture toughness decreases after prolonged annealing for 60 h at 1950°C. The long heat treatment causes a depletion in secondary phases due to volatilisation losses (the average secondary phase content after sintering is $11 \pm 0.5\%$ and after annealing is $5.7 \pm 0.3\%$). In addition, grain coarsening occurs with a decrease in aspect ratio. This leads to an increasing tendency for transgranular fracture (*Figure 4.20 (c), (f) and (i)*) and consequently to a decrease in fracture toughness [136,137].

The lowest toughness is reported for the materials containing a higher amount of Lu_2O_3. This is attributed to the globular grain morphology of the as sintered samples where the crack deflection mechanism is less predominant. Apart from that, some transgranular fracture is also observed due to the presence of exaggerated grain growth

after sintering (*Figure 4.20 (g)*). The fracture toughness increases in these systems after annealing, but at a slower rate due to sluggish transformation/recrystallisation of the more refractory secondary phase.
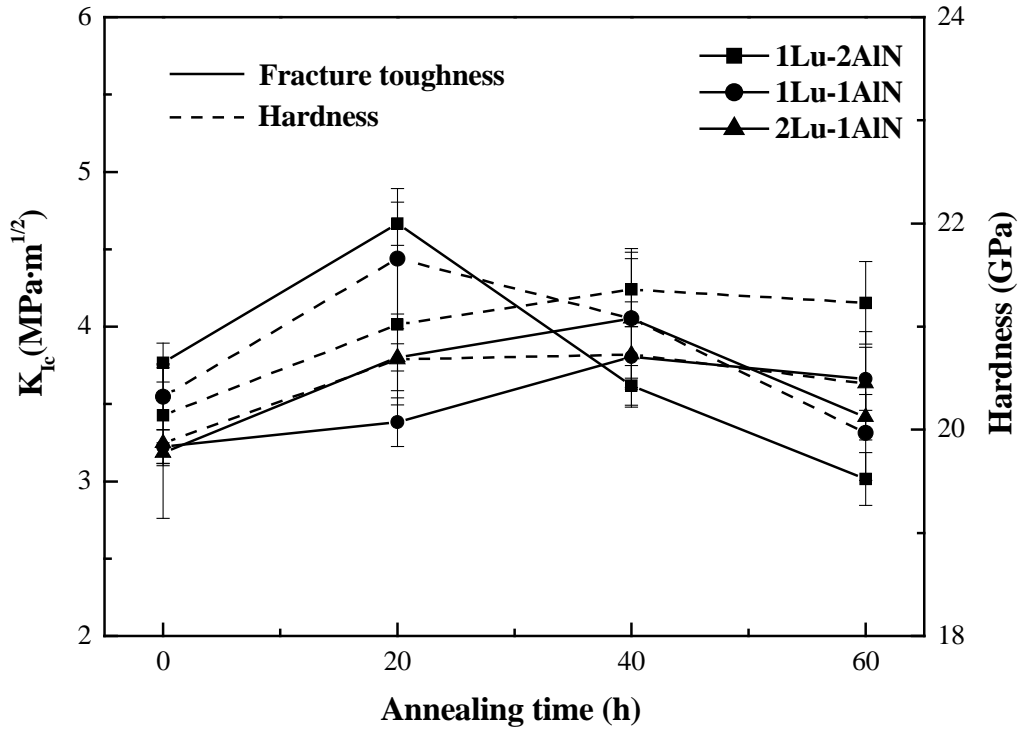
Figure 4.19: Variation of fracture toughness and hardness as a function of the annealing time in SiC ceramics sintered with different Lu$_2$O$_3$-AlN additve systems.

Hardness shows a similar trend as fracture toughness as a function of annealing time for all three systems. The initial increase in hardness corresponds to the crystallisation and reduction of the amount of secondary phases, as it was also observed in other LPS-SiC poly-crystalline material containing amorphous grain boundary phases [130]. After crystallisation, further annealing causes grain growth which reduces the hardness owing to the grain size dependence of the hardness (Hall-Petch like behaviour) [135].

As sintered   **20 h annealed**   **60 h annealed**

Figure 4.20: Crack propagation in as sintered and annealed (20 h and 60 h) SiC ceramics sintered with 1Lu-2AlN ((a), (b) and (c)), 1Lu-1AlN ((d), (e) and (f)) and 2Lu-1AlN ((g), (h) and (i)) additive systems.
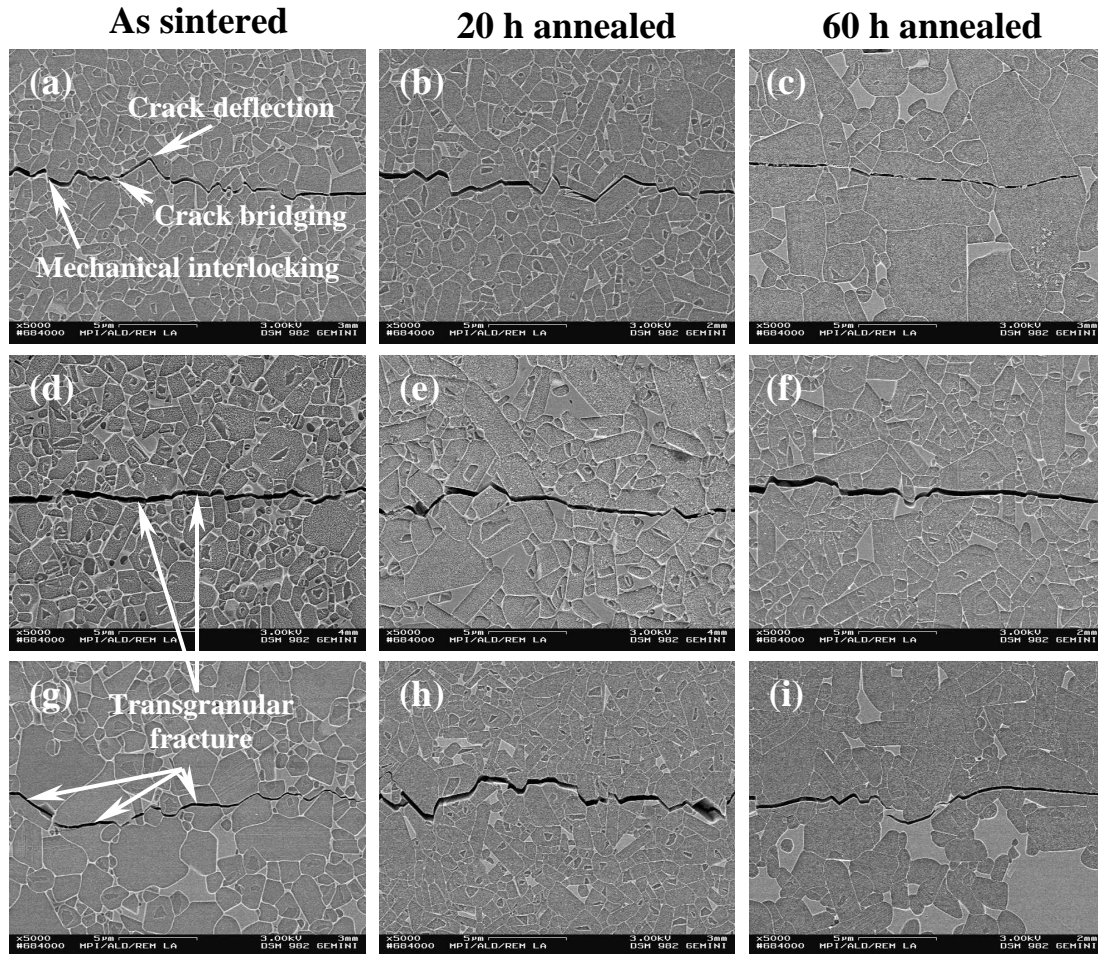
5 Thermomechanical properties

In this chapter, the high temperature behaviour of liquid phase sintered SiC with optimised Lu_2O_3-AlN additive is described. Mechanical properties, specifically bending strength, creep deformation and compliance have been examined in a temperature range from ambient to 1500°C with the objective of characterizing the role of the grain boundary phase. The effect of grain boundary crystallinity, phase compositions and grain morphology on the high temperature strength, creep mechanisms and elastic-plastic behaviour are reported.

5.1 Flexural strength

5.1.1 Effect of temperature

The high temperature strength of the sintered and annealed LPS-SiC with different Lu_2O_3:AlN ratio is measured at different temperatures and is plotted in *Figure 5.1*. A significantly increasing trend is observed from room temperature to 1400°C for the specimens with higher Lu_2O_3 content. Degradation of the high temperature strength in SiC with lower Lu_2O_3 content is related to softening of the intergranular phase [81,130,132]. As the Al content increases, the refractoriness of the intergranular phase degrades as Al^{3+} modifies the silica glass structure by substituting silicon [105,138]. Substitution of Si^{4+} by Lu^{3+} is unlikely due to the large cationic radii difference ($r_{Si^{4+}} = 26$ pm and $r_{Lu^{3+}} = 84.8$ pm) [139]. Apart from that, segregation of Al in the grain boundary phase also deteriorates the high temperature properties [140].

Material containing little Lu_2O_3 shows a continuous drop in strength from room temperature to 1400°C. At 1400°C, only 65% strength retention is observed which is primarily attributed to the grain boundary softening in this material. Specimens with a higher amount of Lu_2O_3 show an increase in strength up to 1200°C followed by a drop in strength until 1500°C. Strength increase occurs probably due to the healing of surface cracks. However, materials with higher Lu_2O_3 content retain up to 93% of their room temperature strength values at 1500°C. At higher temperature (>1200°C), the grain boundary weakens due to the softening effect. Hence, non-uniform deformation such as grain boundary sliding can occur and the stress concentration at triple points

increases resulting in a drop in flexural strength [126]. The same happens in the case of 1Lu-2AlN, however grain boundary softening is predominant at all temperatures resulting in the continuously decreasing strength.

5.1.2 Effect of composition

From *Figure 5.1*, one can see that the room temperature flextural strength increases upon lowering the Lu_2O_3 content in the additive systems. At room temperature, the strength of the polycrystalline ceramics containing secondary phases is mainly governed by the characteristics of the secondary phase, the distribution of grains and their morphology, and flaw/pore sizes [110,130,141,142]. As discussed in the previous chapter, crystallisation of the secondary phases is more pronounced in the material containing little Lu_2O_3. As the mode of fracture is mostly intergranular in these materials, crystallisation of the intergranular phases leads to an increase in flexural strength [130].

Apart from the strengthening effect due to a higher degree of crystallisation, the strength increases due to formation of a bimodal mixture of large elongated and small globular grains in case of the 1Lu-2AlN additive system (*Figure 5.2 (a)*). The enhancement of the flexural strength with the 1Lu-2AlN additive system is attributed to grain bridging caused by elongated grains [143]. The grain size distribution becomes broader (*Figure 5.2 (c) and (e)*) as the Lu_2O_3 content increases in the additive system and hence the effect of grain bridging diminishes. Large globular grains in these systems cause a lowering of the strength according to the σ vs. $\overline{G}^{-1/2}$ relationship [110].

Apart from that, specimens with higher Lu_2O_3 contents reveal higher mismatch in thermal expansion between SiC grains and secondary phase (The thermal expansion coefficient (TEC) of SiC is 4.2×10^{-6} /K and estimated TEC of the secondary phase is of the order of 10^{-5}-10^{-6} /K). This cause and may be microcracks lower hardness (as discussed in chapter 4) and therefore lower strength [108]. Pores and microcracks are deleterious to the strength of ceramics because they act as stress concentrators [108].
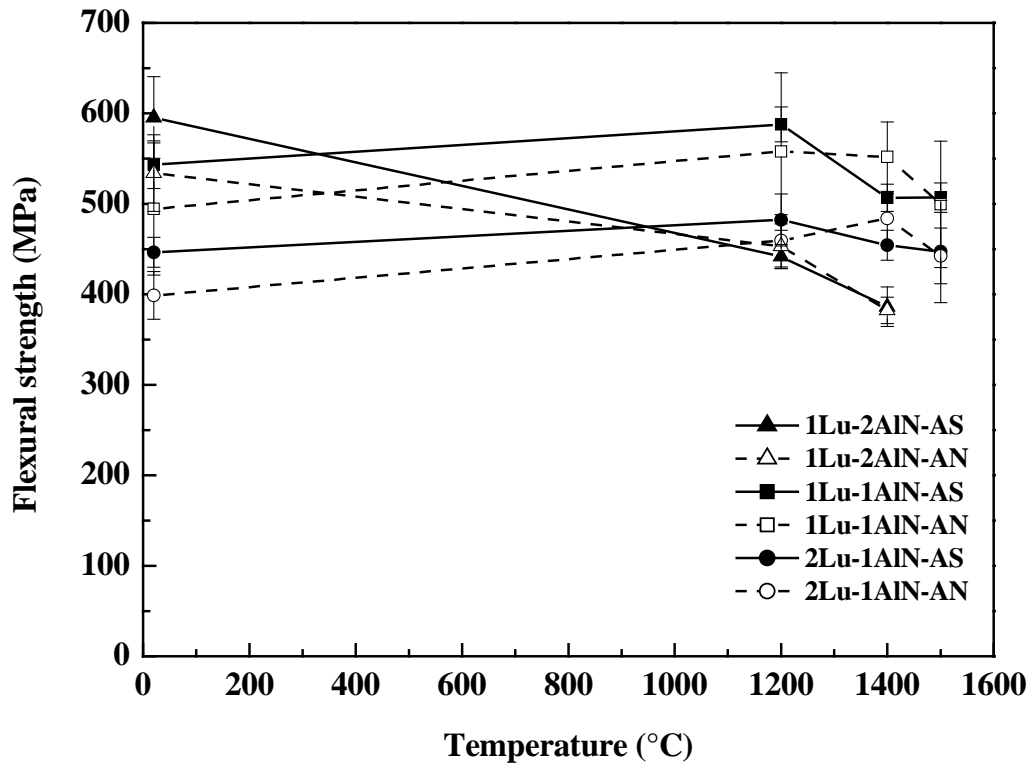
Figure 5.1: Flexural strength of SiC sintered with different Lu₂O₃-AlN additives as a function of temperature. AS = as-sintered and AN = annealed at 1950°C for 20 h.

5.1.3 Effect of annealing

Upon annealing, the room temperature strength decreases due to the change in grain morphology. After thermal treatment, the globular grains become elongated platelets (*Figure 5.2*) and thus the average diameter of the grains ($\overline{G}$) increases resulting in a decrease in strength value owing to the σ vs. $\overline{G}^{-1/2}$ relation [110]. Thus, the coarser microstructure obtained after annealing is beneficial for fracture toughness but detrimental for flexural strength [130,144-147].

After thermal treatment, retraction of the intergranular phase from the grain boundaries to the triple points is observed (*Figure 5.2*) due to a different wetting behaviour of Lu₂O₃ and AlN. By means of TEM (*Figure 5.3*), it is observed that a rather thick heterophase layer is formed between SiC grains and the interior of secondary phase regions (~ 9 nm as compared to 1 nm boundary layer if Y instead of Lu is present [129]), consisting of a Lu-depleted region which suggests poor wettability of the SiC grains by the rare earth element. A similar observation was made by Kim *et al.* [139] who observed that the thickness of the intergranular glassy phase increases
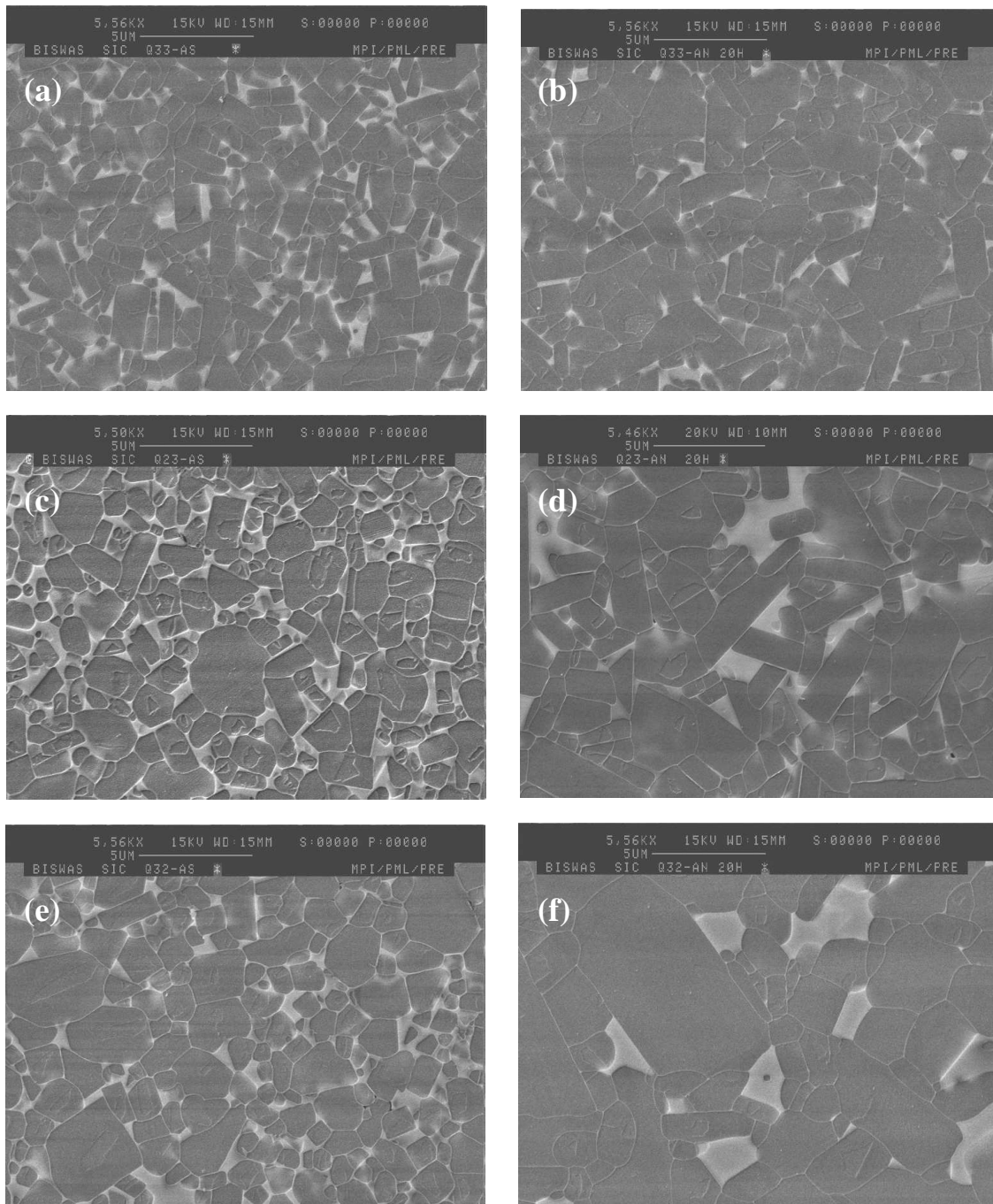
Figure 5.2: Scanning electron micrographs of as sintered [(a) 1Lu-2AlN, (c) 1Lu-1AlN and (e) 2Lu-1AlN] and annealed (20 h) [(b) 1Lu-2AlN, (d) 1Lu-1AlN and (f) 2Lu-1AlN] specimens .

with decreasing cationic radius. However, at 1400°C, the flexural strength of the annealed specimens is higher than that of sintered ones. After annealing, the majority of the grain boundary glassy phase becomes crystallised (see section 4.3.2 and *Figure 4.15* in chapter 4). Such a crystallisation of the grain boundary phase would clearly

minimise the softening and grain boundary sliding and would possibly hinder crack propagation within this region, which would account for the increase in strength [148]. There is almost a 20% increase in strength at 1400°C as compared to the room temperature value for LPS-SiC sintered with 2Lu-1AlN. Reduction in the amount of secondary phase after post sintering heat treatments also improves the high temperature strength [130].
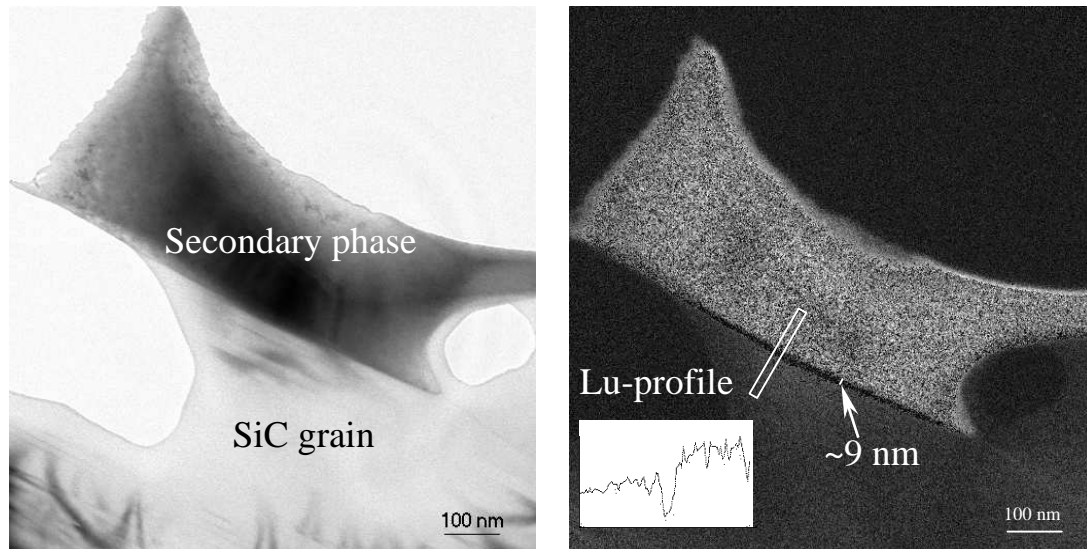
Figure 5.3: Transmission electron micrographs showing EELS line scan of Lu in the hetero-phase boundary between a SiC grain and the secondary phase in SiC sintered with the 1Lu-1AlN additive system.

5.2 Creep

5.2.1 Characteristic behaviour

Figure 5.4 depicts typical creep bending data showing strain as a function of time and applied stress. For a first analysis of creep deformation and for small displacements, the time dependence of creep rate can be neglected and the specimen behaviour can be considered to be steady-state creep [149]. Using the steady-state creep law as represented by equation 2.10 (in chapter 2) is thought to be appropriate in the present case.

Figure 5.4: Typical creep curves showing the effect of temperature and stress on the creep deformation of SiC.

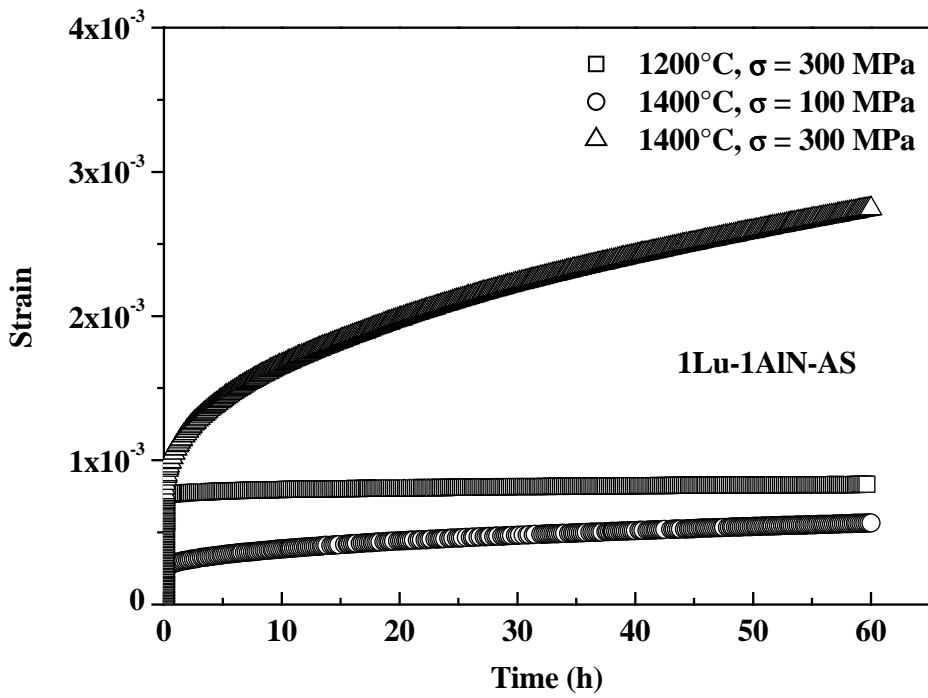The total creep rate $(\dot{\varepsilon}_c)$ is a superposition of the primary creep rate $\dot{\varepsilon}_p$ and the secondary creep rate $\dot{\varepsilon}_s$, i.e.,

$$\dot{\varepsilon}_c = \dot{\varepsilon}_p + \dot{\varepsilon}_s, \tag{5.1}$$

where the primary creep rate is governed by the following equation [150] :

$$\dot{\varepsilon}_p = C \cdot \sigma^n \cdot \varepsilon_p^{-p} \tag{5.2}$$

C is a pre-exponential function depending on temperature, σ is the applied stress, n is the stress exponent and p is the primary strain exponent. This relationship gives a probable estimation of the higher deformation rate at the initial stage of the creep. The length of the transient creep increases with stress and temperature. These tests are electively terminated after 60 h. The creep rates are calculated from the almost linear region of the creep curve, i.e., in the predominantly secondary creep region where $\dot{\varepsilon}_p$

can already be neglected in first approximation (*Figure 5.4*). Here, in particular, the quasi-steady state strain rates are calculated after 20 h of exposure.

5.2.2 Factors influencing the creep behaviour

5.2.2.1 Effect of temperature and stress

The creep rates of SiC ceramics sintered with different Lu_2O_3-AlN additives are plotted in *Figure 5.5* for different temperatures and stress levels. The quasi-steady state strain rates are calculated from a log-log plot of strain rate as a fuction of time. At low temperature and low stress level (1300°C/100 MPa), much scattering occurs in the data because the low deformation rate in this stress and temperature region is close to the resolution limit of the machine.

Furthermore, it is observed at low temperature and at low stress level that the average strain rate is lower in case of the 1Lu-1AlN material, as compared to the other two compositions. As discussed earlier, the degree of deformation depends not only on the viscosity of the intergranular phase, but also on its extent of crystallinity. The viscosity of the amorphous fraction of the intergranular phase is primarily controlled by the amount of rare-earth oxide present in the system and increases with increasing Lu_2O_3 content. However, in as-sintered specimens, the extent of crystallinity decreases with increasing Lu_2O_3 content due to slow diffusion of the chemical species through the highly viscous intergranular phase. So, in the deformation behaviour at 1300°C, there is a trade-off between the extent of crystallinity and the increase of viscosity of the secondary phase. At higher temperature and higher applied stress, the deformation behaviour primarily depends on the viscosity of the secondary phase.

The effect of stress and temperature on the creep deformation of 1Lu-1AlN is depicted in *Figure 5.6*. Temperature plays a predominant role, as suggested by the steady-state creep rate equation 2.10. With increasing stress, no morphological changes hinting deformation of SiC grains during the creep tests are visible at the tensile surface of the crept specimens (*Figure 5.7*). However, a decrease in the viscosity of the secondary phase is likely to occur with increasing stress. It has been observed that the viscosity of silicate melts follows an inverse relationship with the square of the applied stress [150]. So, viscosity drops at high stress level resulting in high creep deformation rate.
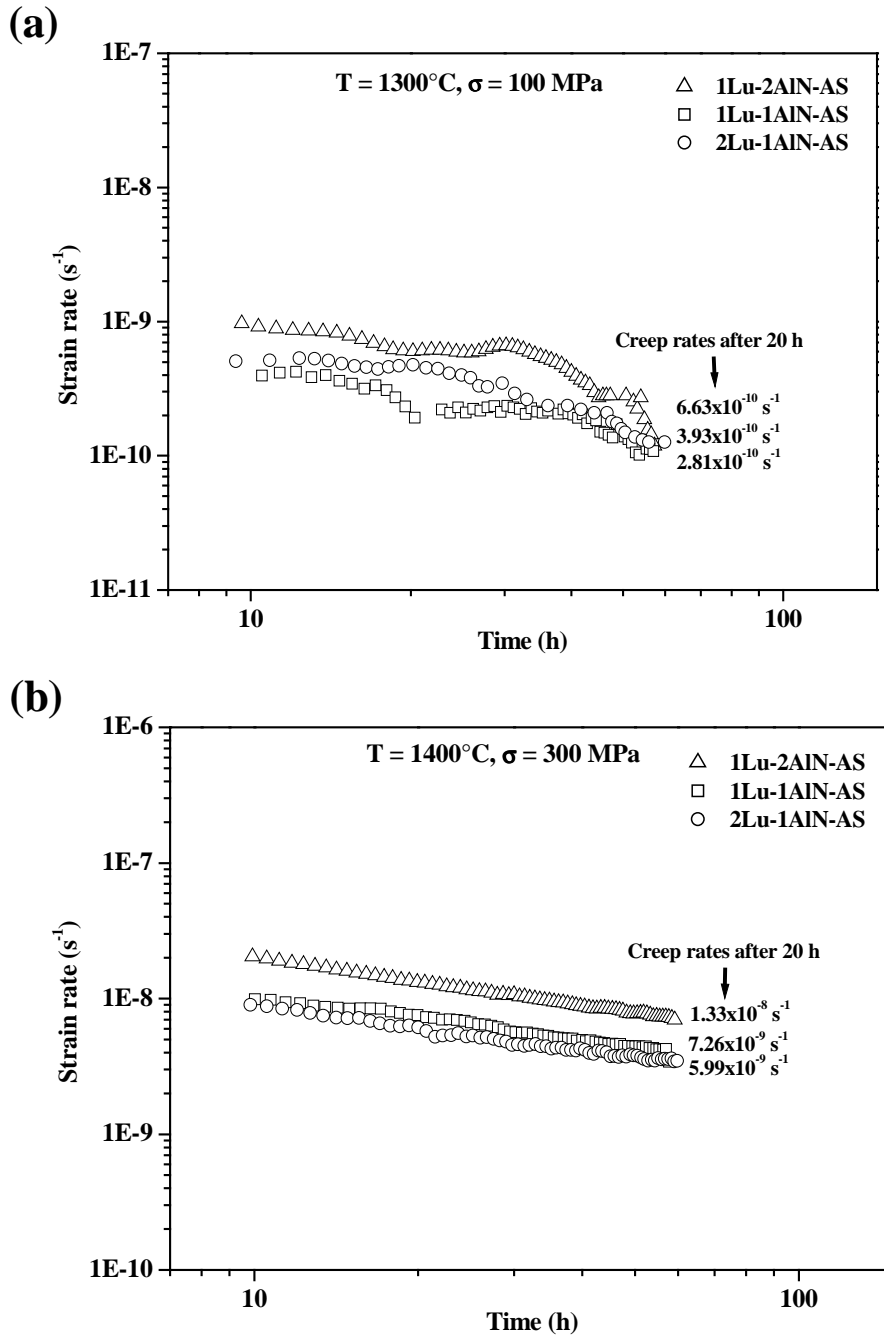
Figure 5.5: Effect of temperature and stress on the creep rates of SiC sintered with different additives (a) low temperature, low stress, (b) high temperature, high stress.
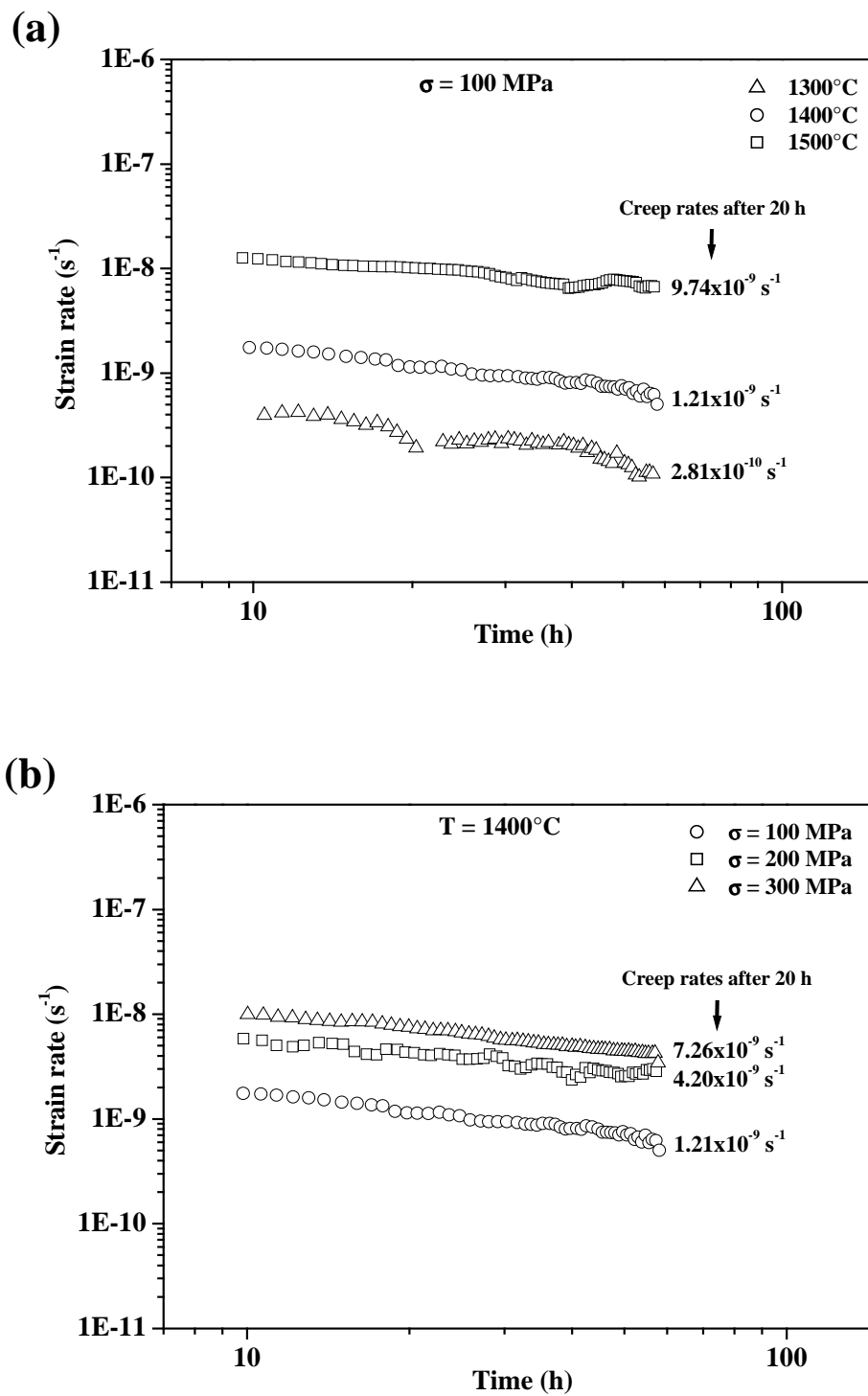
Figure 5.6: Creep rate variation as a function of (a) temperature and (b) stress for SiC sintered with the additive system 1Lu-1AlN.
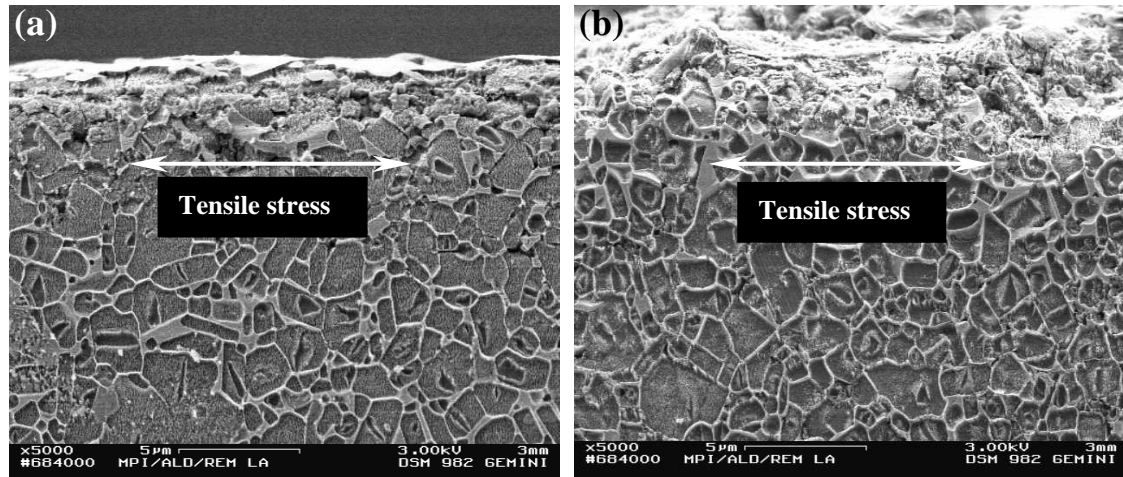
Figure 5.7: Microstructure of 1Lu-1AlN samples crept at (a) 1400°C and (b) 1500°C for 60 h at 100 MPa showing no grain deformation along the tensile axis.

5.2.2.2 Effect of composition

Figure 5.8 depicts the creep behaviour as a function of compositional variation in different LPS-SiC systems at an applied stress of 300 MPa. At higher temperature (1400°C), the creep rate increases upon lowering the Lu_2O_3 content in the additive systems owing to the fact that the viscosity of the secondary phase in the samples with lower Lu_2O_3 content goes down. However, as discussed in the previous section for a different set of creep conditions, the low temperature (1300°C) deformation is dictated by both the viscosity and the extent crystallisation of the secondary phase after sintering. Consequently, a higher creep resistance for the material with 1Lu-1AlN is observed.

5.2.2.3 Effect of annealing

Figure 5.9 shows a comparison between creep curves of as-sintered specimens with specimens annealed at 1950°C for 20 h. Comparison of the strain rates shows that there is no significant improvement of the creep rates (calculated after 20 h) upon annealing. The slight decrease in the creep rates corresponds to the partial crystallisation of the intergranular phase and the decreasing amount of secondary phases upon annealing. However, partial devitrification of the amorphous phases may also occur during the long creep test and hence, the influence of the annealing treatment diminishes with testing time.

(a)

(b)
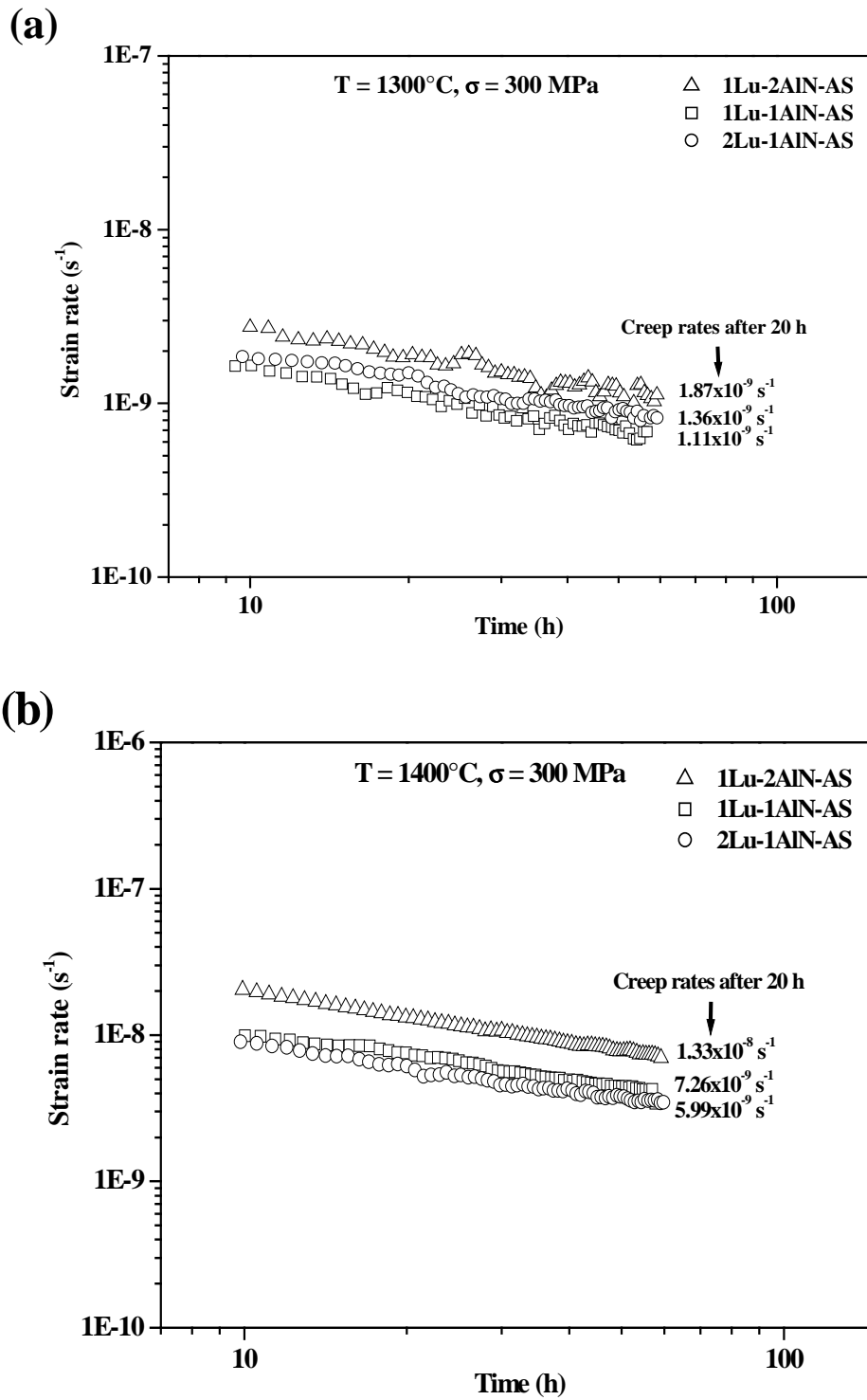
Figure 5.8: Variation of creep rates for different compositions, at (a) 300 MPa, 1300°C and (b) 300 MPa, 1400°C.
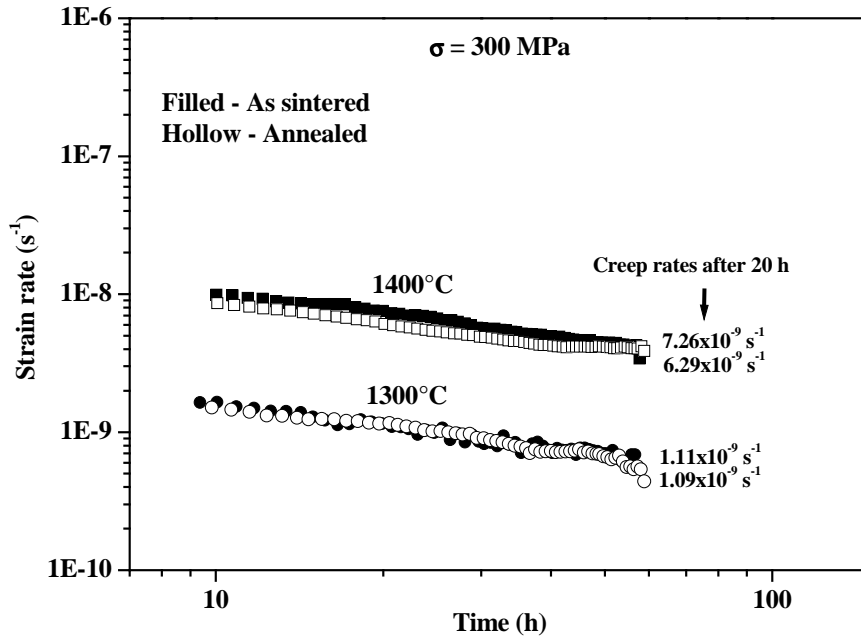
Figure 5.9: Influence of 20 h annealing at 1950°C on the creep rates of 1Lu-1AlN material at different temperatures.

5.2.3 Creep parameters evaluation

For different levels of stress and at different temperatures, creep parameters are determined from incremental stress or temperature changes using the general constitutive creep equation 2.10. Stress exponents, *n*, and activation energies, *Q,* are determined from the logarithmic plots of strain rate ($\dot{\varepsilon}$) vs. stress (σ) and vs. reciprocal temperature ($1/T$), respectively. These results are compared in *Figure 5.10* and *Figure 5.11*. The calculated activation energies are tabulated in *Table 5.1*.

The stress exponents in sintered and annealed SiC with different Lu_2O_3:AlN additives range from about 1 to 1.7. The activation energies vary from 200 to 500 kJ/mol which is in accordance with values given in the literature [117,118].

Figure 5.10: Plots of strain rate vs. stress. The temperature of the tests and stress exponents obtained are indicated.

Figure 5.11: Plot of strain rates at 100 MPa and 300 MPa vs. reciprocal temperature.
The activation energies obtained are reported in Table 5.1.

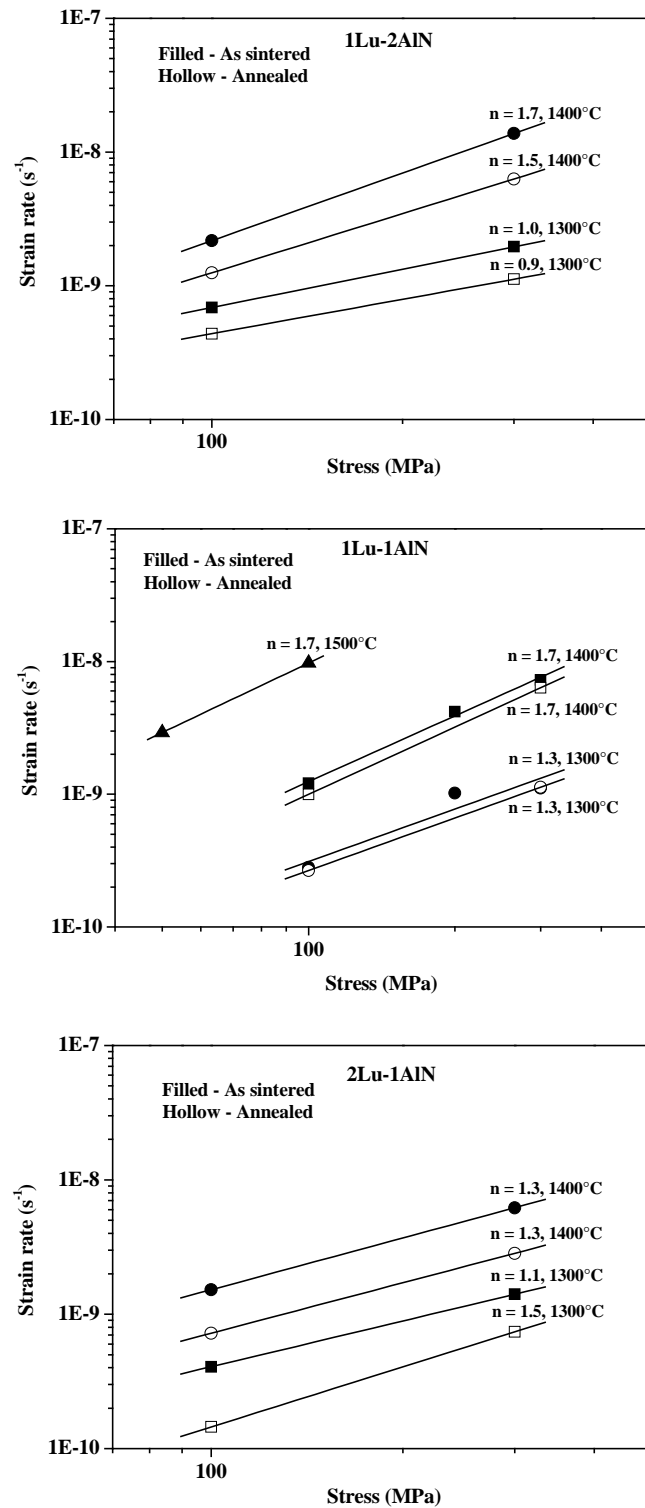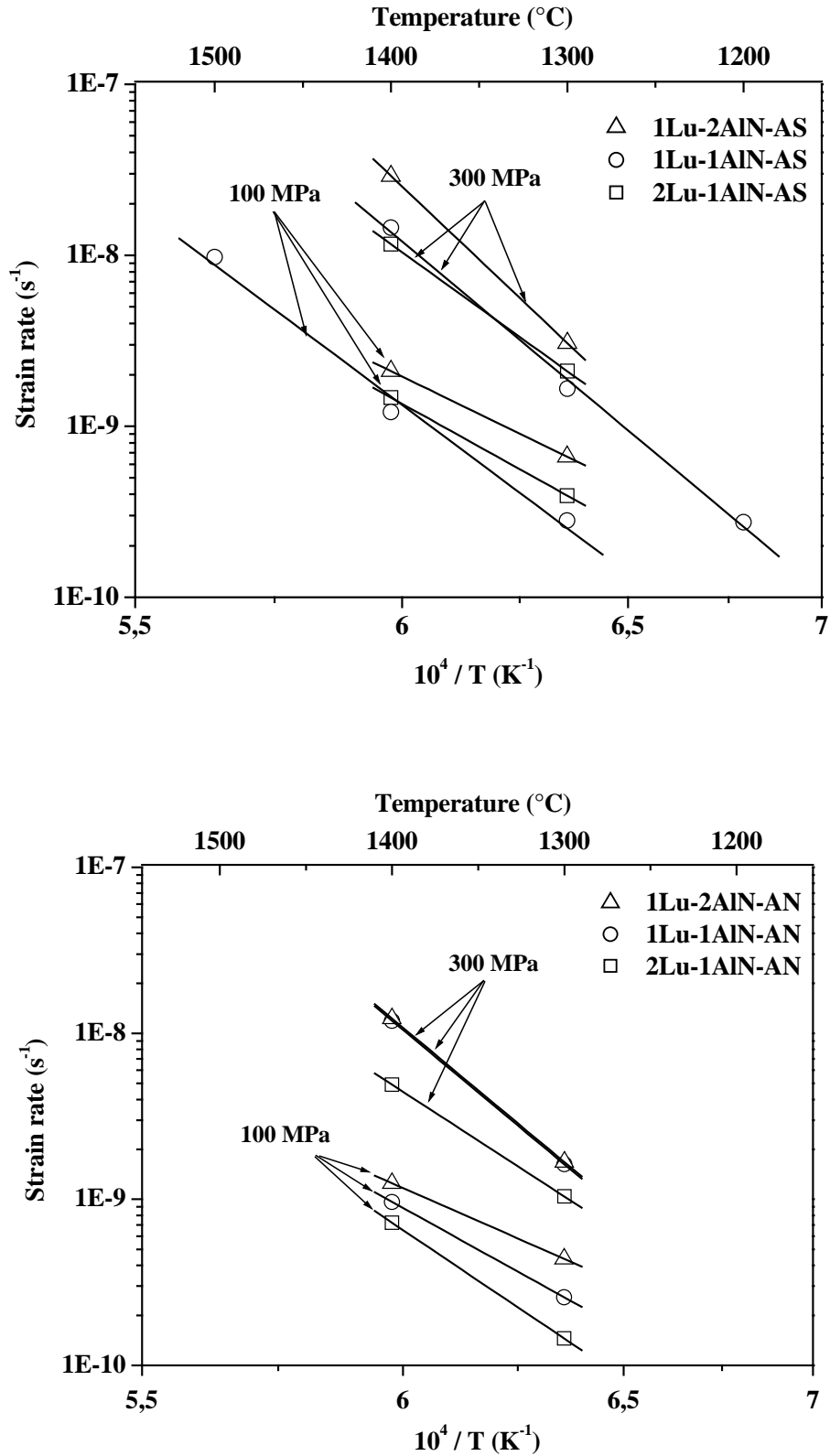*Table 5.1: Activation energies for different materials at different stresses and in different temperature ranges.*

Material	Sintered					Annealed	
	Temperature range					Temperature range	
	1200-1400°C	1300-1400°C			1300-1500°C	1300-1400°C	
Stress (MPa)	300	100	200	300	100	100	300
1Lu-2AlN	—	252		427	—	229	378
1Lu-1AlN	352	319	310	411	411	289	378
2Lu-1AlN	—	289		324	—	352	294

The microstructures of the non-crept and crept samples are shown in *Figure 5.12*. At the surface of the crept specimens, cavities are observed (*Figure 5.12(b)*) whereas no microstructural changes have been observed inside the crept samples (*Figure 5.12(c)*) as compared to non-crept ones (*Figure 5.12(a)*). Cavities, observed only near the surfaces, are formed both at two grain or multiple grain junctions. No grain elongation is observed at the tensile surface of the specimen. The maximum strain in these materials is 0.5% only, corresponding to a maximum displacement of the bending bars of 150 µm during the creep tests.

XRD analysis is used to evaluate the phase compositions of the as-sintered specimens after the completion of the 60 h bend creep tests. After the 60 h bend creep test in air, specimens with more Lu_2O_3 in the secondary phase form surface oxides consisting of $Lu_2Si_2O_7$, Lu_2O_3 and SiO_2 phases (*Figure 5.13*). The specimens containing more AlN form $Lu_2Si_2O_7$ and $Lu_4Si_2O_7N_2$ along with trace amounts of Lu_2O_3. Samples crept for 60 h at 1400°C show Lu_2O_3 and SiO_2 on the surface together with some $Lu_2Si_2O_7$. However, at 1500°C, the extent of disilicate formation increases at the expense of SiO_2 and Lu_2O_3. No traces of Al-containing phases have been found in these samples. Since the Al and Lu concentrations are comparable (but Lu has a much larger scattering cross section than Al), this would give a hint that crystalline Al-containing phases, if present al all, are largely Lu-free. The kinetics of disilicate formation will be discussed in the next chapter in connection with the oxidation behaviour of the samples.
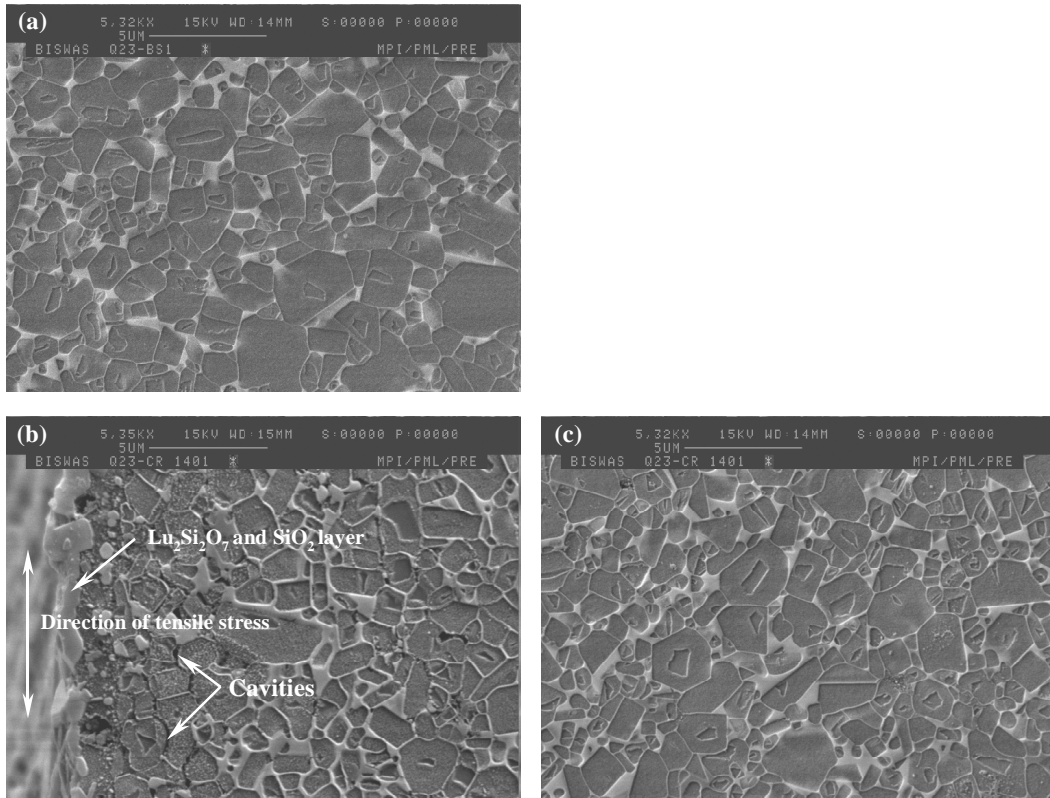
Figure 5.12: SEM images of the 1Lu-1AlN specimen. (a) before creep, (b) surface of the crept specimen and (c) interior of the specimen after creep test at 1400°C with 100 MPa stress for 60 h in air.
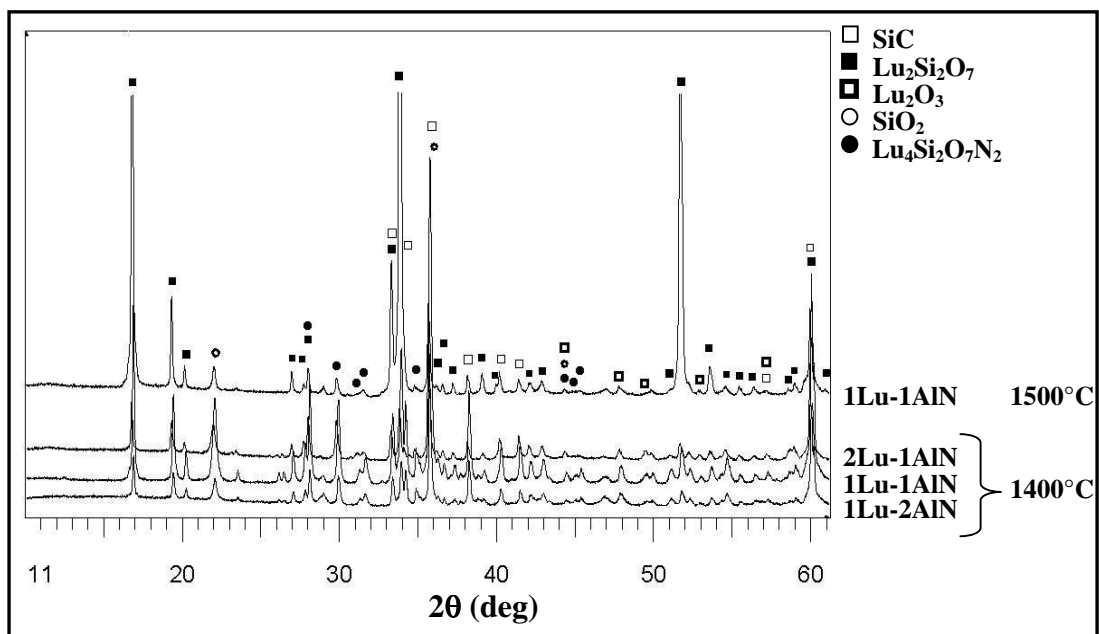

Figure 5.13: XRD patterns obtained from the surface of the different specimens crept at different temperatures for 60 h.

5.2.4 Creep mechanisms

In case of SiC sintered with Lu_2O_3-AlN additives, the stress exponent lies within the range of 1 to 2 and extensive microstructural modification is not observed after creep testing. Nagano [151] found that the flow stress dependencies in compression and tension tests were almost same below a strain of 0.5. So, the main deformation mechanisms were thought to be the same in compression and in tension. In general, a linear flow stress dependency suggests that the creep deformation is controlled by diffusion processes [152]. It is reported, however, that viscous flow also showing a stress exponent of n = 1 is a likely deformation mechanism in amorphous solids [153]. Somewhat higher stress exponents indicate that other mechanisms may also contribute to the deformation. One of them is creep cavitation, however, creep cavitation damage and vapourisation from the near-surface region of the samples may be superimposed, making it difficult to draw conclusions concerning the creep cavitation deformation mechanism from the microstructural observation. Stress exponents of n ~ 2 suggest that bending creep is primarily influenced by interfacial reaction, intergranular glass phases, solution-reprecipitation, grain-boundary sliding and cavity formation [118,119,151,154-157]. Among those, microstructural evidence rules out the possibility of solution-reprecipitation during testing because there is no morphological change inside the SiC-grains.

Although activation energy is not considered as a sharp criterion for the creep mechanism, comparison of the values can give some information about possible creep mechanisms. Gallardo-López *et al.* [158] found an activation energy of 840 ± 100 kJ/mol in compressive creep of LPS-SiC with a stress exponent of 1.6 ± 0.2. The mechanism prevailing in their case was found to be dislocation glide accomodated by lattice diffusion at higher temperature. The activation energy corresponds to the self-diffusion of C and Si. A much lower activation energy is found in the present investigation as compared to their findings. Compared to the present study, similar activation energies (338-434 kJ/mol) were observed by Lane *et al.* [117] and Nixon *et al.* [159] in their respective studies with stress exponents of 1.4-1.7. The creep mechanism in their studies is grain boundary sliding accomodated by grain boundary diffusion. The activation energies are very close to the activation energy for viscous flow of pure SiO_2 ($\approx$ 440 kJ/mol) [120,160]. Comparing the activation energies associated with creep deformation along with the stress exponent, the controlling creep

mechanism in the present systems is supposed to be grain boundary sliding accomodated by diffusion along the grain boundary film/silicon carbide interface. A parallel mechanism, namely cavitation, may be operative above 1400°C. However, from the microstructural observation, it is difficult to establish this fact due to the simultaneous occurrence of volatilisation of the intergranular phases near the surface region.

5.2.5 Comparison with the "conventional" Y_2O_3-AlN system

Figure 5.14 shows the creep curves of different samples under 100 MPa stress at 1400°C. It is observed that the sample with the sintering additive 1Lu-1AlN has the lowest creep rate of all tested materials. By comparison with the material 3Y-2AlN annealed for 16 h at 1950°C, this system is established to exhibit better creep resistance.
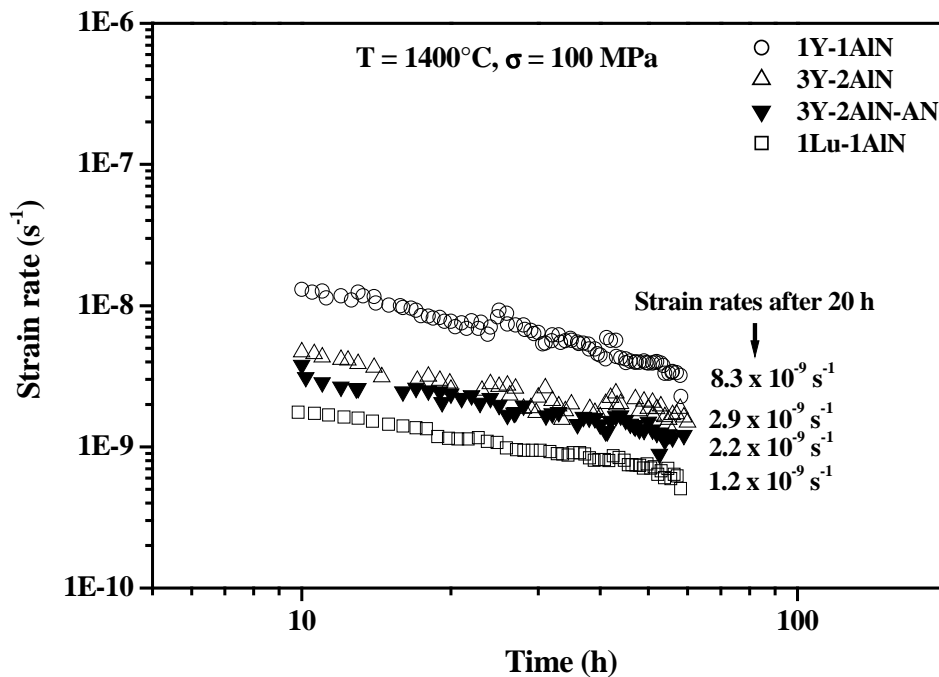

Figure 5.14: A comparison of creep rates for LPS-SiC showing the improved creep resistance of the Lu_2O_3-AlN additive system as compared to the "conventional" Y_2O_3-AlN additives.

5.3 Elastic-plastic behaviour

High temperature compliance tests are perfomed in order to understand the elasto-plastic behaviour under constant stress-rate testing over a wide temperature range (RT to 1450°C). *Figure 5.15* shows typical stress-strain diagrams recorded at different temperatures. The shape of the stress-strain loop changes with increasing temperature. This change is characterised by an increase of the hysteresis loop area which corresponds to increase in plastic-anelastic deformation and an increase in strain per unit of applied stress which means a decrease in stiffness. In order to understand the degradation of the elastic properties, stiffness values have been calculated from the slope of the loading-unloading curve.

The increase in the hysteresis loop area corresponds to energy-dissipating processes due to, e.g., the decrease in the interfacial sliding resistance between the SiC grains and intergranular phase [161]. In other words, the increase in loop area with increase in temperature at a constant maximum load can be correlated with the creep relaxation.
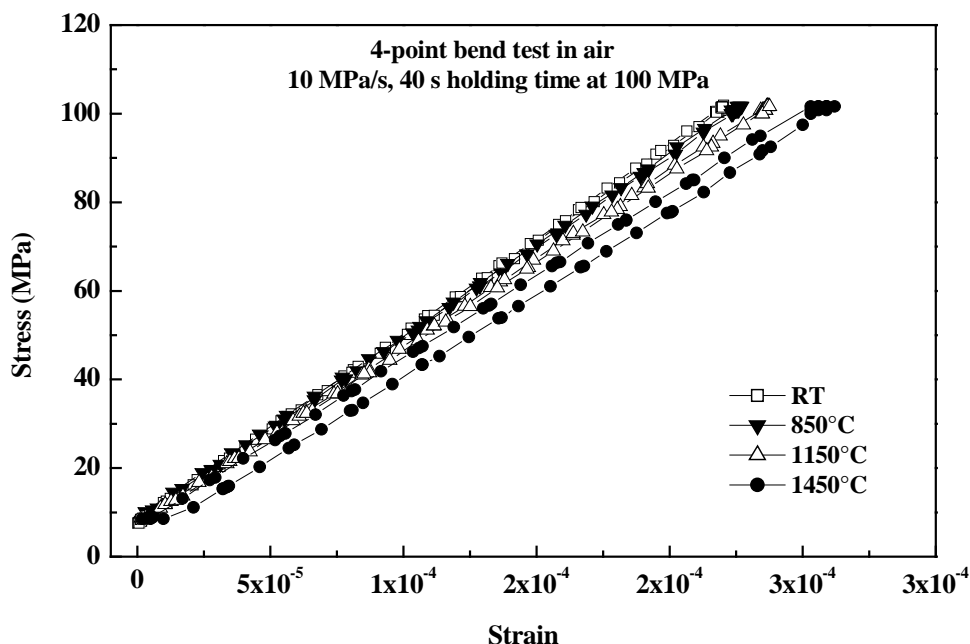
Figure 5.15: Typical stress-strain diagram at different temperatures for SiC sintered with 1Lu-1AlN additive.

From the compliance test, two major parameters, stiffness and hysteresis loop area are determined and plotted in *Figure 5.16* as a function of temperature. The stiffness, calculated from the slope of the loading-unloading curve, essentially characterises the elastic and fast recoverable anelastic components of the material's behaviour. The slow anelastic and plastic behaviour can be determined from the loop area.
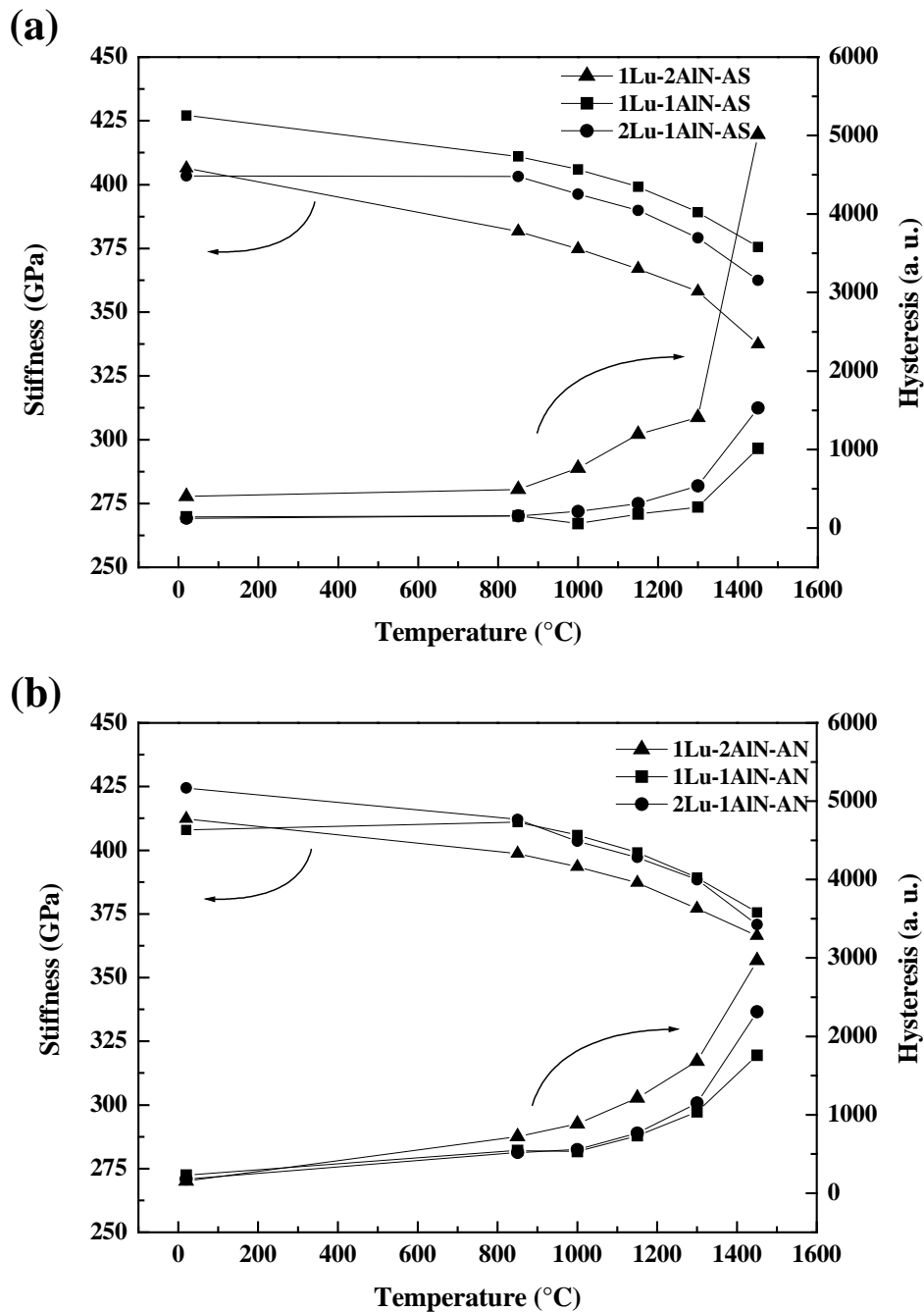
Figure 5.16: A comparison of high temperature compliance test results for different compositions after (a) sintering and (b) annealing at 1950°C for 20 h.

Inevitably, for all compostional variations, the increase in temperature yields a decrease in stiffness of the material (*Figure 5.16*). A similar behaviour is observed in the anelastic-plastic characteristics where the area under the hysteresis loop increases with increasing temperature showing the softening of the material.

5.3.1 Effect of composition

Figure 5.16(a) shows the effect of the composition of the as sintered material on high temperature compliance. In the case of the material containing a lower amount of Lu_2O_3, the stiffness and plastic-anelastic properties are inferior due to the poorer refractoriness of the secondary phase. One of the mechanisms that operate in the plastic behaviour at elevated temperature is grain boundary sliding. As discussed earlier, the trade-off between the extent of crystallisation and the refractoriness of the secondary phases gives rise to superior thermomechanical behaviour in the case of 1Lu-1AlN as compared to other two compositions in the Lu_2O_3-AlN additive system.

5.3.2 Effect of annealing

Upon annealing, intergranular phases crystallise which improves the thermo-elastic behaviour of the material owing to the fact that the crystalline phases have better refractoriness than the amorphous phase. Although, after annealing, there is a retraction of Lu from heterophase boundaries to triple points (*Figure 5.2*) which may deteriorate the high temperature elastic-plastic behaviour due to inhomogeneous distribution of the secondary phases. However, overall elastic-plastic behaviour improves after annealing.

5.3.3 Comparison with the "conventional" Y_2O_3-AlN system

It is evident from *Figure 5.17* that high temperature stiffness as well as plastic-anelastic deformation behaviour are improved by the substitution of Y_2O_3 by Lu_2O_3. The deformation associated with viscous flow is diminished because of the more refractory nature of the grain boundary phase in the system Lu_2O_3-AlN as compared to the Y_2O_3-AlN additive system.
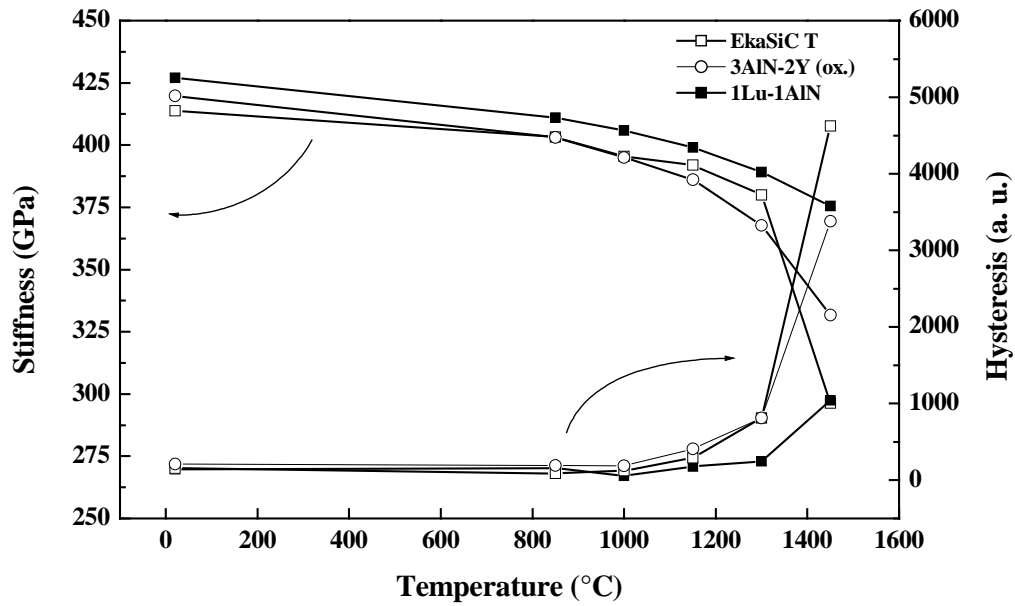
Figure 5.17: LPS-SiC with Lu₂O₃-AlN additive exhibiting superior thermo-elasto-plastic behaviour as compared to a "conventional" Y₂O₃-AlN additive. EkaSiC T is a commercial material (ESK, Kempten, Germany) which contains mainly yttrium-aluminium garnet (YAG) as a secondary phase.

6 Oxidation

Figure 6.1 shows the specific mass gain for specimens oxidised in air at temperatures between 1200 and 1500°C. The specific mass gains increase with temperature for all the compositions. For all specimens, the oxidation kinetics are observed to be of the parabolic type. Thus, the oxidation behaviour is governed by the parabolic rate equation:

$$\Delta W^2 = k_p\, t \qquad\qquad\qquad (6.1)$$

where ΔW is the weight gain per unit surface area, k_p is the rate constant of parabolic oxidation and t is the exposure time. From plots of weight gain versus time, the parabolic rate constants are determined for all systems at different temperatures and are listed in *Table 6.1*. The activation energies are also calculated from Arrhenius plots of the parabolic rate constants (*Figure 6.2*) and tabulated in *Table 6.1*.

Table 6.1: Weight gain and parabolic rate constant (k_p) for different additive systems after oxidation at different temperatures.

| Material	1Lu-2AlN	1Lu-1AlN	2Lu-1AlN
Weight gain (1200°C, 100 h, mg·cm^{-2})	0.16	0.20	0.35
Rate constant at 1200°C, k_p (kg^2·m^{-4}·s^{-1})	5.43×10^{-12}	8.72×10^{-12}	3.33×10^{-11}
Weight gain (1400°C, 100 h, mg·cm^{-2})	0.53	0.57	0.40
Rate constant at 1400°C, k_p (kg^2·m^{-4}·s^{-1})	7.94×10^{-11}	4.11×10^{-11}	8.58×10^{-11}
Weight gain (1500°C, 100 h, mg·cm^{-2})	1.52	1.24	1.13
Rate constant at 1500°C, k_p (kg^2·m^{-4}·s^{-1})	6.44×10^{-10}	4.24×10^{-10}	3.59×10^{-10}
Activation energy between 1200-1500°C (kJ/mol)	561 ± 67	460 ± 60	251 ± 184
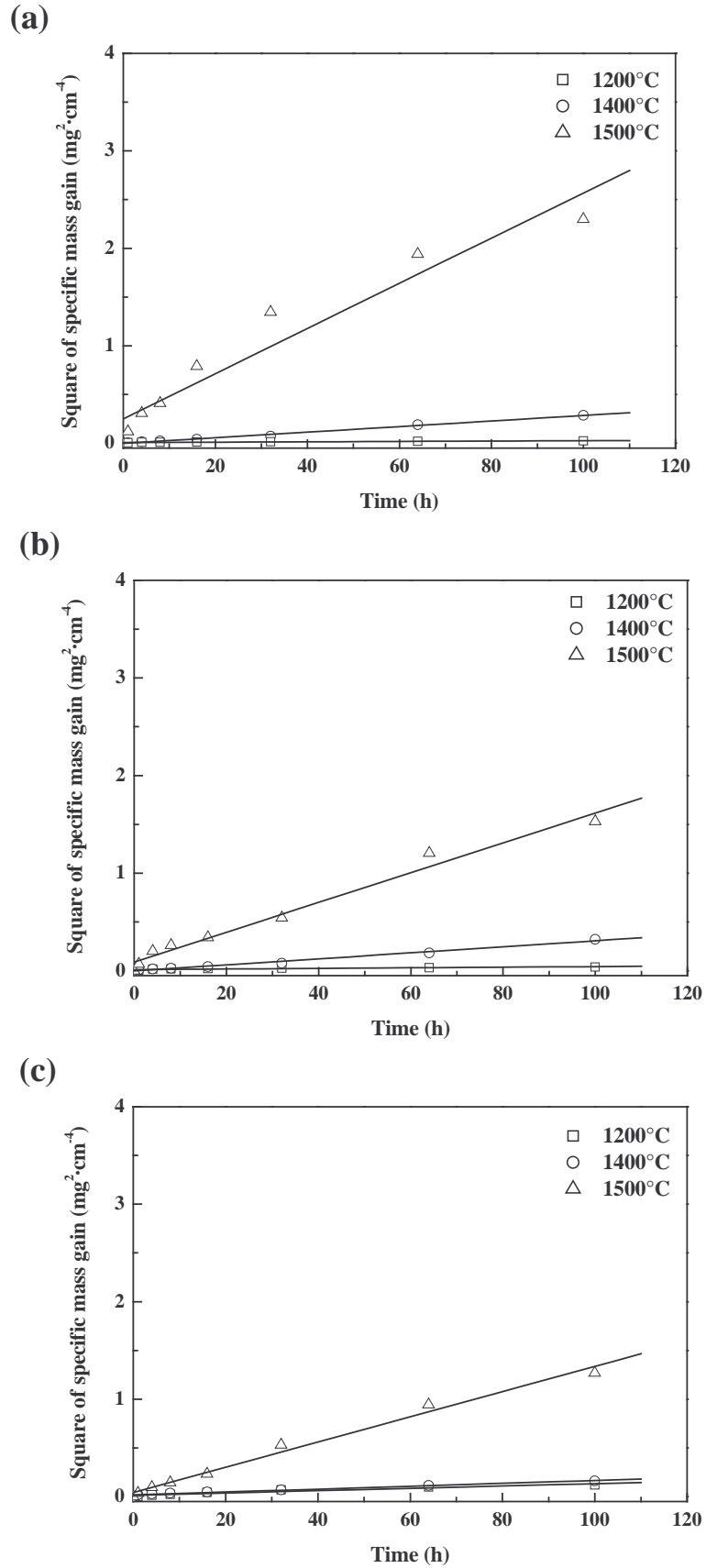
Figure 6.1: Parabolic relationship between weight gain and time for (a) 1Lu-2AlN, (b)1Lu-1AlN and (c) 2Lu-1AlN at different temperatures.
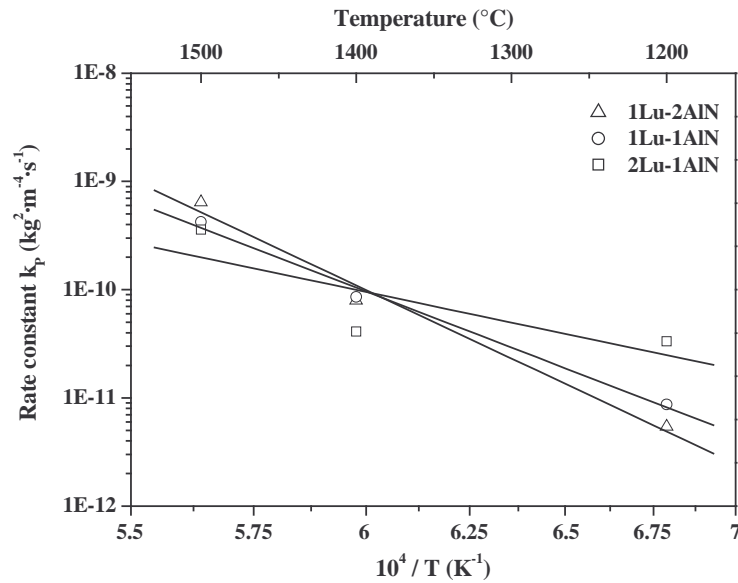
Figure 6.2: Arrhenius plot of parabolic rate constants for oxidation.

An interesting aspect can be observed in *Figure 6.2*, which summarises the oxidation behaviour of three materials with different Lu_2O_3 contents, namely the differences in the temperature dependence of rate constants. At high temperature ($\geq 1400°C$), materials containing higher amounts of Lu_2O_3 are more resistant to oxidation, and below that, the lowest weight gain corresponds to the material containing more AlN in the additive system. This difference in oxidation resistance between the three compositions is believed to be related to the characteristics of the intergranular phases of the systems. At low temperature ($<1400°C$), the better oxidation resistance exhibited by the 1Lu-2AlN containing material is not surprising since its intergranular phase after sintering is more crystalline which makes difficult to oxygen to diffuse through the intergranular phase and thereby improving the oxidation resistance. On the other hand, at higher temperature ($\geq 1400°C$), the material containing more AlN is less resistant to oxidation because probably, at those temperatures, the oxidation products Al_2O_3 (forms after oxidation of AlN [162]) along with SiO_2 (forms due to the oxidation of SiC) form low viscous phases (eutectic point in the system Al_2O_3-SiO_2 is $1587 \pm 10°C$ [163]) which increases the permeability of the oxide layer for oxygen. So, the diffusion of rare earth cations to the surface is facilitated and larger quantities of oxide products ($Lu_2Si_2O_7$) are formed by reaction with SiO_2 formed during early stages of oxidation (passivation of SiC grains). So, oxidation proceeds by formation of new SiO_2 which further reacts with Lu_2O_3 to form $Lu_2Si_2O_7$.
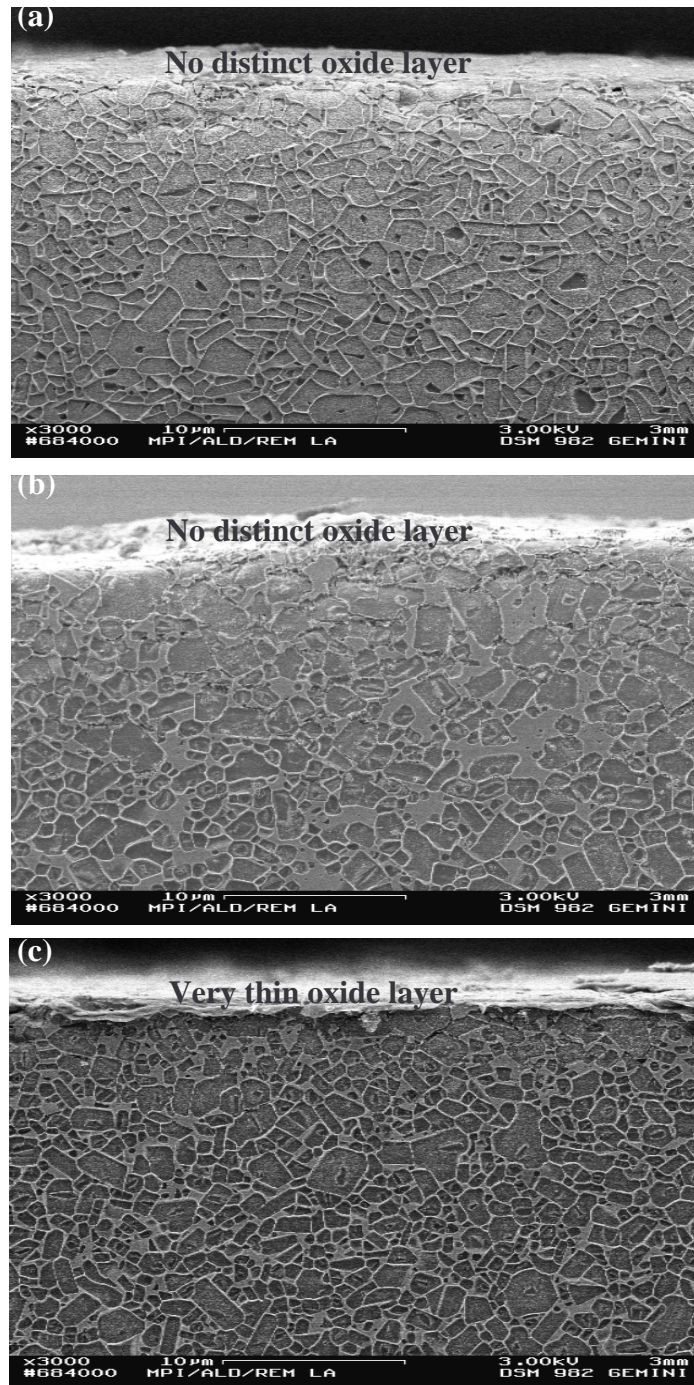
Figure 6.3: SEM images of the oxidised specimens after 100 h at 1200°C in air, (a) 1Lu-2AlN (b) 1Lu-1AlN and (c) 2Lu-1AlN. The images show that a thin oxide layer is visible in case of the high Lu_2O_3 content-material (c), as compared to the other two (a and b). This is true at temperatures <1400°C.

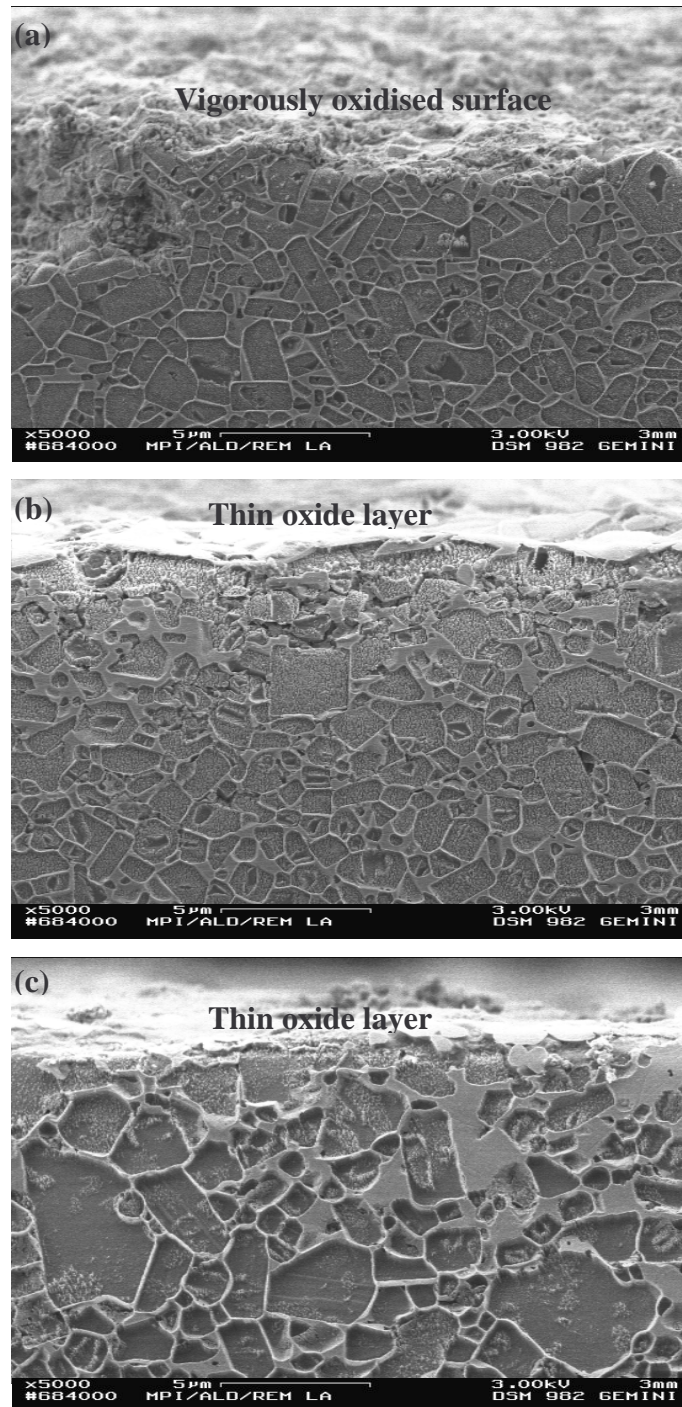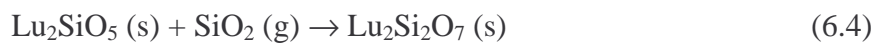*Figure 6.4: SEM images of oxidised specimens after 100 h at 1500°C in air, (a) 1Lu-2AlN (b) 1Lu-1AlN and (c) 2Lu-1AlN. The images shows a vigorously oxidised surface in case of the material containing little Lu_2O_3 (a) as compared to the other two (b and c). This suggests that the oxidation resistance is deteriorated with decreasing Lu_2O_3 content in the intergranular phase at higher temperatures ($\geq$1400°C).*

Mechanism

For each of the present materials, a faster oxidation rate than expected according to the parabolic rate law was observed during the initial stage of oxidation. This may be due to the surface pits and cracks of the specimens which allow ingress of oxygen into a surface layer of finite thickness. In this case, the measured parabolic rate constant is not valid because no defined oxide layers formed to control the oxidation rate.

It has been proposed that the parabolic oxidation behaviour of ceramics indicates that the rate-determining step is a diffusional process associated with the migration of ions (cation diffusion through the grain boundary phase and/or anion diffusion through the oxide film) [99,164,165]. High activation energies (250-560 kJ/mol), as found in the present study, suggest that oxidation proceeds not only by the diffusion of oxygen ion through the SiO_2 layer ($Q_{ox} \sim 150$ kJ/mol), but also by interfacial reactions between the growing SiO_2 layer and Lu_2O_3. Presumably, silica formed by the oxidation of SiC reacts with secondary phases ($Lu_4Si_2N_2O_7$, Lu_2O_3) and forms $Lu_2Si_2O_7$ by the following reactions [166] :

$$SiC \text{ (s)} + 2O_2 \text{ (g)} \rightarrow SiO_2 \text{ (s)} + CO_2 \text{ (g)} \hspace{2cm} (6.2)$$

$$2Lu_4Si_2N_2O_7 \text{ (s)} + 3O_2 \text{ (g)} \rightarrow 4Lu_2SiO_5 \text{ (s)} + 2N_2 \text{ (g)} \hspace{1cm} (6.3)$$

$$Lu_2SiO_5 \text{ (s)} + SiO_2 \text{ (g)} \rightarrow Lu_2Si_2O_7 \text{ (s)} \hspace{2.3cm} (6.4)$$

Reaction (6.3) and (6.4) occur due to the incompatibility of the $Lu_4Si_2N_2O_7$ and Lu_2SiO_5 phases with SiO_2 whereas the $Lu_2Si_2O_7$ is compatible with it. However, this explanation is preliminary because of the lack of thermodynamic studies and the non-availability of the phase diagram in the system Lu_2O_3-SiO_2. The Yb_2O_3-SiO_2 phase diagram [167] (*Figure 6.5*) can be considered as a guide line for the above discussion (sinceYb, being very close to Lu in the lanthanide series, is expected to show similar behaviour). The formation of the $Lu_2Si_2O_7$ phase by oxidation leads to depletion of Lu^{3+} ions below the surface, resulting in a compositional gradient of Lu^{3+} ions between the surface and bulk [168]. This leads to migration of Lu^{3+} ions from the bulk to the interface of the base material and the oxide film. Therefore the compositional gradient of Lu^{3+} ions as well as the incompatibility of lutetium-silicon oxynitride ($Lu_4Si_2N_2O_7$) with SiO_2 determine the oxidation of the SiC ceramics.
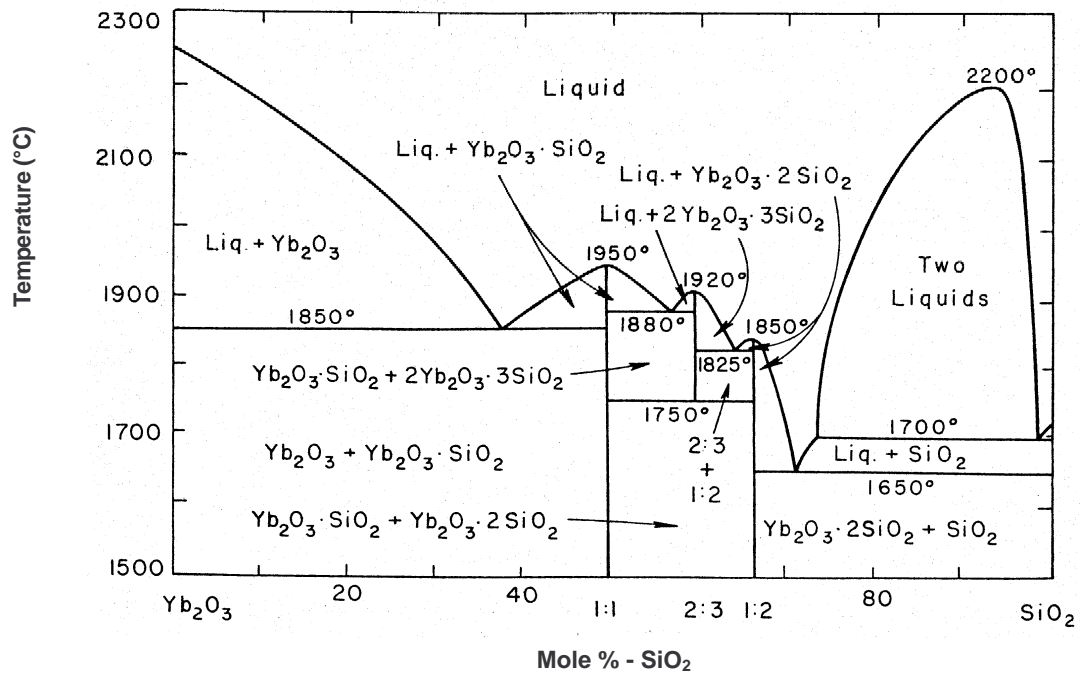
Figure 6.5: Yb$_2$O$_3$-SiO$_2$ phase diagram. Oxide ratios of compounds given as Yb$_2$O$_3$:SiO$_2$ [167].

7 Conclusions

In binary rare-earth sesquioxide systems, the characteristic sintering temperature generally decreases with increasing tolerance factor or increasing cationic radius difference. However, a linear correlation with sintering temperature can not be established due to change in the coordination number within the systems.

Sintering additives consisting of a single rare earth component are found to be unsuitable for the production of dense SiC due to insufficient liquid phase formation together with the in-situ SiO_2. β-SiC, seeded with α-SiC, was successfully sintered to full density with Gd_2O_3-Ho_2O_3 and Dy_2O_3-Ho_2O_3 additives. Dense SiC ceramics were also obtained with Lu_2O_3 substituted for Y_2O_3 in the "conventional" Y_2O_3-AlN additive system, and Lu_2O_3-AlN proved to be a promising additive system for significantly improved high temperature properties of LPS-SiC. More than 99% densification were achieved in all of these systems when sintering was carried out in N_2 atmosphere. N_2 is more effective for full densification as compared to argon atmosphere.

Sintering proceeds through the classical solution-reprecipitation mechanism as established by SEM, TEM, EDS and AES analysis. Poor wetting behaviour during sintering and devitrification result in a retraction of rare earth cations from the grain boundary to triple point regions. The extent of retraction also depends on the cationic radius of the rare earth elements.

The materials obtained after sintering have a fine-grained homogeneous microstructure of more or less equiaxed SiC grains which can be suitably designed through post sintering heat-treatment. Characteristically, the $\beta \rightarrow \alpha$-SiC phase transformation leads to anisotropic grain growth of α-SiC grains which then form an interlocked platelet type of microstructure. The kinetics of the phase transformation depends primarily on the viscosity of the secondary phase which is predominantly influenced by cationic radius and the amount of rare-earth oxides in the system.

Room temperature fracture toughness, hardness and flexural strength are directly correlated with the microstructure, the extent of secondary phase devitrification and concentration of extrinsic defects like pores, surface cracks, etc. Improvements in fracture

toughness after annealing treatments are due to crack deflection, crack bridging and mechanical interlocking mechanisms. Higher bending strength (~ 600 MPa) is observed if bimodal microstructures are formed. Fine-grained equiaxed microstructures cause improved flexural strength owing to the σ vs. $\overline{G}^{-\frac{1}{2}}$ relationship. However, the increase in average grain size ($\overline{G}$) during post sintering treatments causes lower strength indicating a trade-off between strength and fracture toughness.

The high temperature strength of the Lu_2O_3-AlN additive system primarily depends on the viscosity and the extent of devitrification after sintering and annealing treatment. The characteristic strength increase at 1200°C with Lu_2O_3 rich additives can be correlated with the surface crack/flaw healing due to the oxidation. Crystallisation of intergranular phases and decrease in their amount after the annealing treatment improve the flexural strength at high temperatures.

Like high temperature strength, the creep deformation rate also depends on the visco-elastic behaviour of the secondary phase. Devitrification and microstructural modification after post sintering heat treatments marginally influence the creep rates. Stress exponent, activation energy and the microstructural modifications observed after creep tests suggest that the creep deformation is primarily controlled by grain boundary sliding accomodated by diffusion coupled with some cavity formation.

Elastic-plastic phenomena at high temperature are governed by the characteristic viscosity of the intergranular phases. Improvements in high temperature stiffness and plastic-anelastic behaviour occurred with increasing the amount of Lu_2O_3 in the additive system and the extent of crystallisation of the secondary phase.

The details observation in the parabolic oxidation behaviour showed that the kinetics of the oxidation process is complex and it is controlled not only by the diffusion of oxygen through the SiO_2 layer, but also by surface reactions.

Zusammenfassung (German abstract)

Siliciumcarbid (SiC) erhält aufgrund seiner Kombinationen von hoher Härte, guter thermischer Leitfähigkeit, hoher Beständigkeit gegen oxidierende und korrodierende Medien und seines guten Thermoschockverhaltens einen besonderen Stellenwert in der Reihe der Hochleistungskeramiken. Bei der konventionellen Herstellung von SiC-Keramiken wird dem Ausgangspulver prinzipiell ein Sinteradditiv beigemengt. Der Einsatz von flüssigphasenbildenden Additiven erhöht die Sinterfähigkeit und ermöglicht gezielten Kornwachstum, wodurch eine vollständige Verdichtung von SiC-Werkstoffen erreicht werden kann.

Die Menge an Glasphase muss einerseits für die Verdichtung und den Zusammenhalt der SiC-Keramik ausreichend sein, andererseits ist jedoch zu beachten, dass die Hochtemperatur-eigenschaften und die Oxidationsbeständigkeit von SiC durch die Erweichung der Glasphase erheblich beeinträchtigt werden. Um die Hochtemperaturleistung der Korngrenzenphase zu verbessern, wurden verschiedene wirksame Sinterhilfsmittel untersucht. Aus der Literatur [3-8] ist bekannt, dass Seltenerdmetalloxide hochschmelzende viskose Flüssigphasen bilden, die Herstellung hochtemperatur-beständiger SiC-Werkstoff ermöglichten. Die Seltenerdmetalloxide mit kleinem Ionenradius führen dabei zu überlegenen Korrosions- und Hochtemperatur-Korrosionseigenschaften der gesinterten Keramiken [169]. Ein weiteres Auswahlkriterium ist die zu fordernde Stabilität der Oxidationsstufe 3^+ unter reduzierenden Bedingungen, so dass insbesondere die Elemente Gd, Dy, Ho, Er und Lu als Sinteradditive in Frage kommen.

Ziel der Arbeit ist es, Grundlagen für die Entwicklung von hochtemperaturstabilen additivhaltigen SiC-Werkstoffen zu schaffen, die neben sehr guten Hochtemperatureigenschaften auch über hohe Kennwerte bei Raumtemperatur verfügen. Der Zusammenhang zwischen Gefüge und verschiedenen mechanischen und thermomechanischen Eigenschaften von LPS-SiC wird diskutiert.

Siliciumcarbidkeramik wurde durch druckloses Sintern von Mischungen aus β-Siliciumcarbid- und α-Siliciumcarbidpulver als Ausgangsmaterialien, mit unterschiedlichen Kombinationen von Sesquioxiden der seltenen Erden sowie Aluminiumnitrid als Sinterzusätze, hergestellt. Zur Untersuchung des

Verdichtungsverhaltens wurden, die Grünlinge in einem Graphit-Widerstandsofen (Astro Industries bzw. FCT GmbH) unter Ar oder N_2 als Ofenatmosphäre und innerhalb des Temperaturintervalles zwischen 1850°C und 2150°C gesintert. Die Sinterdichte wurde mittels der Auftriebsmethode nach Archimedes bestimmt. Zur Bestimmung der β-SiC $\rightarrow$ α-SiC-Umwandlungskinetik wurden vollständig verdichtete Keramiken bei 1950°C für verschiedenen Zeitdauern in N_2-Atmosphäre ausgelagert (im gleichen Ofen). Die Ermittlung des β-SiC bzw. α-SiC-Phasenanteils erfolgte mit Hilfe von Röntgenbeugungs- Untersuchungen.

Die Ausbildung des Gefüges wurde mit Hilfe der Rasterelektronenmikroskopie (REM, DSM 982 Gemini, Zeiss, und S200, Cambridge Instruments) und energiegefilterten Transmissionselektronenmikroskopie (EFTEM, Zeiss EM912 Omega) analysiert. Zur qualitativen Bestimmung der chemischen Zusammensetzung der Sekundärphasen und für Untersuchungen der Mikrostruktur wurden Methoden der analytischen Elektronenmikroskopie (AEM) verwendet.

Die Raumtemperatur-Bruchzähigkeit wurde mit einer Last von 5 kg und einer Belastungszeit von 15 s mit der Eindruckmethode nach Vickers bestimmt. Messungen der RT-Biegebruchfestigkeit erfolgten an Proben (Abmessungen ~ $50 \times 3 \times 4$ mm^3) im 4-Punkt-Biegeversuch mit Auflagerabständen von 40 mm außen und 20 mm innen, bei einer Prüfgeschwindigkeit von 5 mm/s. Die 4-Punkt-Hochtemperaturbiegebruchfestig-keit wurde an Luft von 1200°C bis 1500°C bei einer Querhauptgeschwindigkeit von 0.1 mm/s gemessen. Kriechversuche an flüssigphasengesintertem SiC mittels des 4- Punkt-Biegeversuches wurden von 1200°C bis 1500°C ebenfalls an Luft durchgeführt. Die aufgebrachten Lasten lagen dabei zwischen 50 und 300 MPa. Steifigkeitstests mit einer Last von 100 MPa und einer Belastungsgeschwindigkeit von 0.1 mm/s wurden im Temperaturbereich von 850°C bis 1450°C in Intervallen von 150 K durchgeführt.

Messungen des Oxidationswiderstandes wurden bei verschiedenen Temperaturen von 1200°C bis 1500°C an Luft durchgeführt.

Das Additivsystem $RE_2^I O_3$-$RE_2^{II} O_3$

Herstellung und Verdichtung

In *Abb. 1* sind charakteristische Dilatometerläufe für alle hergestellten Materialien gezeigt. Dabei wurde eine nicht-lineare Korrelation zwischen dem Toleranzfaktor [103],

einem normierten Radiusverhältnis der Kationen und Anionen, und der Sintertemperatur festgestellt. Umfangreiche Sinterstudien wurden durchgeführt, und das Verdichtungsverhalten als Funktion des Temperaturzyklus sowie der Gasatmosphäre wurde überwacht, um die Sinterbedingungen zu optimieren.
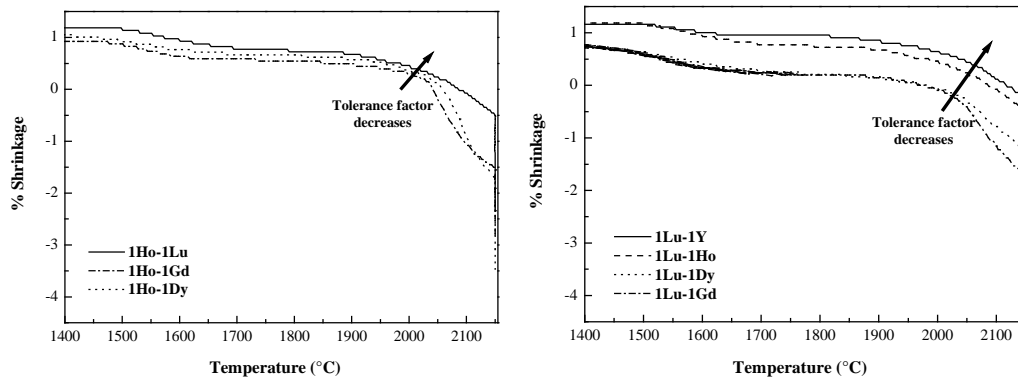

Abb. 1: Charakteristische Dilatometerkurven für SiC mit verschiedenen Seltenerdoxid-Sinteradditiven.

Tabelle 1. zeigt die Zusammensetzung der untersuchten Materialien und Ergebnisse aus Dilatometer- und Sinterstudien mit den verschiedenen Additivsysteme. LPS-SiC-Keramiken mit 1Gd-1Ho und 1Dy-1Ho erreichen vollständige Verdichtung bei 2000°C in N_2. Ein vorteilhafter Effekt von Stickstoff gegenüber Argon als Sinteratmosphäre wurde festgestellt.

Tabelle 1. Pulverspezifikationen und Resultate der Dilatometer- und Sinterversuche.

Prozess	Zusammensetzung*	Additiv (vol%)	SiC $\alpha : \beta$	% Masseverlust	% Theor. Dichte	Temperatur (°C)	Atmosphäre (0.2 MPa)
D I L A T O M E T R I E	1Gd-1Er			10	81	1900	Ar
	1Gd-1Er			6.4	96	2150	N_2
	1Sc			18	52	1950	Ar
	1Sc			8.9	53	2150	N_2
	1Lu			5.1	65	2150	,,
	1Gd-1Ho	10	10 : 90	6.3	102	2150	,,
	1Gd-1Lu			7.6	99	2150	,,
	1Dy-1Lu			8.4	82	2150	,,
	1Dy-1Ho			5.0	83	2150	,,
	1Ho-1Lu			4.8	91	2150	,,
	1Lu-1Y			6.3	99	2150	,,
Sintern	1Gd-1Ho			3.3	101	2000	,,
	1Dy-1Ho			3.3	99	2000	,,

* $1RE^{I}$ - $1RE^{II}$ bedeutet 50 mol% $RE^{I}_2 O_3$: 50 mol% $RE^{II}_2 O_3$

RT-Bruchzähigkeit und Härte

Als Folge einer Wärmebehandlung nach dem Sintern wurde eine Verbesserung der bruchmechanischen Eigenschaften beobachtet (*Abb. 2(a)*). Die Ergebnisse zeigen, dass die RT-Bruchzähigkeit von LPS-SiC stark vom Aufbau des Gefüges abhängt (*Abb. 2(b) und (c)*). Da die Ausbildung der Plattenkornmorphologie eine direkte Folge der Phasenumwandlung von β- in α-SiC ist, steigt die Festigkeit mit der Auslagerungsdauer und damit zunehmendem α-SiC-Anteil im Gefüge an. Die Messungen bestätigen die Ergebnisse von Pezzotti [134], der zeigte, dass Gefüge mit länglichen α-SiC-Körnern eine bessere Risszähigkeit (K_{Ic}) aufweisen als äquiaxiale Mikrostrukturen. Die α-SiC Plättchen führen zu einer Verzahnung des Gefüges, was bei dem vorliegenden interkristallinen Bruchverhalten eine höhere Bruchzähigkeit bewirkt.
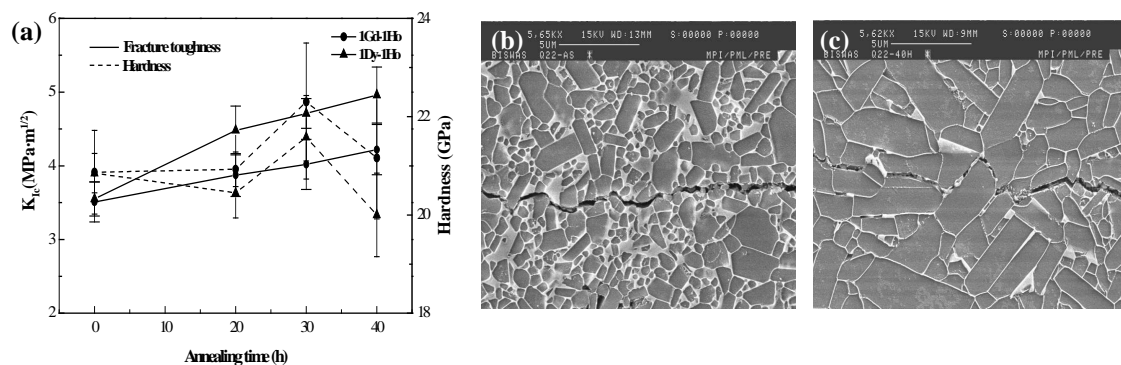

Abb. 2: (a) Variation der Bruchzähigkeit und Härte als Funktion der Auslagerungsdauer, Mikrostrukturen mit 1Dy-1Ho-Additiv, (b) im wie-gesinterten Zustand und (c) nach Wärmebehandlung bei 1950°C für 40 h.

Das Additivsystem Lu$_2$O$_3$-AlN

Flüssigphasensintern und Auslagern

Alle SiC-Proben mit Lu$_2$O$_3$-AlN-Additiven wurden zu hohen Dichten von mehr als 99% gesintert (*Tabelle 2*). In *Abb. 3* ist ein typisches Gefüge einer SiC Keramik aus dem Material 1Lu-1AlN nach dem Sintern und nach der Auslagerung dargestellt. Eine Kern-Rand-Struktur der SiC Körner (*Abb. 3(a)*) kann im REM beobachtet werden. Analysen mit Auger-Elektronen-Spektroskopie (AES) zeigen, dass im Randbereich der SiC-Körner Lu, Al, O und N nachgewiesen werden können. Danach kann gefolgert werden, dass ein Lösungs-Wiederausscheidungs-Sintermechanismus auftritt [136].

Tabelle 2. Pulverspezifikationen und Dichten/Masseverluste nach dem Sintern/der Wärmebehandlung.

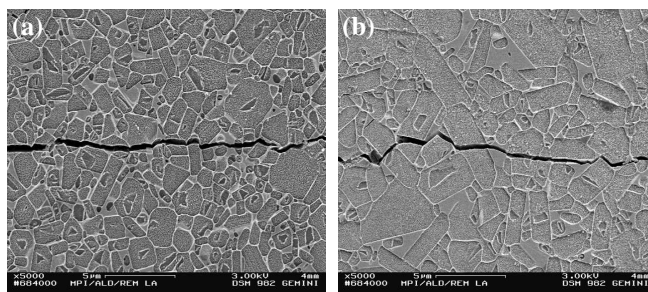| Prozess	Bezeichnung	Additive (vol%)	SiC $\alpha : \beta$	% Masseverlust	% Theor. Dichte	Temperatur (°C)	Atmosphäre (10 MPa)
Sintern	1Lu-2AlN-AS			2.3	98.9	2100	N_2
	1Lu-1AlN-AS			2.8	99.5	2100	N_2
	2Lu-1AlN-AS	10	10 : 90	2.6	99.1	2100	N_2
Wärmebehandlung	1Lu-2AlN-AN			0.8	98.9	1950	N_2
	1Lu-1AlN-AN			0.6	99.3	1950	N_2
	2Lu-1AlN-AN			2.8	98.1	1950	N_2

Abb. 3: REM-Bilder von (a) gesinterten und (b) wärmebehandeln 1Lu-1AlN-Gefügen : Rissverläufe und Kern-Rand-Struktur der SiC-Körner.
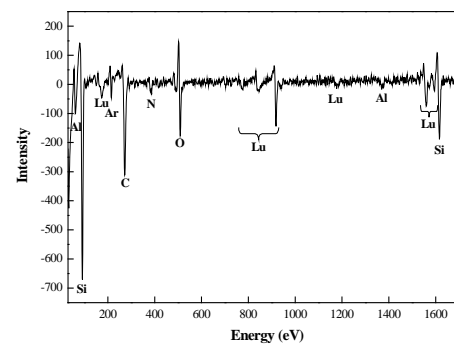
Abb. 4: Auger-spektroskopische Mikro-analyse eines SiC-Korns nach dem Sintern mit 1Lu-1AlN-Additiv.

RT-Bruchzähigkeit und Härte

Die RT-Bruchzähigkeit und Härte wurde an verschieden zusammengesetzten Materialien ermittelt und sind in *Abb. 5* graphisch dargestellt. Eine Verbesserung der Bruchzähigkeit durch weiteres Tempern nach dem Sintern wurde beobachtet. Wie in *Abb. 3(a)* und *3(b)* erkennbar, zeigen Feinkörnige Sinter-gefüge fast geradlinige Rissverläufe, während in Plättchengefügen Riss-ablenkung auftritt. Die Rissausbreitung
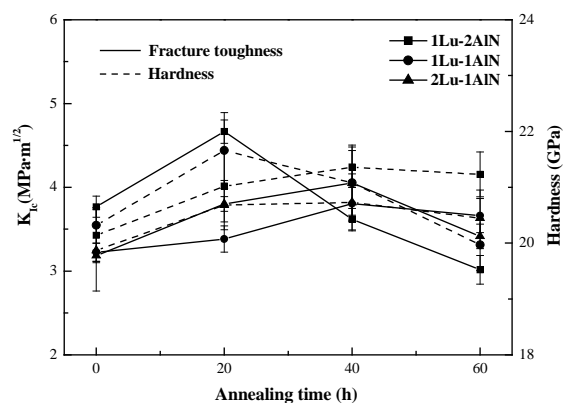

Abb. 5: Bruchzähigkeit und Härte als Funktion der Auslagerungsdauer.

ist teilweise transgranular, wenn größere Körner senkrecht zum Rissverlauf stehen. Rissablenkung, Rissüberbrückung und mechanische Verzahnung sind zähigkeitssteigernde Mechanismen [134]. Der Abfall der Bruchzähigkeit bei Langzeitausgelagerten Proben wird auf Kornvergröberung mit einem Rückgang der Kornstreckungsfaktoren zurückgeführt [136]. Zu lange Auslagerungsdauer bewirkt Poren- und Mikrorissbildung und damit eine ausgeprägte Verschlechterung der Härte.

Biegefestigkeit

In *Abb. 6* ist die Abhängigkeit der Biegefestigkeit von der Temperatur zwischen RT und 1500°C für alle Proben dargestellt. Die Biegebruchfestigkeit bei Raumtemperatur hängt maßgeblich von der Korngröße und Sekundärphasenkristallisation der Materialien ab.

Eine relativ hohe RT-Biegefestigkeit wird für 1Lu-2AlN festgestellt. Dies lässt sich auf die Ausbildung einer bimodalen Mikrostruktur zurückführen (*Abb. 7*) [143]. Wie erwartet, liegen die RT-Biegefestigkeiten der ausgelagerten Materialien deutlich unter denen der gesinterten Proben, während die HT-Festigkeit einen gegenläufigen Trend zeigt. Nach der Orowan-Petch-Relation

Abb. 6: Biegefestigkeit als Funktion der Temperatur.

nimmt durch die Kornvergröberung des Gefüges während der Auslagerung die RT-Festigkeit wesentlich ab [110]. Die gute HT-Biegefestigkeit nach der Auslagerung der SiC-Werkstoffe bis 1400°C bzw. 1500°C basiert auf einem hohen Kristallisationsgrad und einer Verringerung der Menge der Sekundärphase durch Abdampfen [130].

Die HT-Biegefestigkeit für 1Lu-2AlN fällt gegenüber der RT-Festigkeit drastisch ab, während Keramiken mit hohem Lu_2O_3–Anteil bis etwa 1200°C eine ansteigende Festigkeit zeigen. Als Ursache für diesen Trend kommt ein Rissausheilungseffekt in Frage, durch den in der Nähe der Risse Druckspannungen entstehen. Möglicherweise ergeben sich diese Druckspannungen durch die
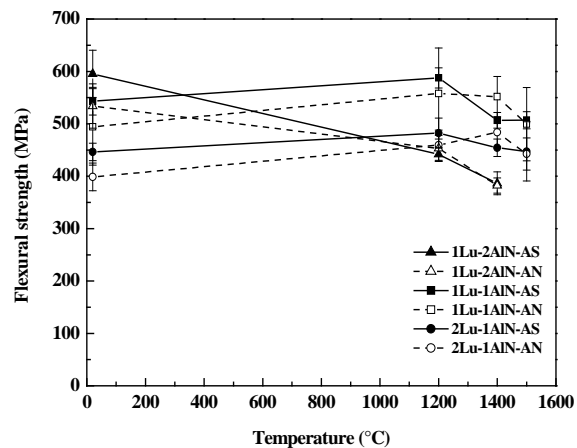
Phasenumwandlung von
Oxynitrid zu Oxid in einer
Oberflächenschicht [125].
Oberhalb einer Grenz-
temperatur zwischen 1200
und 1400°C fällt die
Festigkeit aufgrund der
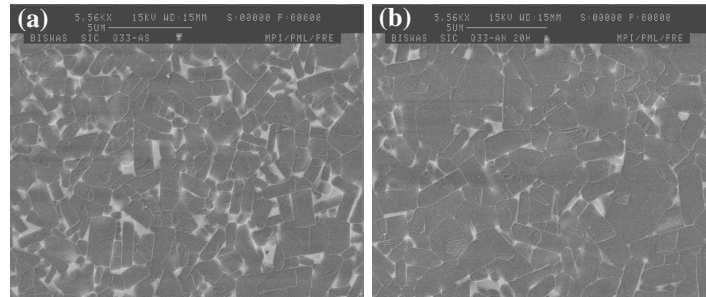Erweichung der Sekundär-
phase ab.

Abb. 7: Gefüge von 1Lu-2AlN zeigen (a) bimodale Korngrößenverteilung nach dem Sintern und (b) Kornvergröberung nach einer zusätzlichen Wärmebehandlung bei 1950°C für 20 h.

Kriechverformung

Unter den Bedingungen des Hochtemperatur-Kriechens lässt sich die Abhängigkeit der stationären Kriechrate $\dot{\varepsilon}$ von der angelegten Spannung σ und der Temperatur T meist in der Form [114] :

$$\dot{\varepsilon} = A \cdot \sigma^n \cdot e^{-Q/RT} \qquad (1)$$

darstellen, wobei n der Spannungsexponent, R die Gas-Konstante, Q die Aktivierungsenergie und A eine Konstante ist.

In *Abb. 8* ist für verschiedene Materialien, die sich im Lu_2O_3-Anteil des Additivs

unterschieden, die Kriechge-
schwindigkeit in Abhängigkeit von
der Kriechzeit bei Temperaturen
von 1300 bzw. 1400°C und einer
Biegespannung von 100 MPa
doppellogarithmisch aufgetragen.
Die Kriechraten $\dot{\varepsilon}$ der SiC–
Werkstoffe liegen bei ca. 1×10^{-9}
s^{-1} bzw. bei 1×10^{-8} s^{-1}. Die
Kriechbeständigkeit der unter-
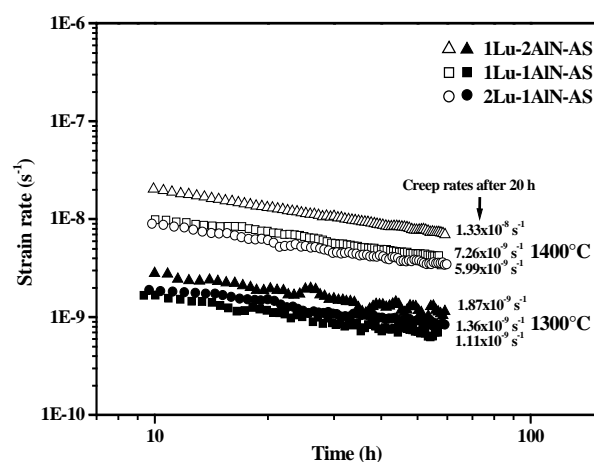suchten Materialien ist damit im

Abb. 8: Kriechraten von verschiedener Materialien bei 100 MPa Biegespannung.

Vergleich zu anderen flüssigphasengesinterten Keramiken außerordentlich hoch und wird nur noch durch einen kürzlich entwickelten Siliciumnitridwerkstoff mit Lu_2O_3 als einiges Sinteradditiv übertroffen [170]. Aus *Abb. 8* lässt sich abschätzen, dass die höchsten Kriechgeschwindigkeiten bei höheren AlN-gehalten im Additiv erreicht werden, da hier auch die Viskosität der Glasphase am niedrigsten ist.

Die Spannungsexponenten und die Aktivierungsenergien für 1Lu-1AlN Materialien lassen sich nach Gleichung (1) aus *Abb. 9* und *Abb. 10* ermitteln. Da stationäres Kriechen, bei den vorliegenden Materialien nicht erreicht wird, wurden ersatzweise die Kriechen nach 20 h als Funktion der Spannung bzw. der reziproken Temperatur aufgetragen sind. Zwischen 1200°C und 1500°C ergaben sich Spannungsexponenten von etwa 1 bis 1.7. Für die Aktivierungsenergien dieser Materialien werden Werte von etwa 250 bis 450 kJ/mol erhalten.
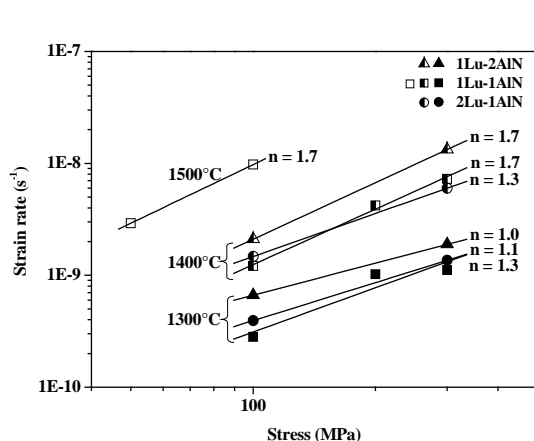
Abb. 9: Spannungsexponenten n wie-gesinterter Materialien bei verschiedenen Temperaturen.
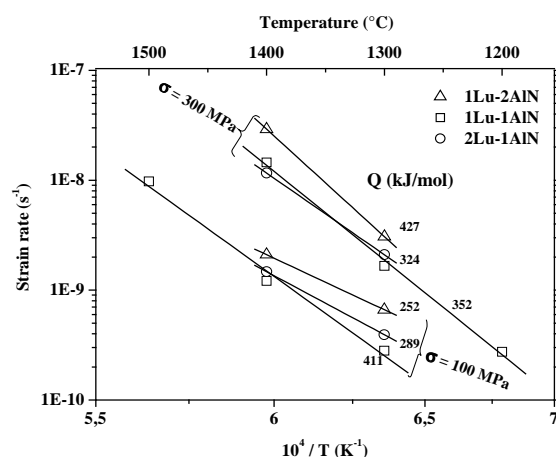

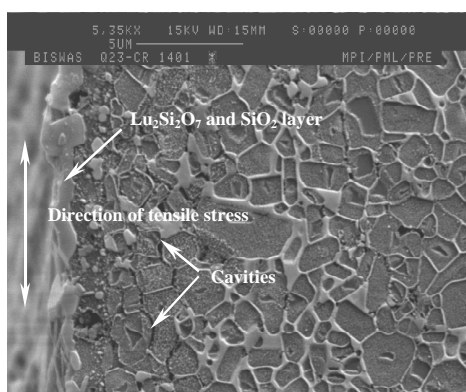*Abb. 10: Aktivierungsenergien Q wie-gesinterter Proben bei unterschiedlichen Biegespannungen.*

Abb. 11: REM-Bild einer 1Lu-1AlN-Probe nach dem Kriechversuch (1400°C, 60 h, 100 MPa).

In *Abb. 11* ist eine REM-Aufnahme der Zugseite einer SiC-Kriechprobe der Zusammensetzung 1Lu-1AlN gezeigt. Am Rand sind Poren an den Korngrenzen in der Keramikmatrix zu erkennen.

In der Analyse des Biegekriechens von Hollenberg *et al.* [115] wird vorausgesetzt, dass für kleine Dehnungen (< 2%) das Kriechverhalten aufgrund der stabilen Mittellage der neutralen Faser bezüglich Zug- und Druckbelastung symmetrisch ist. Deshalb ist die durch Gleichung (1) gegebene Kriechgeschwindigkeit im vorliegenden Falle gültig. Im Prinzip spiegeln sich die dominierenden mikroskopischen Prozesse in den Kriechparametern n und Q wieder. Für LPS-SiC werden in 4-Punkt-Biegung Spannungsexponenten von n = 1 – 2 berichtet, wobei Korngrenzengleiten (bzw. viskoses Fließen des Korngrenzenfilms) oder grenzschichtkontrollierte Diffusion als Kriechmechanismen in Betracht gezogen werden [118,119,151,154-157]. Die ermittelten Spannungsexponenten von n = 1.0 – 1.7 liegen somit in guter Übereinstimmung mit der Literatur. Die gemessene durchschnittliche Aktivierungsenergie (250-450 kJ/mol) deutet auf viskoses Fließen von amorphen Silikatphasen hin [120,160].

Hochtemperatursteifigkeit

Zum besseren Verständnis des elastisch-plastischen Verhaltens bei hoher Temperatur wurde ein dynamischer Belastungstest durchgeführt (100 MPa, 60 s Belastungszeit). Der Verformungsgrad ist dabei ein Maß für die Steifigkeit, und die Hysterese zwischen Be- und Entlastungskurve ist ein Maß für die dissipierte Energie. Eine große Hysteresefläche und ein deutlicher Abfall der Steifigkeit zu hohen Temperaturen hin werden im Falle von 1Lu-2AlN beobachtet (*Abb. 12*). Dies liegt an der Erweichung der Sekundärphase bei hoher Temperatur. Die Steifigkeit

Abb. 11: Ergebnisse der HT-Steifigkeitstests mit verschiedenen Materialzusammensetzungen.

zeigt bei der mittleren Zusammensetzung 1Lu-1AlN den besten Verlauf, wo offensichtlich ein optimaler Kompromiss zwischen Viskosität und Kristallisationsgrad erreicht wird.
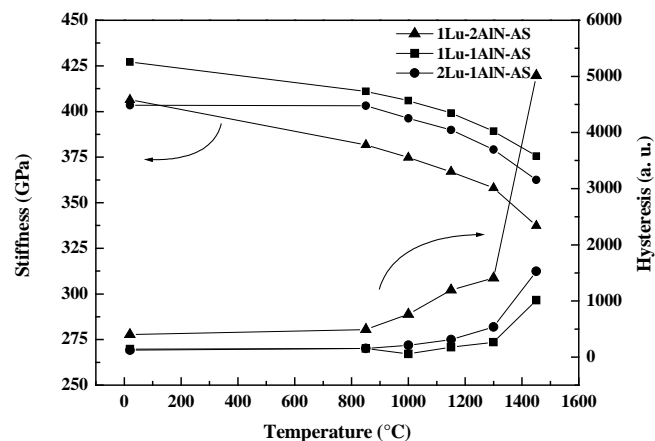
Oxidation

Die Oxidation von Siliciumcarbid ist durch ein parabolisches Geschwindigkeitsgesetz gekennzeichnet (*Abb. 13(a) und (b)*). Danach verläuft die Gewichtszunahme in allen Fällen nach einem diffusionsgesteuerten Mechanismus. Das gute Oxidationsverhalten der Lu_2O_3-reichen SiC-Werkstoffe 1Lu-1AlN und 2Lu-1AlN bis 1400°C bzw. 1500°C basiert auf einer hohen Viskosität der Lu_2O_3-reichen amorphen Restphase, die zu einer niedrigen Rate der Auswärtsdiffusion von Additivionen zur Oxidationsoberfläche führt. Die Oxidationsrate Lu_2O_3-armer Materialien bei der niedrigsten untersuchten Temperatur von 1200°C ist besonders niedrig, weil der Kristallisationsgrad in diesem Material sehr hoch ist (*Abb. 13(b)*). Die Oxidationskinetik wird also wahrscheinlich bei niedriger Temperatur, wo die silikatische Oxidschicht dünn ist, durch die Anionendiffusion durch die Oxidschicht hindurch kontrolliert, bei hoher Temperatur dagegen durch Kationendiffusion durch die glasartige Sekundärphase zur oberflächlichen Oxidschicht hin. Die Absolutwerte der Oxidationsrate sind in allen Fällen in Vergleich zu andern flüssigphasengesinterten, Si-basierten Werkstoffen sehr niedrig [171,172].
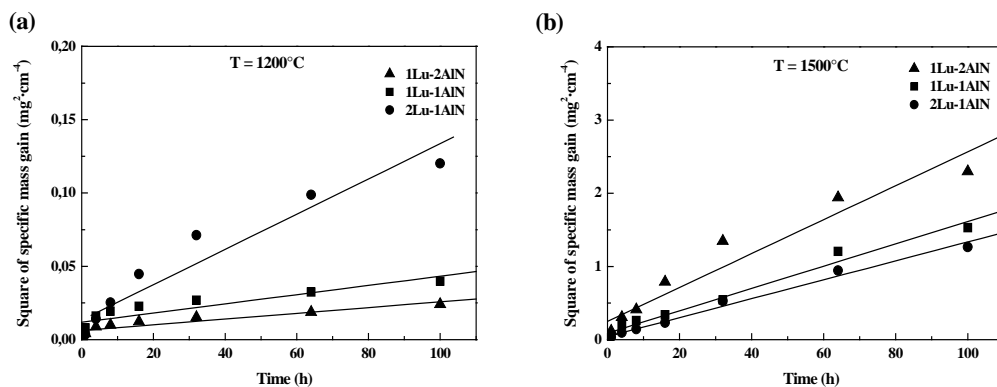

Abb. 13: Parabolische Oxidationsrate verschieden zusammengesetzter Materialien bei (a) 1200°C und (b) 1500°C.

References

[l] K. Yamada and M. Mohri, 'Silicon Carbide Ceramics', **Vol.1,** ed. S. Sōmiya and Y. Inomata, Elsevier, Barking, U.K. (1991) p.13.

[2] P. Popper, 'Special Ceramics', ed. P. Popper, The Brit. Ceram. Res. Assoc., Stoke-on-Trent, U.K. (1960) p.209.

[3] N. Camuşcu, D. P. Thompson and H. Mandal, J. Eur. Ceram. Soc., **17** (1997) 599.

[4] M. K. Cinibulk and G. Thomas, J. Am. Ceram. Soc., **75** (1992) 2037.

[5] Z. Shen, P. Käll and M. Nygren, J. Mater. Res., **14** (1999) 1462.

[6] A. Rosenflanz and I. W. Chen, J. Eur. Ceram. Soc., **19** (1999) 2325.

[7] K. Hirao, K. Watari, M. Toriyama and S. Kanzaki, J. Am. Ceram. Soc., **84** (2001) 353.

[8] Y. Menke, V. Peltier-Baron and S. Hampshire, J. Non-Cryst. Solids, **276** (2000) 145.

[9] L. S. Ramsdell, Am. Mineral., **32** (1947) 64.

[10] T. Tagai, S. Sueno and R. Sadanaga, Mineral J., **6** (1971) 240.

[11] E. G. Acheson, Chem. News, **68** (1893) 179.

[12] P. Matje and K. A. Schwetz, 'Ceram. Trans., Ceramic Powder Science II', A, **Vol.1,** ed. G. L. Messing, E. R. Fuller, Jr. and H. Hausner, The Am. Ceram. Soc., Westerville, Ohio (1988) p.460.

[13] Y. Okaba, J. Hojo and A. Kato, J. Chem. Soc. Japan, **88** (1980) 188.

[14] Y. Okaba, J. Hojo and A. Kato, J. Less-Common Met., **68** (1979) 29.

[15] G. C. Wei, C. R. Kennedy and L. A. Harris, Am. Ceram. Soc. Bull., **63** (1984) 1054.

[16] T. Hase and H. Suzuki, J. Ceram. Soc. Japan, **86** (1978) 606.

[17] Y. Ando et al., J. Cryst. Growth, **52** (1981) 178.

[18] W. R. Cannon, S. C. Danforth, J. H. Flint, J. S. Haggerty and R. A. Marra, J. Am. Ceram. Soc., **65** (1982) 324.

[19] W. R. Cannon, S. C. Danforth, J. S. Haggerty and R. A. Marra, J. Am. Ceram. Soc., **65** (1982) 330.

[20] M. Luce, O. Croix, C. Robert and M. Cauchetier, 'Ceram. Trans., Ceramic Powder Science III', **Vol.12,** ed. G. L. Messing, S. Hirano and H. Hausner, The Am. Ceram. Soc., Westerville, Ohio (1990) p.267.

[21] C. Greskovich and J. H. Rosolowski, J. Am. Ceram. Soc., **59** (1976) 336.

[22] S. Prochazka, 'Mass Transport Phenomena in Ceramics', ed. A. R. Cooper and A. H. Heuer, **Vol.9,** Plenum Press, New York (1975) p.421.

[23] H. Hausner, 'Energy and Ceramics', Mater. Sci. Monographs, **Vol.6**, ed. P. Vincenzini, Elsevier Scientific Publ. Co., Amsterdam (1980) p.582.

[24] H. Suzuki and T. Hase, 'Proc. Int. Symp. on Factors in Densification and Sintering of Oxide and Non-Oxide Ceramics', ed. S. Sōmiya and S. Salto, Gakujutsu Bunken, Fukyu-kai, Tokyo (1979) p.345.

[25] Y. Murata and R. H. Smoak, 'Proc. Int. Symp. on Factors in Densification and Sintering of Oxide and Non-Oxide Ceramics', ed. S. Sōmiya and S. Saito, Gakujutsu Bunken, Fukyu-kai, Tokyo (1979) p.383.

[26] D. H. Stutz, S. Prochazka and J. Lorenz, J. Am. Ceram. Soc., **68** (1985) 479.

[27] R. A. Alliegro, L. B. Coffin and J. R. Tinklepaugh, J. Am. Ceram. Soc., **39** (1956) 386.

[28] W. Bröcker, H. Landfermann and H. Hausner, Powder Metall. Int., **11** (1979) 83.

[29] S. Shinozaki, J. Haugas, W. T. Donlon, R. M. Williams and B. N. Juterbock, 'Advanced Ceramics II', ed. S. Sōmiya, Elsevier Applied Science, London (1988) p.7.

[30] A. Kerber, H. Hoffmann and P. Wirth, 'Ceram. Trans., Ceramic powder science III', **Vol.12,** ed. G. L. Messing, S. Hirano and H. Hausner, The Am. Ceram. Soc., Westerville, Ohio (1990) p.895.

[31] J. Hojo, 'Silicon Carbide Ceramics', **Vol.1,** ed. S. Sōmiya and Y. Inomata, Elsevier, Barking, U.K. (1991) p.149.

[32] H. Tanaka, 'Silicon Carbide Ceramics', **Vol.1,** ed. S. Sōmiya and Y. Inomata, Elsevier, Barking, U.K. (1991) p.213.

[33] S. Prochazka, C. A. Johnson and R. A. Giddings, 'Proc. Int. Symp. on Factors in Densification and Sintering of Oxide and Non-Oxide Ceramics', ed. S. Sōmiya and S. Saito, Gakujutsu Bunken, Fukyu-kai, Tokyo (1979) p.366.

[34] M. N. Rahaman, 'Ceramic Processing and Sintering', Marcel Dekker, New York (1995) p.707.

[35] J. S. Nadeau, Am. Ceram. Soc. Bull., **52** (1973) 170.

[36] D. Kalish and E. V. Clougherty, Am. Ceram. Soc. Bull., **48** (1969) 570.

[37] K. Takatori, N. Ogawa, M. Shimada and M. Koizumi, 'Energy and Ceramics', Mater. Sci. Monographs, **Vol.6**, ed. P. Vincenzini, Elsevier Scientific Publ. Co., Amsterdam (1980) p.525.

[38] T. Sakai and T. Aikawa, J. Am. Ceram. Soc., **71** (1988) C-7.

[39] T. Sakai and N. Hirosaki, J. Am. Ceram. Soc., **68** (1985) C-191.

[40] R. Ruh, A. Zangvil and J. Barlowe, Am. Ceram. Soc. Bull., **64** (1985) 1368.

[41] J. Schoennahl, B. Willer and M. Daire, 'Sintering-New Developments', ed. M. M. Ristic, Elsevier Scientific Publ. Co., Amsterdam (1979) p.338.

[42] M. Omori and H. Takei, J. Am. Ceram. Soc., **65** (1982) C-92.

[43] N. P. Padture and B. R. Lawn, J. Am. Ceram. Soc., **77** (1992) 2518.

[44] M. A. Mulla and V. D. Kristic, J. Mater. Sci., **29** (1994) 934.

[45] M. A. Mulla and V. D. Kristic, Acta Metall., **42** (1994) 303.

[46] N. P. Padture, J. Am. Ceram. Soc., **77** (1994) 519.

[47] Y. W. Kim, M. Mitomo and H. Hirotsuru, J. Am. Ceram. Soc., **78** (1995) 3145.

[48] M. A. Mulla and V. D. Kristic, Am. Ceram. Soc. Bull., **70** (1991) 439.

[49] M. Omori and H. Takei, J. Mater. Sci., **23** (1988) 3744.

[50] A. K. Misra, J. Am. Ceram. Soc., **74** (1991) 345.

[51] K. Suzuki, 'Silicon Carbide Ceramics', **Vol.2,** ed. S. Sōmiya and Y. Inomata, Elsevier, Barking, U.K. (1991) p.163.

[52] L. S. Sigl and H. J. Kleebe, J. Am. Ceram. Soc., **76** (1993) 773.

[53] T. Grande, H. Sommerset, E. Hagen, K. Wiik and M. A. Einarsrud, J. Am. Ceram. Soc., **80** (1997) 1047.

[54] F. F. Lange, J. Mater. Sci., **10** (1975) 314.

[55] M. Nader, Doctoral Thesis, University of Stuttgart (1995).

[56] K. Y. Chia, W. D. G. Böcker and R. S. Storm, U. S. Pat. 5,298,470 (1994).

[57] H. W. Jun, H. W. Lee, G. H. Kim, H. S. Song and B. H. Kim, Ceram. Engg. and Sci. Proc., **18** (1997) 487.

[58] A. Jeutter, Diplom Thesis, University of Stuttgart (1993).

[59] Z. K. Huang and T. Y. Tien, J. Am. Ceram. Soc., 7**9** (1996) 1717.

[60] B. W. Lin, M. Imai, T. Yano and T. Iseki, J. Am. Ceram. Soc., **69** (1986) C-67.

[61] K. Suzuki, Bull. Ceram. Soc. Japan, **21** (1986) 590.

[62] R. Hamminger, G. Grathwohl and F. Thümmler, 'Science of Ceramics', **Vo1.12,** ed. P. Vincenzini, Ceramurgica s.r.l., Faenza, Italy (1984) p.299.

[63] S. S. Shinozaki, W. T. Donlon, R. M. Williams, B. N. Juterbock and T. J. Whalen, 'Advanced Ceramics', ed. S. Sōmiya and R. C. Bradt, Terra Scientific Publ. Co., Tokyo (1987) p.35.

[64] P. Greil and D. Stutz, 'Advanced Ceramics', ed. S. Sōmiya and R. C. Bradt, Terra Scientific Publ. Co., Tokyo (1987) p.49.

[65] K. Suzuki and M. Sasaki 'Fundamental Structural Ceramics', ed. S. Sōmiya and R. C. Bradt, Terra Scientific Publ. Co., Tokyo (1987) p.75.

[66] M. Sasaki, K. Suzuki, H. Nishimura and M. Noshiro Proc. of the World Congr. an High Tech. Ceramics, 6th CIMTEC, ed. P. Vincenzini, Elsevier Scientific Publ., B. V., Amsterdam (1987) p.1101.

[67] S. K. Lee and C. H. Kim, J. Am. Ceram. Soc., **77** (1994) 1655.

[68] Y. W. Kim, M. Mitomo and H. Hirotsuru, J. Am. Ceram. Soc., **80** (1997) 99.

[69] W. Rafaniello, M. R. Plichta and A. V. Virkar, J. Am. Ceram. Soc., **66** (1983) 272.

[70] A. Zangvil and R. Ruh, J. Am. Ceram. Soc., **71** (1988) 884.

[71] S. Y. Kuo and A. V. Virkar, J. Am. Ceram. Soc., **72** (1989) 540.

[72] S. Y. Kuo, A. V. Virkar and W. Rafaniello, J. Am. Ceram. Soc., **70** (1987) C-125.

[73] S. Y. Kuo and A. V. Virkar, J. Am. Ceram. Soc., **73** (1990) 2640.

[74] W. E. Mayo and T. Tsakalakos, Metall. Trans. A, **11A** (1980) 1637.

[75] J. Chen, Q. Tian and A. V. Virkar, J. Am. Ceram. Soc., **75** (1992) 809.

[76] I. Wiedmann, Doctoral Thesis, University of Stuttgart (1998).

[77] J. W. Edington, D. J. Rowcliffe and J. L. Hawshall, Powder Met. Int., **7** (1975) 82.

[78] S. Prochazka and R. J. Charies, Am. Ceram. Soc. Bull., **52** (1973) 885.

[79] S. Dutta, J. Mater. Sci., **19** (1984) 1307.

[80] S. Dutta, J. Am. Ceram. Soc., **68** (1985) C-269.

[81] M. Keppeler, H. G. Reichert, J. M. Broadley, G. Thurn, I. Wiedmann and F. Aldinger, J. Eur. Ceram. Soc., **18** (1998) 521.

[82] J. W. Edington, D. J. Rowcliff and J. L. Hawshall, Powder Met. Int., **7** (1975) 136.

[83] K. A. Schwetz and A. Lipp, 'Science of Ceramics', **Vol.10,** ed. H. Hausner, Dt. Keram. Ges., Köln (1980) p.149.

[84] G. Grathwohl, R. Hamminger, H. Iwanek and F. Thümmler, 'Science of Ceramics', **Vol.12,** ed. P. Vincenzini, Ceramurgica s.r.1., Faenza, Italy (1984) p.583.

[85] K. T. Faber and A. G. Evans, J. Am. Ceram. Soc., **66** (1983) C-94.

[86] H. Kodama and T. Miyoshi, J. Am. Ceram. Soc., **75** (1992) 1558.

[87] J. J. Cao, W. J. MoberlyChan, L. C. DeJonghe, C. J. Gilbert and R. O. Ritchie, J. Am. Ceram. Soc., **79** (1996) 461.

[88] P. L. Farnsworth and R. L. Coble, J. Am. Ceram. Soc., **49** (1966) 264.

[89] T. L. Francis and R. L. Coble, J. Am. Ceram. Soc., **51** (1968) 115.

[90] R. K. Govila, J. Mater. Sci., **18** (1983) 1967.

[91] T. H. Elmer and M. E. Nordberg, J. Am. Ceram. Soc., **50** (1967) 275.

[92] G. M. Renlund, S. Prochazka, R. H. Doremus, J. Mater. Res., **6** (1991) 2723.

[93] R. D. Shannon and C. T. Prewitt, Acta. Cryst., **B25** (1969) 925.

[94] W. D. Kingery, J. Appl. Phys., **30** (1959) 301.

[95] W. D. Kingery, J. Appl. Phys., **30** (1959) 307.

[96] G. Petzow and W. J. Huppmann, Z. Metallkde., **67,** (1976) 579.

[97] R. M. German, 'Liquid Phase Sintering', Plenum Press, NY (1985).

[98] J. L. Iskoe, F. F. Lange and E. S. Diaz, J. Mater. Sci., **11** (1976) 908.

[99] S. C. Singhal, J. Mater. Sci., **11** (1976) 500.

[100] W. H. Zachariasen, J. Am. Ceram. Soc., **54** (1932) 3841.

[101] A. Makishima, Y. Tamura and T. Sakaino, J. Am. Ceram. Soc., **61** (1978) 247.

[102] A. Makishima, M. Kobayashi and T. Shimohira, J. Am. Ceram. Soc., **65** (1982) C-210.

[103] B. O. Mysen, Geochim. Cosmocim. Acta., **59** (1995) 455.

[104] J. E. Shelby, 'Introduction to Glass Science and Technology', The Royal Soc. Chem., Cambridge, England (1997).

[105] E. Shelby and J. T. Kohli, J. Am. Ceram. Soc., **73** (1990) 39.

[106] A. Dietzel, Z. Elektrochem., **48** (1942) 9.

[107] Scandium: Occurrence, Chemistry, Physics, Metallurgy, Biology and Technology, ed. C. T. Horovitz, Acad. Pr. (1975) p190.

[108] M. Barsoum, 'Fundamentals of Ceramics', McGraw-Hill, Singapore (1997).

[109] A. A. Griffith, Phil. Trans. R. Acad., **A221** (1920) 163.

[110] R. W. Rice, 'Mechanical Properties of Ceramics and Composites', Marce Dekker, , New York (2000) p.127.

[111] S. C. Carniglia, J. Am. Ceram. Soc., **55** (1972) 243.

[112] G. R. Anstis, P. Chantukul, B. R. Lawn and D. B. Marshall, J. Am. Ceram. Soc., **64** (1981) 533.

[113] P. Becher, J. Am. Ceram. Soc., **74** (1991) 255.

[114] W. R. Cannon and T. G. Langdon, J. Mater. Sci., **18** (1983) 1.

[115] G. W. Hollenberg, G. R. Terwillinger and R. S. Gordon, J. Am. Ceram. Soc., **54** (1971) 196.

[116] S. Timoshenko, 'Strength of Materials', Part II: Advanced Theory and Problems, 3rd edition, Krieger Publ. Co., Melbourne (1956).

[117] J. E. Lane, C. H. Carter, Jr., R. F. Davis, J. Am. Ceram. Soc., **71** (1988) 281.

[118] S. M. Wiederhorn, B. J. Hockey and J. D. French, J. Eur. Ceram. Soc., **19** (1999) 2273.

[119] M. T. Lin, J. L. Shi, D. Y. Jiang, M. L. Ruan and T. R. Lai, Mater. Sci. Engg., **A 300** (2001) 61.

[120] G. Pezzotti, H. -J. Kleebe, H. Nishimura and K. Ota, J. Am. Ceram. Soc., **84** (2001) 2371.

[121] S. C. Singhal, Ceram. Int., **2** (1976) 123.

[122] S. C. Singhal, 'Properties of High Temperature Alloys', ed. Z. A. Foroulis and F. C. Pettit, The Electrochem. Soc., Princeton, NJ (1976) p.697.

[123] E. M. Levin, C. R. Robbins and H. F. McMurdie, 'Phase Diagram for Ceramists', 1969 Supplement, The Am. Ceram. Soc., Columbus, OH (1969) p.76.

[124] H. -J. Choi, J. G. Lee and Y.-W. Kim, J. Mater. Sci., **32** (1997) 1937.

[125] G. Rixecker, I. Wiedmann, K. Biswas and F. Aldinger, Werkstoffwoche'98 - Band VII, Wiley - VCH, Weinheim, Germany (1999) p.215.

[126] D. Chen, M. E. Sixta, X. F. Zhang, L. C. De Jonghe and R. O. Ritche, Acta. Mater., **48** (2000) 4599.

[127] D. Munz and T. Fett, 'Ceramics: Mechanical Property, Failure Behavior, Materials Selection', Springer-Verlag (1999) p.240.

[128] Y. Murakami and H. Yamamoto, J. Ceram. Soc. Japan, **102** (1994) 231.

[129] H. H. Ye, Doctoral Thesis, University of Stuttgart (2002).

[130] D. Sciti, S. Guicciardi and A. Bellosi, J. Eur. Ceram. Soc., **21** (2001) 621.

[131] S. -L. Hwang and I. -W. Chen, J. Am. Ceram. Soc., **77** (1994) 165.

[132] K. Biswas, G. Rixecker, I. Wiedmann, M. Schweizer, G. S. Upadhyaya and F. Aldinger, Mater. Chem. Phys., **67** (2001) 180.

[133] I. M. Peterson and T. -Y. Tien, J. Am. Ceram. Soc., **78** (1995) 2345.

[134] G. Pezzotti, Acta. Metall. Mater., **41** (1993) 1825.

[135] R. W. Rice, C. Cm. Wu and F. Borchelt, J. Am. Ceram. Soc., **77** (1994) 2539.

[136] D. Sciti and A. Bellosi, J. Mater. Res., **16** (2001) 806.

[137] H. Klemm and G. Pezzotti, J. Am. Ceram. Soc., **77** (1994) 553.

[138] H. -J. Choi, J. G. Lee and Y.-W. Kim, J. Eur. Ceram. Soc., **19** (1993) 773.

[139] Y. W. Kim, M. Mitomo and T. Nishimura, J. Am. Ceram. Soc., **84** (2001) 2060.

[140] T. Kinoshita, S. Munekawa and S. –I. Tanaka, Acta. Mater., **45** (1997) 801.

[141] M. Ohashi, K. Nakamura, K. Hirao, M. Toriyama and S. Kanzaki, Ceram. Int., **23** (1997) 27.

[142] Y. Zhou, K. Hirao, M. Toriyama, Y. Yamauchi and S. Kanzaki, J. Am. Ceram. Soc., **84** (2001) 1642.

[143] P. F. Becher, E. Y. Sun, K. P. Plucknett, K. B. Alexander, C. -H. Hsueh, H. -T. Lin, S. B. Waters, C. G. Westmoreland, E. -S. Kang, K. Hirao and M. E. Brito, J. Am. Ceram. Soc., **81** (1998) 2821.

[144] P. F. Becher, S. B. Waters, C. G. Westmoreland and L. Riester, J. Am. Ceram. Soc., **85** (2002) 897.

[145] S. K. Lee, Y. C. Kim and C. H. Kim, J. Mater. Sci., **29** (1994) 5321.

[146] Y. W. Kim, M. Mitomo, H. Emoto and J. G. Lee, J. Am. Ceram. Soc., **81** (1998) 3136.

[147] D. -H. Cho, Y. -W. Kim and W. Kim, J. Mater. Sci., **32** (1997) 4777.

[148] T. D. Gulden, J. Am. Ceram. Soc., **52** (1969) 585.

[149] H. Serizawa, M. Ando, C. A. Lewinsohn and H. Murakawa, J. Nuclear Mater., **289** (2001) 16.

[150] R. W. Hertzberg, 'Deformation and Fracture Mechanics of Engineering Materials', Wiley, New York (1995) p.127.

[151] T. Nagano, K. Kaneko, G. -D. Zhan, M. Mitomo and Y. -W. Kim, J. Eur. Ceram. Soc., **22** (2002) 263.

[152] J. R. Dryden, Acta Metall. **37** (1989) 2007.

[153] L. An, R. Riedel, C. Konetschny, H. -J. Kleebe and R. Raj, J. Am. Ceram. Soc., **81** (1998) 1349.

[154] J. A. Todd, Z. Y. Zu, J. Mater. Sci., **24** (1989) 4443.

[155] T. Nagano, K. Kaneko, G. -D. Zhan and M. Mitomo, J. Am. Ceram. Soc., **83** (2000) 2497.

[156] D. S. Wilkinson, J. Am. Ceram. Soc., **81** (1998) 275.

[157] B. A. Fields and S. M. Wiederhorn, J. Am. Ceram. Soc., **79** (1996) 977.

[158] A. Gallardo-López, A. Muñoz, J. Martínez-Fernández and A. Domínguez-Rodríguez, Acta. Mater., **47** (1999) 2185.

[159] R. D. Nixon and R. F. Davis, J. Am. Ceram. Soc., **75** (1992) 1786.

[160] G. Pezzotti, H. -J. Kleebe and K. Ota, J. Am. Ceram. Soc., **81** (1998) 3293.

[161] M. Mizuno, S. Zhu, Y. Kagawa and H. Kaya, J. Eur. Ceram. Soc., **18** (1998) 1869.

[162] R. Yue, Y. Wang and C. Chen, Appl. Sur. Sci., **148** (1999) 73.

[163] I. A. Aksay and J. A. Pask, J. Am. Ceram. Soc., **58** (1975) 507.

[164] M. K. Cinibulk and G. Thomas, J. Am. Ceram. Soc., **75** (1992) 2044.

[165] E. Gomez, I. Iturriza, J. Echeberria and F. Castro, Scripta Metall. et Mater., **33** (1995) 491.

[166] H. -J. Choi, J. -G. Lee and Y. -W. Kim, J. Eur. Ceram. Soc., **19** (1999) 2757.

[167] E. M. Levin, C. R. Robbins and H. F. McMurdie, 'Phase Diagrams for Ceramists', ed. M. K. Reser, The Am. Ceram. Soc. (1969) p.108.

[168] L. K. L. Falk and E. U. Engstrom, J. Am. Ceram. Soc., **74** (1991) 2286.

[169] Gmelin Handbuch der Anorganischer Chemie, **8.** Auflage, Seltenerdelemente, Teil C1, ed. H. Bergmann, Springer-Verlag, Berlin (1974).

[170] F. Lofaj, S. M. Wiederhorn, G. G. Long, P. R. Jemian and M. K. Ferber, den Keramischen Materialien und in den Bestandteilen für Maschinen ein, Wiley - VCH, Goslar, Germany (2000) p.487.

[171] D. -M. Liu, Cream. Int., 23 (1997) 425.

[172] R. P. Jensen, W. E. Luecke, N. P. Padture and S. M. Wiederhorn, Mater. Sci. Engg., **A282** (2000) 109.

Curriculum Vitae (Lebenslauf)

Name : Koushik BISWAS

Date of birth : 24-11-1973

Place of birth : Jamshedpur, India

Nationality : Indian

Family status : Single

School educations :

1977 – 1981	**Vivekananda Sarada Mission, Jamshedpur, India**
1982 – 1983	**Chetla Boy's High School, Calcutta, India**
1984 – 1985	**Bishnupur Shikhya Sanghya, Amtola Bishnupur, W. B., India**
1986 - 1992	**Kamrabad Uchchya Vidyalaya, Sonarpur, W. B., India**

Graduate studies :

08.1982 – 06.1996	**Bachelor of Engineering (Metallurgy), Jadavpur University, Calcutta, India**
12.1996 – 05.1999	**Master of Technology (Materials and Metallurgical Engineering), Indian Institute of Technology Kanpur, India and University of Stuttgart, Germany** *Thesis: "Liquid phase assisted sintering of alumina and silicon carbide based ceramics"*
08.1999 – 12.2002	**PhD, Max-Planck Institute für Metallforschung and University of Stuttgart, Germany** *Thesis: "Liquid phase sintering of SiC ceramic with rare earth sesquioxides"*

Work experiences :

07.1996 – 12.1996	**Marketing executive, ESAB India Ltd., Jamshedpur, India**
12.1996 – 05.1999	**Research and teaching associates, Indian Institute of Technology Kanpur, India**
08.1999 – 12.2002	**Graduate research fellow, Max-Planck Institute für Metallforschung, Stuttgart, Germany**